Doctoral Dissertation
Doctoral Program in Materials Science and Technology (35th Cycle)

Effects of polymorphs and of Fe-doping on the properties of engineered nano TiO_2 for photocatalytic degradation of emerging pollutant

By

Nicola Blangetti

******

Supervisor(s):
Prof. Bonelli Barbara, Supervisor
Prof. Serena Esposito, Co-Supervisor
Dr. Francesca Stefania Freyria, Co-Supervisor

Doctoral Examination Committee:
Prof. Magnacca Giuliana , Referee, University of Turin, Italy
Prof. Tanveer Ahmed Gadhi, Referee, University of Jamshoro, Pakistan

Politecnico di Torino
2023

Declaration

I hereby declare that the contents and organization of this dissertation constitute my own original work and does not compromise in any way the rights of third parties, including those relating to the security of personal data.

Nicola Blangetti

2023

* This dissertation is presented in partial fulfillment of the requirements for **Ph.D. degree** in the Graduate School of Politecnico di Torino (ScuDo).

I would like to dedicate this thesis to my brother Dani, his girlfriend Luna, my father Frank and, last but not least,Vanessa. But what is the most important, I would like to tell to my mum, wherever she is, that everything is fine thanks to you.

Acknowledgment

I would like to thank my supervisor Prof Barbara Bonelli for the constant support and guidance throughout this project. Many thanks to Dr Francesca Stefania Freyria without whom I would not have been able to complete this research. I would also like to acknowledge Prof Marco Armandi and Prof. Serena Esposito for their participation and engagement.

Abstract

Titanium dioxide (TiO_2) is well-known semiconductor used in many technological fields. I focused my attention on TiO_2 nanoparticles synthesis and their physico-chemical characterization for their application in the photocatalytic degradation of emerging contaminants.

Among the wide range of sol-gel methods, to control the polymorphic structures of the nanoparticles, two soft-template assisted routes with either direct micelles (section 2.1.2) or reverse micelles (section 2.1.3) and an alternative template-free method (section 2.1.4) were proposed.

Two main strategies were attempted to improve the materials photocatalytic properties: i) Fe doping and ii) formation of heterojunctions between different polymorphic structures of TiO_2. (section 1.3.2 and 1.3.1)

The synthesis methods were described in detail, and the physico-chemical properties of obtained samples were discussed after an accurate analysis of the samples by different characterization techniques. (Chapter 4 and 5)

In (Chapter 6), the photocatalytic experiments results obtained during photocatalytic degradation of paracetamol, N-Phenylurea, simazine, and two azo dyes were proposed and discussed in detail.

During the whole study the possible interconnection between physico-chemical properties and photocatalytic efficiency were proposed and supported by the available literature.

Contents

List of Figures

List of Tables

1 TiO_2-based materials for photocatalytic application

Titanium dioxide (TiO_2) was discovered in 1791, but its first applications as a pigment are dated back to 1920. Since then, a wide range of applications have been proposed in the field of cosmetics, industrial pigments, biomedicine, and self-cleaning glasses.[1]

The importance of titanium dioxide for photocatalytic application started in 1972 when K. Honda and A. Fujishima discovered the opportunity to perform water splitting with TiO_2 electrode, and consequently, the material started to attract the attention of scientists for hydrogen production and photo/photo-electro assisted environmental remediation. [2], [3]

Nowadays, titanium dioxide, in virtue of its chemical stability and low toxicity, is currently used in a wide range of applications, from dye-sensitized solar cells to sensor devices and paints; most of all, TiO_2 is one of the most investigated photocatalysts, as it can decompose several organic/inorganic pollutants in both liquid and gas phases. [4]

1.1 Advantages of TiO_2 in photocatalytic processes

Heterogeneous photocatalysis is an advanced oxidation process (AOP) that has been the subject of many studies related to air cleaning and water purification. [5] AOPs generally imply the in-situ production of highly reactive species (i.e., H_2O_2, $OH^{\cdot}$, $O^{\cdot -}$, O_3) that allow the degradation of refractory organic pollutants into biodegradable compounds. Rather than stand-alone methods, AOPs are more effective when used before or after biological treatments. AOPs may imply using of nanomaterials (NMs) as either catalysts or photocatalysts, which improve the selective removal of the target pollutants.[6]

In the case of heterogeneous photocatalysis applied to water purification processes, the reactive oxidative species (ROS) are provided by the interaction

between the semiconductor and water. The elementary steps of photocatalytic reactions in water solution are [7] :

- Adsorption or secondary interaction of the target molecule from the surrounding environment on the photocatalyst surface;
- Light absorption with photon energy is sufficient to promote electron/hole separation in the photocatalyst.
- Migration of electrons (e^-) and holes (h^+) to the surface of the photocatalyst to participate in the redox process.
- Oxidation and reduction of H_2O molecules and O_2 adsorbed on the surface of the photocatalyst to form hydroxyl radicals (• OH) and superoxide radicals ($O_2^{-\cdot}$) by h^+ and e^-, respectively or direct interaction between e^- and h^+ with the adsorbed pollutant.
- The target molecule undergoes some redox reactions with ROS species, and the by-products are released in the solution.

Figure 1 reports a schematic representation of the photocatalytic degradation of pollutants.

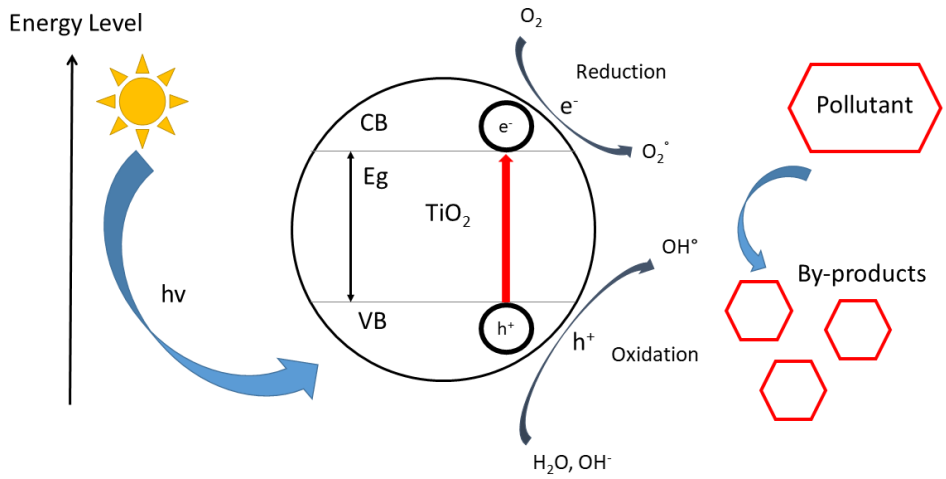

Figure 1. Schematic representation of heterogeneous photocatalytic degradation of pollutants under solar light. Adapted from [7]

Heterogeneous photocatalytic processes offer several advantages. Firstly, solar light can be used as an energy source. Furthermore, heterogeneous photocatalytic processes exhibit a rapid reaction rate and low energy consumption because these reactions occur under milder reaction conditions than traditional thermal catalysis

or other conventional treatment technologies like adsorption, membrane separation, chemical sedimentation, and bioprocesses. [7] Therefore, the utilization of solar energy to remove environmental pollutants holds significant importance in energy conservation and environmental remediation. Consequently, thousands of studies have been reported on the photocatalytic treatment of various pollutants, and new studies are being increasingly conducted in this regard. [7]

This work studied two essential aspects of heterogeneous photocatalytic degradation of pollutants: the nanostructured TiO_2 properties and their possible application in photocatalytic degradation of emerging pollutants under solar simulated light.

1.2 TiO_2 nanoparticles' physico-chemical properties

1.2.1 Polymorphic structures

TiO_2 has several polymorphs: although less-known amorphous TiO_2 and monoclinic TiO_2–B (space group C2/m) are gaining growing interest, anatase (tetragonal crystal system), rutile (tetragonal) and brookite (orthorhombic) are the most studied polymorphs, belonging to the I41/amd, P42/mnm, and Pbca space groups, respectively. Figure 2 summarises the conventional unit cells, lattice parameters, and volumes of anatase, rutile, and brookite polymorphs, as obtained from both Density Functional Theory (DFT) calculations and experiments.[8], [9]

Polymorph	Unit cell[a]	Method	a (Å)	b (Å)	c (Å)	V (Å^3)	$= \beta = \gamma$ (°)	Average E_g (eV)	DFT[1] E_g (eV)
Anatase	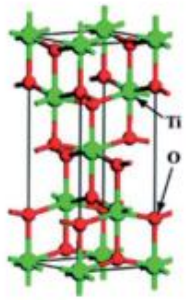	Experimental	3.796	3.796	9.444	136.084	90	3.2	2.38
		DFT	3.800	3.800	9.700	140.068	90		
		Deviation (%)	0.1	0.1	2.7	3.0	0		
Rutile	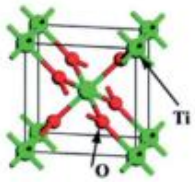	Experimental	4.602	4.602	2.956	62.603	90	3.0	2.13
		DFT	4.643	4.643	2.965	63.918	90		
		Deviation (%)	0.9	0.9	0.3	2.1	0		
Brookite	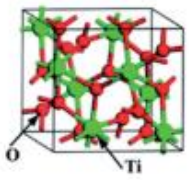	Experimental	9.166	5.436	5.135	255.858	90	3.1–3.4	1.86
		DFT	9.257	5.501	5.177	263.627	90		
		Deviation (%)	1.0	1.2	0.8	3.0	0		

Figure 2. Conventional unit cells, optimized lattice parameters, volumes (V) and relative deviations, and experimental and calculated average Eg for anatase, rutile, and brookite TiO_2. All deviations are less than 3%, which is consistent with the reliability of the DFT calculations performed in [8]–[10]. The Table is from ref [11]

The formation of different polymorphs depends on how the TiO_6 octahedral units share edges and corners: for instance, the TiO_6 units in anatase, rutile, and brookite share four, two, and three edges, respectively.[8]–[10]

The main difference among polymorphic structures depends on how many edges and corners of the octahedral units (TiO_6) are shared to form the unit cells.[8]

In anatase, the TiO_6 units share edges in a zig-zag mode along the three directions. In the rutile structure, the octahedral units share vertices along the *a* and *b* directions and vertices and edges along the *c* direction. In brookite, vertices and edges of the octahedral units are shared along the *a* and *b* directions while edges are on the *c* direction.[12]

These structural features differentiate the length of the Ti-O bond in three main polymorphic structures, and therefore the thermodynamic properties and structural stability of anatase, brookite, and rutile are different.[13]

Rutile is the most stable polymorphic structure at room temperature for bulk (size exceeding 100 nm) TiO_2 [2]. In recent studies, the order of thermal stability reported in the literature is rutile >brookite > anatase. [9] The anatase-to-rutile thermal transition for bulk TiO_2 is at ca. 600 °C in air, whereas for nanometric TiO_2, the reported transition temperature varies in a broad range (400–1200 °C)[14]

Another aspect influencing the polymorphic structure's stability is the crystallites' size. Anatase and rutile can be classified as stable when the crystallite size is below and above 11 and 35 nm, respectively, while brookite is stable inside that interval. [15]

The transition among polymorphic structures can be affected by other parameters like reaction conditions during the synthesis, such as the pH (in the case of synthesis from solutions) or exposed crystallographic planes [1]

The possibility to tune the transitions among the polymorphic structures opens a wide range of opportunities to obtain the optimal combination of polymorphic structures.

1.2.2 Electronic properties of TiO_2

TiO_2 is a semiconductor material; the main feature of the electronic properties of a semiconductor can be described by taking into consideration its band structure. A semiconductor has a band structure, roughly characterized as a series of energetically closed-spaced energy levels (the valence band, VB) and a second series of spatially diffuse, energetically similar levels lying at higher energy (the conduction band, CB). [16]

In semiconductors, the band gap or also called energy gap (Eg) refers to the separation between the energy of the lowest level of the CB and that of the highest level of the VB. The Eg parameter influences the semiconductor's behavior. The illustration of the distribution of the energy states in a semiconductor on both sides of Eg suggests the existence of a well-defined edge. The electrons in a solid occupy allowed energy bands separated by forbidden energy gaps. Two main types of VB-to-CB transitions are summarized (Figure 3) [17]:

- Direct transitions (allowed) when the participation of a phonon is not required to conserve momentum. Direct transitions (forbidden) take into account the small but finite momentum of photons and are less likely to occur.
- Indirect transitions, when at least one phonon participates in the absorption or emission process to conserve the momentum.

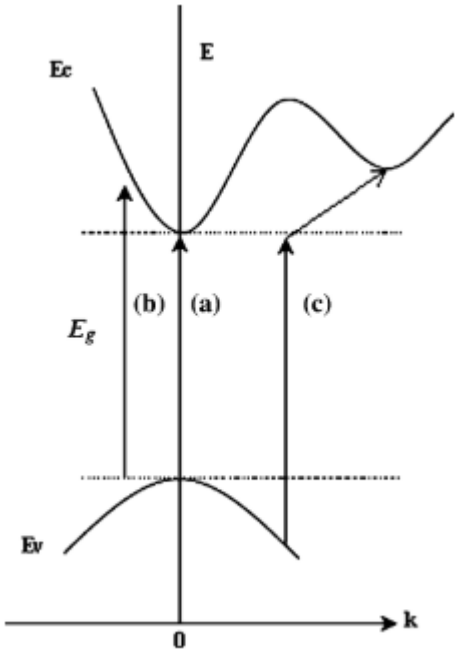

Figure 3. Simplified band transition representation: (a) allowed and (b) forbidden direct gap absorption of a photon with Eg energy can occur without the assistance of a phonon; (c) for the indirect gap, the assistance of a phonon is required. Adapted from [17].

Concerning the band structure of TiO_2, the density of states (DOS) is similar for the three main polymorphic structures. The valence band primarily consists of O 2p states and some Ti 3d states, suggesting a strong hybridization between O 2p and Ti 3d states. The conduction bands are mainly formed by Ti 3d states and a few Ti 3p and O 2p states. A strong hybridization between Ti 3d and O 2p states are also present in the CB, which causes the formation of the antibonding states. [18]

The Eg values depend on the polymorphic structure. The reported average values in the literature are ca. 3.0 eV and 3.2 eV for anatase and rutile, respectively, while the reported experimental Eg values for brookite span from 3.1 to 3.4 eV. [9] The average Eg values correspond to a direct transition for the anatase phase while for brookite and rutile, these energy values correspond to indirect electronic transitions. [9], [19]

These values of Eg correspond to electronic transitions that can be induced by the absorption of photons. The photons' energy depends on the wavelength; UV light includes wavelengths that span from 100 to 400 nm (12.39 to 3.09 eV), while visible light is composed of radiation between 400 and 700 nm (3.09 to 1.77 eV).

The solar light includes visible light, a small portion of UV light (ca 4%), and near-infrared radiation (NIR).

Therefore, TiO_2 absorbs below 380 nm and is mainly activated by UV light, being able to exploit only a small fraction (~4-5%) of the solar spectrum. A possible solution is to reduce the band gap and extend the light absorption towards the visible region by doping with several transition metal ions.[20]

1.3 Strategies to improve the photocatalytic properties of TiO_2

Recombination of energy carriers is one of the main drawbacks of TiO_2-based material for photocatalytic applications, together with the low amount of solar light that can be exploited by undoped TiO_2 having a large energy gap.

These two main topics lead to the reduction of the quantum yield (number of desired products produced per photon absorbed), which is the measure of the efficiency of a photocatalyst. [21]

1.3.1 Heterojunctions between polymorphs

Heterojunctions between different polymorphs of TiO_2 have attracted significant attention because they offer a good platform for tailoring the electronic properties of the photocatalyst. The development of interfaces among them can deeply affect the material properties. [22]

For example, heterojunctions between anatase and rutile commonly found in a commercial powder produced by Evonik (formerly Degussa) AEROXIDE® TiO_2 P-25 (P25) have been shown to promote good photocatalytic activity due to the possibility to improve charge separation and transfer of electron and holes among the interfaces. [23] The presence of electronic transfer among the interfaces was experimentally demonstrated by spectroscopy techniques like electron paramagnetic resonance (EPR). [24] The positive effects due to heterojunctions' presence request well-interconnected crystalline domains to allow the interchange of carriers.

The opportunity to obtain heterojunctions has led scientific research since the discovery of P25. However, most of the investigation was focused on anatase-rutile systems, while the role of brookite in mixed-phase samples is less known. In the literature, although, it was shown that the co-presence of brookite along with anatase or rutile improves photocatalytic activity.[25]–[27]

Focusing attention on heterojunctions within semiconductors makes it possible to discriminate among three types of schemes presented in Figure 4. The three different conventional heterojunctions are- type I heterojunction with a straddling gap, type II with a staggered gap, and type III with a broken gap. [21] Type I heterojunction is formed when VB and conduction band CB of semiconductor X is lower and higher than semiconductor Y's corresponding VB and CB energy levels respectevely. In contrast, with type II heterojunctions, the VB and CB energy levels of semiconductor X are both higher or lower than the corresponding VB and CB of semiconductor Y. In type III heterojunctions, both the VB and CB of semiconductor Y are lower/higher than the VB of semiconductor X.

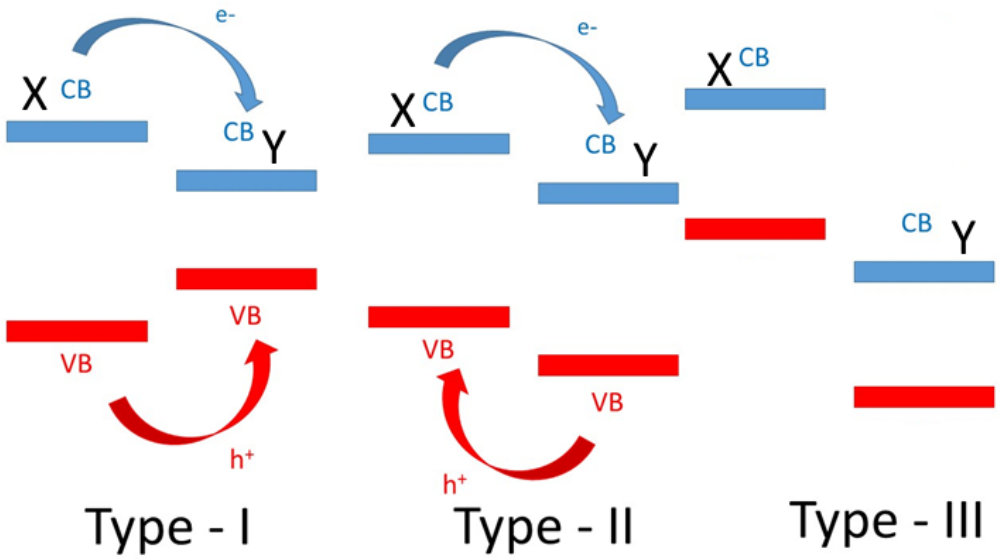

Figure 4. Illustration of the three different types of heterojunctions in a semiconductor : (a) type I, (b) type II, and (c) type III heterojunctions. Adapted from [21]

The mismatch of bands in type I heterojunction induces migration of photo-generated e^- and h^+ from semiconductor X to CB and VB of semiconductor Y, respectively. On the other hand, when type II heterojunctions are available, photo-generated e^- in semiconductor X will migrate into the CB of semiconductor Y, while h^+ will move from the VB of semiconductor Y into the VB energy level of semiconductor X; as such in this way, this configuration favors a more spatial charge separation. When the bands of the material show the mismatch in type III heterojunction, no charge carriers exchange is observed. [21]

Type II heterojunctions guarantee spatial separation of charge carriers and are typical of anatase-rutile systems with anatase positions of VB and CB positioned as type Y semiconductors and rutile bands positioned as X semiconductors Figure

4.[28] The type II heterojunction was proposed, also, for the anatase-brookite system with anatase acting, as X semiconductor (Figure 4) by Khedr et al. but more investigation are needed on this type of heterojunctions. [29]

In the literature, a wide range of synthesis methods have been proposed to obtain heterojunctions between polymorphs ranging from spray pyrolysis (P25) but also wet chemical methods such as hydrothermal synthesis and sol-gel processes. [30]

Overall, heterojunctions between polymorphs are widely considered an important strategy to reduce or delay the $e^-/\ h^+$ pairs recombination and consequently enhance the photocatalytic properties of TiO_2. [22]

1.3.2 TiO_2 doping: The case of Fe doping

TiO_2-based materials for photocatalytic application with solar light suffer from poor solar spectrum absorption, which contains only a minor fraction of UV light (ca. 4-5%). In contrast, the three most common polymorphs of TiO_2, namely anatase, brookite, and rutile, have average band-gap energies (Eg) in the UV range (of ca. 3.2, 3.4, and 3.0 eV), respectively.[31] One of the possibilities adopted to cope with this problem is doping with heteroatoms of the material to promote a red shift of absorption edge and improve its absorption of solar light. [32], [33]

In the wide range of heteroatoms used with TiO_2 are iron ions. Concerning Fe doping, this element is earth-abundant, non-toxic, and can be successfully introduced to different types of materials, such as TiO_2, due to the similar charge radius of Fe^{3+} and Ti^{4+}. [34], [35]

Iron doping in TiO_2 materials affects light absorption abilities by shifting the absorption edge toward the visible range by forming new levels within the TiO_2 band gap (Figure 5). [36]–[39]

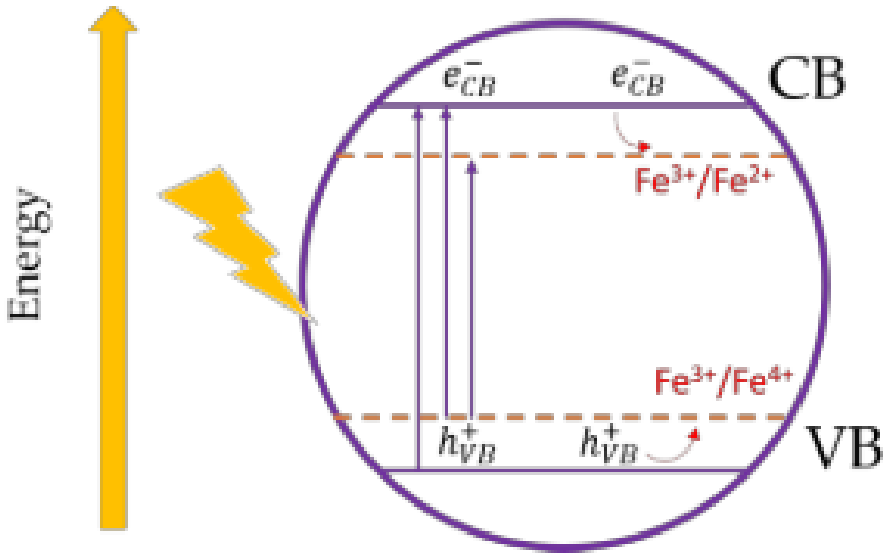

Figure 5. Processes occurring in Fe-doped TiO_2 upon interaction with light (adapted from Ref [31]

The presence of these mid-gap states induces a variation in the energy gap with new levels at different depths with the possibility of absorbing visible light by reducing the Eg value. [40]

However, the positive effects of Fe doping are not related exclusively to enhanced photon absorption: another important improvement of photocatalytic properties derives from the enhancement of the separation of photo-generated e^-/ h^+. [41]

The mechanism takes place in the bulk of the material where Fe atoms trap the photo-generated e^-_{CB} or h^+_{VB} (Figure 5), avoiding their recombination and giving rise to the following reactions [42]:

$$Fe^{3+} + e^-_{CB} \rightarrow Fe^{2+} \qquad \text{Equation 1.1}$$

$$Fe^{2+} + Ti^{4+} \rightarrow Fe^{3+} + Ti^{3+} \qquad \text{Equation 2.1}$$

$$Fe^{3+} + h^+_{VB} \rightarrow Fe^{4+} \qquad \text{Equation 3.1}$$

$$Fe^{4+} + OH^- \rightarrow Fe^{3+} + HO^{\cdot} \qquad \text{Equation 4.1}$$

Equation 1.1 and Equation 3.1 suggest evidence of the trapping effect induced by Fe presence. Fe ions interact with electrons or holes and prevent recombination

because they allow the species not involved in the reaction to reach the surface and promote the formation of ROS species. Furthermore, according to Equation 3.1 and Equation 4.1, in the presence of TiO_2, the photo-generated h_{VB}^{+}can react with Fe^{3+} species to produce (unstable) Fe^{4+} species, which can provide additional HO• species. [31]

The positive effects of Fe doping described before depending on the amount of doping introduced in the TiO_2 materials. An excessive amount of Fe ions introduced in the structure can induce disorder in the structure with peculiar mid-gap levels formation, promoting the charge carriers' recombination and inducing a decrease of photocatalytic properties. [42-44]

1.4 Water pollutants

Water and air are the most important resources for life on this planet. These essential resources are frequently contaminated by various toxic, organic, and inorganic compounds that can alter the water quality. [45]

The reduction of safe/unpolluted water can lead to scarcity of this precious resource. It is foreseen that water scarcity will affect around 2.273 billion people by 2050 [46].

Examples of substances that can be defined as pollutants include many compounds and substances from agrochemicals, pesticides, pharmaceuticals, and chemical industrial wastes.[47]

These pollutants can be detected in different amounts in the groundwater, watercourses, and drinkable water with common detection methods. Although some of these substances have been forbidden for many years, they can still be detected due to their stability.

An example of a study regarding the interaction between water micropollutants and the environment was performed by Schwarzenbach et al. and can be summarized by Figure 6, where the paths followed by a pollutant in the ecosystem are proposed.

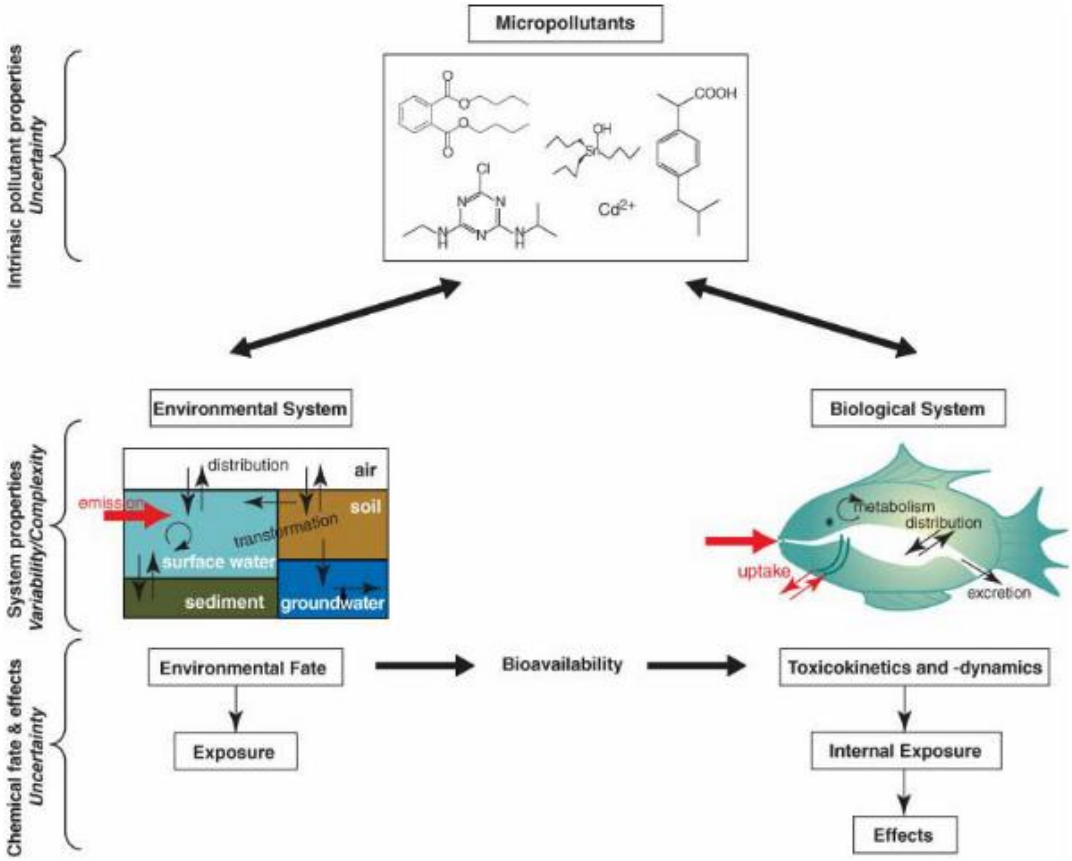

Figure 6. Environmental and correlated animal pollutants fate[48]

Pollutants interact with environmental and biological systems according to their intrinsic physicochemical properties and reactivate, yielding a characteristic pattern of environmental and internal exposure concentrations for each pollutant. [48]

Due to the peculiarity of single pollutants and the complexity of their fate in the ecosystem in this work, the attention was focused on a group of pollutants named “emerging contaminants”.

1.4.1 Emerging contaminants

Among water pollutants, a sub-category upon which scientists are focusing their attention is called emerging contaminants. This family of pollutants, also known as emerging organic contaminants (EOC)[49] or contaminants of emerging concern (CECs)[50], is a group of chemicals and their by-products which are nowadays detectable in water bodies all over the globe with very low dosages.

The effects of CECs contaminants are under investigation, but their definition is already clear: the emerging pollutants are anthropic-originated substances

detected in low concentration ng L^{-1} to μg L^{-1} levels. [51] Furthermore, these pollutants are presently not regulated (not submitted to a constant monitoring and/or emission limit control regime by the institutions) but can cause environmental damage and suspected detrimental effects on ecosystems and human health.[52] [49]

The effects of most of the emerging contaminants are relevant for human life because of the daily exposition. Notably, these substances are detected daily in wastewater treatment plant (WWTP) effluents and, therefore, they can reach water courses.[53]

The evidence of CECs' effects on the ecosystem moved the legislators to develop a strategy in order to tackle the problem.

The European Commission founded 2005 the NORMAN project to promote the work of universities, research centers, and industries to organize the data acquired. According to the NORMAN project, the most known CECs include pharmaceuticals, industrial compounds, personal-care products, biocides, plant protection products, and pesticides. Furthermore, every day according to the European Union database (REACH), daily-use products are included in 30000 to 50000 chemicals.[48] [50] These chemicals can be found in our food and drinking water. [50]

According to the NORMAN database, there are more than 700 compounds grouped into 20 classes of emerging pollutants: "surfactants, antibiotics and other pharmaceuticals, steroid hormones, and other endocrine–disrupting compounds (EDCs), fire retardants, sunscreens, disinfection by-products, new pesticides, and pesticide metabolites, naturally–occurring algal toxins" and other substances. [54]

In this work, the attention was focused on one common drug (paracetamol), two herbicides/pesticides (N-phenylurea and simazine), and two azo dyes (Acid orange 7 and Crystal violet). These compounds are categorized as EOC, and the possibility of degrading these substances with photocatalytic processes is investigated in Chapter 6.

1.4.2 Paracetamol

Among CECs, active pharmaceuticals ingredients (APIs) and pharmaceuticals and personal care products (PPCPs) are a worldwide concern due to the increasing world population and changes in personal habits. [52] PPCPs all together form the largest contribution to CECs, and the number of consumers is growing daily. [55] One of the worst problems of drugs and their by-products is the possibility,

according to their reactivity, to target the cells of organisms and, consequently, when dispersed in water, can easily react with non-target organisms.[56][57]

Paracetamol, acetaminophen or N-acetyl-para-aminophenol (Figure 7) is one of the most widely used analgesic and antipyretic medications. It can be found in a wide range of pharmaceutical products, either alone or in a formulation combined with other drugs. [58]

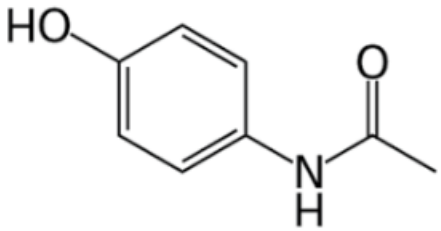

Figure 7. The structural formula of paracetamol

Paracetamol is available in different forms, from pills to effervescent tablets, suppositories, syrups, or even injections, and it is commonly available without any medical prescription.[59] According to the analysis performed a few years ago on raw urban wastewater, paracetamol was one of the most frequently detected chemical compounds in secondary effluents among analgesic drugs [60]. Furthermore, paracetamol appeared as one of the highest concentrations of APIs in the analyses of 258 rivers in 104 countries of all continents, including the Antarctic, thus affecting a population of 471.4 million. The research found acetaminophen with an amount almost constant on all the continents.[61]

Before the COVID-19 pandemic, paracetamol was detected even in drinking water: in the US, some years ago, scientists detected from 0.002 μg L^{-1} to 10 μg. L^{-1} of it in 7 % of the analyzed water sources.[61] Higher concentrations were detected in Europe in recent years, ranging between 0.260 to 0.010 μg L^{-1} in Spain and a concentration of 0.045 μg L^{-1} in the Marseille area[62]. Before the pandemic, scientists discovered an extremely high amount of 227 μg L^{-1} paracetamol in Rio Seke, Bolivia. [61]

During the COVID-19 pandemic, the situation worsened because paracetamol was chosen as one of the leading drugs for treating the first symptoms after infection.[63] The increased paracetamol consumption inevitably led to a significant increase in its occurrence in wastewater and drinking water sources.

1.4.3 Simazine and N-phenylurea

Simazine's IUPAC name is *6-chloro-N,N'-diethyl-1,3,5-triazine-2,4-diamine*, and it was widely used as an herbicide. Simazine belongs to the triazine family that comprehends the whole nitrogen-based herbicides family. Figure 8 reports the structural formula of simazine.

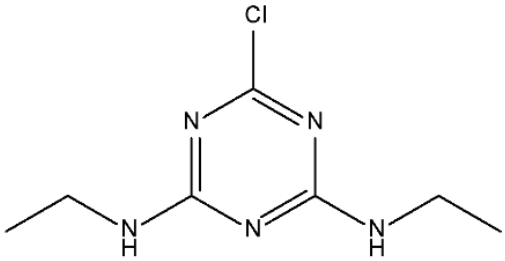

Figure 8. The structural formula of simazine

Simazine was discovered and approved in Switzerland in 1956 for applications on the railways' lines as an herbicide. After a few years, simazine was used for corn and other vegetables in order to control broad-leaved weeds and annual grass by photosynthesis inhibition.[64][65]

Since 1991, in Italy and Germany, simazine has been banned [66], and after a few years (2004), most of the other European countries implemented the same choice [67]. Just after 2020, along with atrazine (the most used triazine herbicide), simazine was banned in Hawaii and other US territories [68]. The decision to ban these compounds is correlated with evidence of possible effects on the endocrine system of organisms and the possibility to affect the reproductive organs: simazine has been categorized as toxic for humans and wildlife.

The most prominent issue of simazine is its persistent presence in surface and groundwater after many years of prohibition.[69]

A recent report by the European environment agency showed that simazine was detected in the water of more than 6000 sites, including 28 distinct countries, between 2007 and 2017. [70]

The other herbicide investigated was another nitrogen compound: N-phenylurea. N-phenylurea (NPU) belongs to the family of phenylurea herbicides (PUHs) used to inhibit the photosynthesis process of weeds in crop fields.[71]

NPU is well known by the name phenyl carbamide because of the phenol presence and carbamide functional group. Figure 9 reports N-phenylurea molecule. Depending on the ring halogen substitution of the molecule, we can differentiate

molecules belonging to the PUHs family, among which the most known are Diuron, Bromuron, and Fenuron.

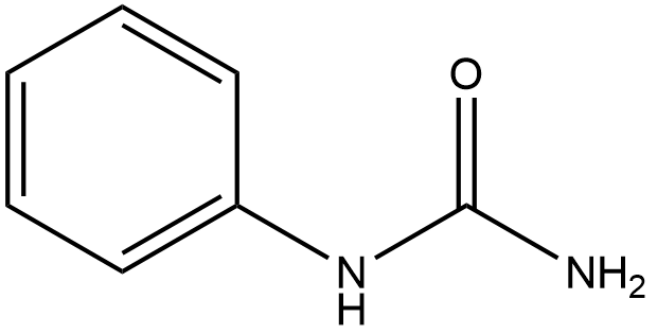

Figure 9. The structural formula of N-phenylurea (NPU)

The high wettability (10 mg/ml) and the application directly on the agricultural field make these herbicides already diffused worldwide in surface water and groundwater.[27]

1.4.4 Azo-Dyes

In recent years, the dyes industry has reached a high production increase for the textile, printing, leather, food, cosmetic, and chemical sectors. Consequently, an important amount of waste is discharged into water. An example of the massive production of dyes is in the United States of America, where the annual production is around 60,000 tons per year.[72]

Dye compounds often resist common wastewater processes, consequently affecting the ecosystem [73]. The most common drawback of dye pollution is the presence of chromophores groups, which can hamper the sunlight penetration in water, affecting the organisms living in it.

Dyes can be categorized as emerging pollutants for their resistance to being removed by common remediation methods and to their fate in the water[57]

Dyes can be categorized depending on different category, *e.g.*, the application field, and chemical formula. Azo-dyes are organic compound in which nitrogen atoms, included in the molecule, are as an azo group (-N=N-). These compounds represent *ca* 80% of the dyes released in the environment. An example of azo studied in this work is the Acid Orange 7 (AO7).

Figure 10 shows the structural formula of AO7, which is an anionic dye.

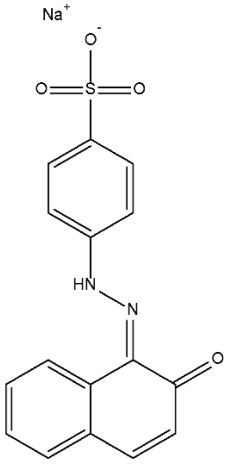

Figure 10. The structural formula of tautomeric form of acid orange 7 (AO7) [74]

Another important category of azo dyes is cationic dyes. In this work, the cationic azo dye chosen as a target molecule for the photocatalytic test was Crystal Violet(CV), used as a purple dye for tissues but also for polymers.[73] The structural formula of this cationic dye is reported in Figure 11

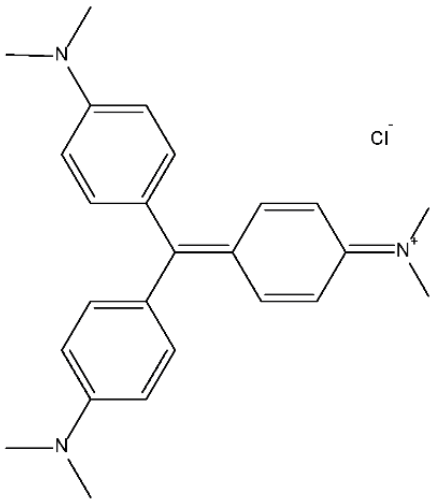

Figure 11. The structural formula of crystal violet (CV)

2 .Liquid phase methods for TiO_2 synthesis

TiO_2-based materials can be synthesized by several techniques depending on the application and the requested properties. The TiO_2-based photocatalyst's properties depend on a wide range of parameters ranging from porosity to optimized electronic properties. This complex system can be adjusted through synthesis and tuning the synthesis procedure and reactants selection. Some examples of photocatalyst parameters that can be controlled through a proper choice of synthesis method and experimental variables are: [75]

- Nanoparticles (NPs) morphology.
- Crystallite size and particle distribution.
- Polymorphic structures.
- Porosity and, consequently, specific surface area.
- Surface charge of the nanoparticles or aggregates.
- Electronic properties(i.e. mid-gap states and bandgap).

All these parameters affect the photocatalyst because they influence the interaction between the target molecule and the surface, like porosity and surface charge. In addition, other parameters influence the intrinsic properties of the photocatalysts, like polymorphic structures' presence and crystallographic properties that can play a role in the primary mechanism of a photocatalytic reaction, like electronic properties.

In the thesis, I focused my attention on TiO_2 NPs, and consequently, the synthesis methods should allow the synthesis of small particles with crystalline domains of nanometric size.

Examples of synthesis methods for NPs are spray pyrolysis, hydrothermal and solvothermal synthesis, which are similar to hydrothermal except that the primary solvent used is not water, chemical precipitation, and sol-gel methods. [76][77]

Apart from spray pyrolysis, the other methods can be categorized as liquid phase synthesis (wet chemistry or solution phase synthesis). These methods allow tuning the aforementioned properties in the nanoscale [78].

2.1. Wet chemistry for the synthesis of NPs

Wet-chemistry methods applied to NPs synthesis are classically divided into two events according to La Mer's theory: nucleation and growth of the nanocrystals. [79] Nucleation occurs when the concentration of monomers reaches a certain amount named nucleation threshold. At the threshold point, nuclei spontaneously form in the solution. [78]

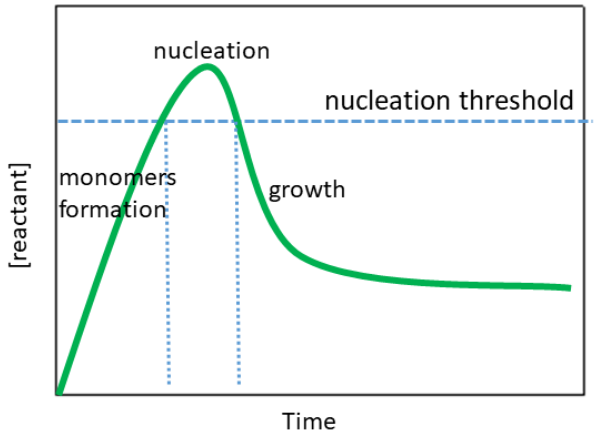

Figure 12. Illustrates La Mer's nucleation and growth condition of nanocrystals. adapted from [77]

The concentration at which the nucleation process starts depends on the specific system because many parameters, including the decomposition of the metallic precursor rate or a rapid variation of the concentration of a reactive species, influence it. [77]

After the nanocrystals' nucleation, the crystals' growth process might proceed in two main ways: monomer addition or Oswald ripening. In the first case, monomers are added onto the formed nuclei with consequent growth of the nanocrystals. In the case of the Oswald ripening phenomenon, the dissolution of small nuclei takes place with the resultant redisposition of monomers on the surface of larger nanoparticles. [77]

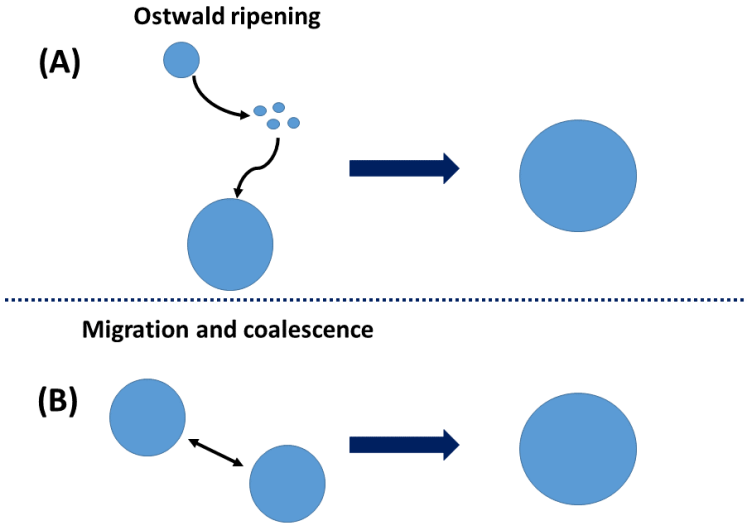

Figure 13. (A) Ostwald ripening model and (B) particle migration and coalescence model. Adapted from [80]

2.1.1 Sol-gel synthesis method

The sol-gel synthesis methods were first developed as an alternative to old classical synthesis method for glasses and glass ceramics at lower temperature. [81] Nowadays, the term sol-gel is used to describe many synthesis methods of solid materials like metal oxides (including TiO_2) starting from solution-state precursor (i.e.metal alkoxides). [81] Some of the most interesting advantages offered by sol-gel synthesis methods to metal oxides for photocatalytic applications, are proposed below:

- The sol-gel process offers control over the stoichiometry of multiphase systems, particle size, shape, and physico-chemical properties.
- Densification rate and porosity can be controlled by chemical modification of the precursors.
- Homogeneous and controlled doping of different metals can be made.

The sol-gel process involves two main steps: solution and gelation. The gelation phase can differ significantly depending on the adopted approach. [82] The so called “polymeric gels” are a three-dimensional network surrounding and supporting a continuous liquid phase. [83] On the other hand when the system is described as the “colloidal gels” the gelation process is described as a controlled destabilization of nanoparticle dispersion, and it can be described in the nanoscale. [82], [84]

The transition metal oxide, like TiO_2 nanoparticles, can also be synthetized by sol-gel method but the high chemical reactivity of their alkoxides has a influence on the typical sol-gel reaction paths.[81] On the other hand, silicon alkoxides were used since the beginning of sol-gel technological development due to the controllable reaction kinetic. [81] For this reason silicon alkoxides will be considered as an example of common reactions occurring during sol-gel processes.

During oxide nanoparticle synthesis from a liquid phase, the nucleation and growth processes start when a bonds network is formed. The generic M-O-M units (where M stands for Si atom) are the elemental part of the network structure which is commonly obtained in two main steps:[78]

- Hydrolysis.
- Polycondensation.

The first step (the hydrolysis) consists of the substitution of the alkoxide chain (OR) with hydroxyl groups Equation 2.1 to form the sol. [78]

$$\equiv M - OR + H_2O \rightarrow \equiv M - OH + ROH \qquad \text{Equation (2. 1)}$$

During the second step, the condensation of the hydroxylated species interacts with each other, alkoxide chains, or water molecules to induce the constitution of the amorphous network (gel). The condensation process by-products are mainly water and alcohol molecules, as summarized by the following three reactions:[85]

$$\equiv M - OR + HOH \rightarrow M - OH + ROH \qquad \text{Equation (2. 2)}$$

$$\equiv \mathrm{M} - OR + HOH \rightarrow M - OH + ROH \qquad \text{Equation (2. 3)}$$

$$\equiv M - OH + \equiv Ti - OH \rightarrow M - O - M + H_2O \qquad \text{Equation (2. 4)}$$

The transition metal oxide, like TiO_2 nanoparticles, can be synthetised by sol-gel method, but an high chemical reactivity of their alkoxides has a influence on the typical sol-gel reaction paths. [82]

In our case, the titanium sources were molecules of titanium alkoxides $Ti(OR)_4$: The macromolecular structure (gel) obtained by hydrolysis and polycondensation

was based on the repetition of the Ti−O−Ti unit but the chemical reactions leading to this system were more complexes.

The hydrolysis and condensation rates can be modified: for example, pH, modification or the presence of counter-anions, ligands, or polymers. An example of a pH adjustment strategy for TiO_2 properties tuning was proposed by Mutuma et al., where the addition of basic or acidic solutions influenced the polymorphic structures of titania nanoparticles obtained by sol-gel synthesis. [30]

Commonly, the final step of sol-gel synthesis methods is the heating treatment promoting the crystalline phase formation and removing the residual organic components. [75]

2.1.2 Three-block copolymer assisted sol-gel synthesis (M-TiO_2)

The three-block copolymer-assisted sol-gel synthesis is part of the soft-template-assisted sol-gel synthesis methods. These synthesis methods are based on the presence of structure-directing molecules like charged surfactants (either anionic or cationic), neutral surfactants (e.g., alkylamines), and block copolymers. [86]

The titanium precursor hydrolysis and condensation steps occur on the structure-directing agent (surfactant macromolecule). The resultant inorganic matrix development takes place by embedding the template structure, and consequently, the shape control of the inorganic matrix is obtained by tuning the organic structure formation. [87][86] The templating agent is commonly removed with a thermal treatment.

Here, the templating agent was a three-block copolymer. This synthesis procedure was proposed in the literature by Shamalia et al. l [88] and offered the opportunity to obtain a high specific surface area TiO_2 material suitable for dyes [89][20] and pollutants degradation[90].

The presence of a non-ionic three-block copolymer commercially named Pluronic P123 (P123) is responsible for the mesoporous structure typical of this material.

The molecular formula of P123 reported has a large organic non-polar chain and a hydrophilic part. The condensed formula is reported below.

$$HO(CH_2CH_2O)_{20}(CH_2CH(CH_3)O)_{70}\,(CH_2CH_2O)_{20}\,H)$$

The synthesis procedure involves the dispersion of this polymer in an ethanol solution. When P123 is dissolved in a solution, the copolymer reaches the critical micelles concentration (CMC), the concentration requested to have stable micelles.

In these systems, the organic macromolecules are organized to form micelles or aggregates in which the hydrophilic part is in contact with ethanol. Meanwhile, the titanium precursor was diluted in bi-distilled water and acetic acid to promote hydrolysis.

When the two solutions are mixed, the formation of micelles is promoted by the presence of ethanol (polar) and water (apolar). The peculiarity of this synthesis method is the presence of the macromolecular structures (micelles), which offer the surface upon which the 3D network, obtained from the condensation process, can be shaped, promoting the final mesoporous structure after a thermal treatment. [86]

Here, this type of synthesis has been applied to obtain both pure mesoporous TiO_2 (M-TiO_2) and iron-doped TiO_2 (M-TiO_2_x_Fe, where x stands for the nominal weight percentage of iron).

The undoped material synthesis was performed with the following schematic synthesis procedure summarized in Figure 14: solutions A and B were prepared simultaneously. Solution A was obtained by drop-wise addition of titanium butoxide ($Ti(OBut)_4$) to an aqueous solution containing acetic acid and water. Solution B was obtained by mixing Pluronic P123 and ethanol. Finally, Solution B was added to Solution A to promote micelle assembling and consequently exploit the effect of the templating agent on the inorganic matrix. The final powder was calcined in air to remove the remaining organic part and promote TiO_2 crystallization.

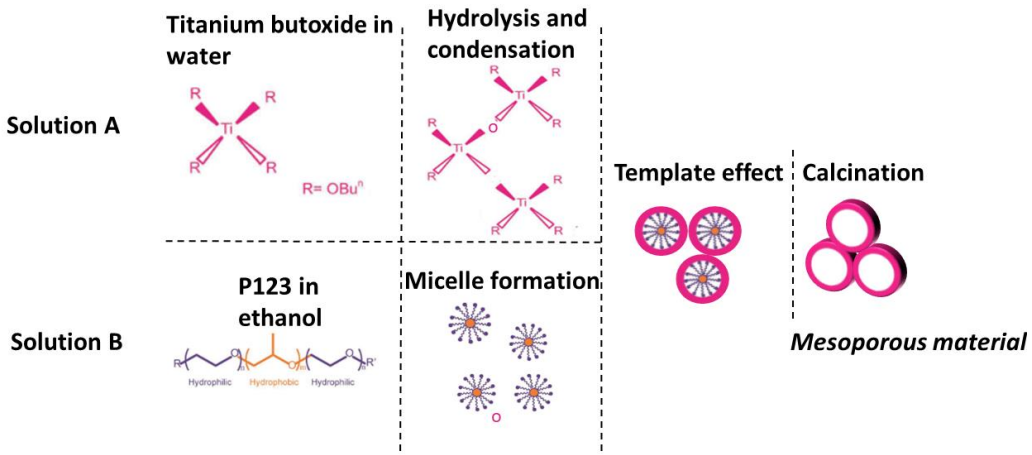

Figure 14. Simplified scheme of the steps leading to the production of ordered titania NPs(M-TiO_2) using three-block copolymer-assisted sol-gel synthesis (adapted from [86])

The same procedure was applied to dope TiO_2 was doped with iron at different weight percentages (Table 1). The iron precursor was iron(III) chloride hexahydrate

($FeCl_3 \cdot 6H_2O$), which was added to the B solution at the beginning of the synthesis. The presence of $FeCl_3 \cdot 6H_2O$ in the solution induced the pH lowering.

Table 1 Samples prepared with the three-block copolymer-assisted soft template synthesis

Sample name	A nominal amount of iron (% w/w)
M-TiO_2	0
M -TiO_2_ 1Fe	1
M -TiO_2_ 2.5 Fe	2.5

2.1.3 Reverse micelle-assisted sol-gel synthesis (RM-TiO_2)

The synthesis procedure is a soft template-assisted sol-gel synthesis method with the addition of surfactant forming, in this case, a reverse-micelle architecture in the bulk solution.

The basic principle of this synthesis method is using organic molecules (diblock copolymer) in an apolar solvent (cyclohexane) to create nano-reactors (the reverse micelles) within the solution. [91]

Such nanoreactors allow obtaining a controlled environment to tune NPs dimensions by controlling the ratio of surfactants and water introduced in the cyclohexane solution. [92] Furthermore, the nano-reactors offer a favorable environment for tuning the nucleation and growth processes and dopant atoms inclusion into the structure. [91]

The soft-template diblock copolymer chosen for this system is a non-ionic surfactant belonging to the Brij®-n family, where the letter n represents the number of [OCH_2H_2] groups repeated in the organic chain. The other parts are the hydroxyl group (hydrophilic) and the alkane chain. [93]

The peculiarity of these surfactants is the opportunity to tune the dimension of the reverse micelles, depending on the polarity of the head groups or the hydrocarbon tail extension. [93]

The dimensions of the reverse micelles depend mainly on the polar solvent-to surfactant ratio in an apolar solvent apart from the type of organic chain characterizing the organic molecules. The presence of double bonds among the organic chains or their length play a role in these systems. [93]

The selected surfactant for this synthesis method was the BriJ (O20) which has the condensed formula: $C_{18}H_{35}$ $(OCH_2CH_2)_n$ OH, n~20. BriJ (O20) was dissolved in cyclohexane in a conical flask with thermal control (oil bath) by stirring at 50 ◦C. Then, MilliQ water was added in the proper amount of the solution resulting in a transparent liquid kept at 50 °C. At this point, the solution was left 45 minutes under stirring to form reverse micelles inside the solution under stirring.

The formation of water-in-oil (w/o) microemulsion in which reverse-micelles act as surfactant-encapsulated aqueous nanoreactors were obtained. The titanium chosen precursor, in this case, was Ti(OBut)4. This precursor was then slowly added to the microemulsion and stirred to allow the process of hydrolysis and condensation inside the nanoreactors. Finally, the micelles were broken by adding isopropanol, and the resultant solution was sonicated. The final step was the calcination performed to remove the remaining organic part and promote the crystallization.

The amount of polar solvent to introduce (bidistilled water) inside the apolar solvent (cyclohexane) amount has been optimized by evaluating the final amount of TiO_2 obtained from the synthesis procedure. The obtained TiO_2 amount was compared with the stoichiometric expected amount and the material yield provided information on the hydrolysis and condensation processes taking place inside the nanoreactors.

This reverse micelles-assisted sol-gel method is summarized in Figure 15.

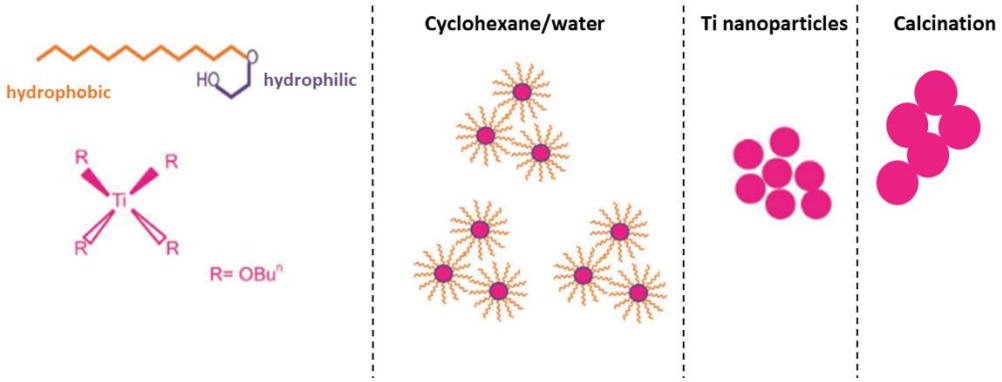

Figure 15. Simplified scheme of the steps leading to the production of TiO_2 NPs using reverse micelle-assisted sol-gel synthesis (adapted from [86])

The Fe precursor was iron(III) chloride hexahydrate salt to obtain Fe-doped samples. Different nominal weight percentages of $FeCl_3 \cdot 6H_2O$ were added to the

Milli-Q water (Table 2). Water contained in iron precursor salt was considered for stoichiometric calculations.

Table 2. Samples prepared with the reverse micelle-assisted soft template synthesis

Sample name	A nominal amount of iron (% w/w)
RM-TiO_2	0
RM-TiO_2_1Fe	1
RM-TiO_2_2.5Fe	2.5
RM-TiO_2_3.5Fe	3.5

2.1.4 Template-free sol-gel synthesis (AB and ABR)

Surfactants play a role in inducing mesoporosity or adjusting particle dimensions. However, high calcination temperature must eliminate these systems' organic components. Therefore, a template-free sol-gel synthesis method (without adding organic molecules) is proposed, which according to the literature, can lead to a disordered mesostructured. [86]

Following this template-free synthesis method, the main advantage was the opportunity to perform low-temperature calcination, as no organic molecules elimination was requested. Another consequence of low-temperature calcination was a crystalline structure control of titania NPs allowing the opportunity to obtain a expected polymorphic structures.

The absence of surfactants makes this synthesis method more eco-friendly than the previous one because the resultant solution does not contain organic macromolecules. [94] Furthermore, according to Mutuma et al., proposing the template-free sol-gel synthesis method adopted for this work, polymorphic structures, and crystallite size tuning are possible through pH control and proper calcination temperature. [30] We selected pH 2 as starting point because, according to Mutuma et al., this pH value offered the opportunity to obtain a significant amount of brookite. The effect of pH control on polymorphic structure tuning is well known in literature since it affects hydrolysis and condensation processes. [95][96]

During this template-free synthesis, we used titanium isopropoxide (TTIP)($Ti[OCH(CH_3)_2]_4$) as a titanium precursor.

The typical synthesis of undoped template free material TTIP was mixed with isopropanol and stirred. Then, MilliQ water was added to the mixture of TTIP and isopropyl alcohol under vigorous stirring to obtain hydrolysis and condensation. Then the solution was transferred into an autoclave, heated for a proper time, and cooled to room temperature. After cooling, the solution's pH was controlled by adding nitric acid (HNO_3) to obtain a sol at pH 2. Then, the sol was allowed to gel at room temperature, the obtained gel was washed with bi-distilled water, and the gel was dried.

The samples were calcined at 200°C showing anatase and brookite phases (AB) or 600°C for the sample showing anatase brookite and rutile polymorphic structures (ABR). The final powder was washed with water and ethanol three times after the calcination. The synthesis procedure is briefly summarized by Figure 16.

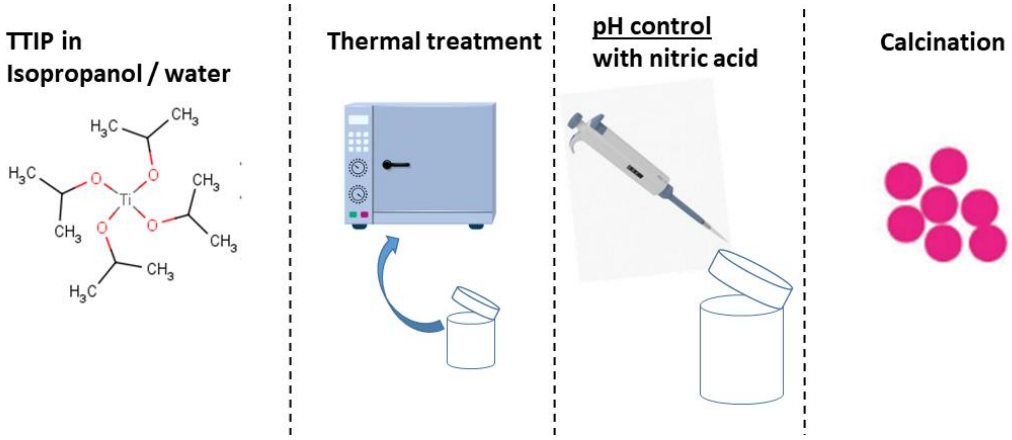

Figure 16. Simplified scheme of the steps leading to the production of TiO_2 NPs using reverse template-free sol-gel synthesis

The same procedure was followed to synthesize iron-doped AB samples by adding iron(III) chloride hexahydrate as an iron precursor.

The iron salt was dissolved in the MilliQ water before addition to the TTIP isopropanol solution. In this case, the solution's acidity was adjusted after considering the lowering of the pH performed by the iron precursor because we wanted to ensure pH 2 in the solution.

Table 3 summarizes the samples prepared by applying the template-free method.

Table 3. Samples prepared with template-free synthesis method

Sample name	**A nominal amount of iron (wt %)**	**Calcination temperature [°C]**
AB	0	200
ABR	0	600
AB_0.05_Fe	0.05	200
AB_1_Fe	1	200
AB_2.5_Fe	2.5	200

3 Characterization techniques

3.1 Introduction

The physico-chemical properties of the TiO_2 photocatalysts were studied by using different characterization techniques to assess how the peculiarities of the material can play a role in their photocatalytic applications.

The following list summarizes the characterization techniques and their purpose for the photocatalysts' analysis:

- Crystallographic information and polymorphic structure percentage were investigated by X-ray powder diffraction (XRPD). Consequently, quantitative phase analysis (QPA) comes from the Rietveld refinement method elaboration.
- Specific Surface Area (SSA) was measured by N_2 adsorption /desorption isotherms at -196°C and calculated by the Brunauer–Emmett–Teller (BET) equation. In addition, porosity analysis was obtained from isotherms through the Barrett–Joyner–Halenda (BJH) method.
- Energy Band Gap and localized surface states were investigated by diffuse reflectance UV-vis spectroscopy. (DR-UV-Vis).
- Surface properties were studied by Fourier-transform infrared spectroscopy (FTIR).
- Morphology was observed by high-resolution transmission electron microscopy (HRTEM) and/or field emission scanning electron microscopy (FE-SEM)
- Surface chemical composition was studied by X-ray photoemission spectroscopy (XPS).
- Chemical composition was studied by Energy-dispersive X-ray spectroscopy (EDX).
- The surface charge of the particles in solution and, consequently, their colloidal stability was analysed by the measurement of their ζ-potential.

3.2 X-ray powder diffraction (XRPD)

X-ray diffraction is a non-destructive technique and provides a wide range of information regarding:

- Crystal structure.
- Crystallographic parameters.
- Chemical composition.

The basic principle of this characterization technique is the exploitation of the capability of atoms, organized in a lattice, to behave as coherent scattering points of incident X-rays radiation. The intensity of the scattered radiation is proportional to the number of electrons surrounding the atoms.

When X-ray radiation reaches the sample, the re-emitted ray is scattered with a spherical wave front, and consequently, it can give rise to constructive and destructive interference. Furthermore, the scattering phenomena is typical of every material, with a periodic structure or not.[97]

Bragg's law (Equation 3.1) explains the diffraction of crystals by considering the position of the atoms arranged in a periodic structure. The diffracted beam is recorded as a function of geometrical constructions connected to material properties:

$$n\lambda = 2dsen\theta \qquad \text{Equation (3. 1)}$$

Where λ is the incident X-ray wavelength, n is an integer number, d is the spacing between the diffracting planes, and θ is the angle between the incident radiation and the diffracting planes, otherwise known as the Bragg angle. [98] The fulfilment of the Bragg's law is correlated with geometrical conditions between families of planes with an inter-planar distance d.

According to geometry, two atoms on two consecutive reticular planes will diffract two parallel waves when the difference in phase between the diffracted waves is proportional to their different path length; the diffraction, in this case, is constructive. Figure 17 reports the geometrical construction behind the constructive diffraction criteria. [98]

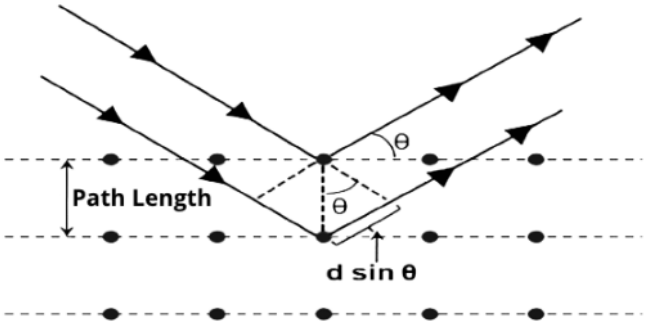

Figure 17. Geometrical derivation of constructive diffraction criteria through the Bragg's law.

Consequently, when the atomic spacing, correlated with the crystalline structure and the orientation of the crystals, satisfies the Bragg's law, we have a diffraction peak. The diffraction pattern is reported as a function of 2θ, which is double the incident beam angulation.

Figure 18 shows two diffractograms of two TiO_2 samples. The diffractogram (a) was obtained by analysing the AB sample (synthesized by a template-free sol-gel synthesis method) and the diffractogram (b) was obtained by analysing the commercial powder P25 (synthesized by spray pyrolysis).

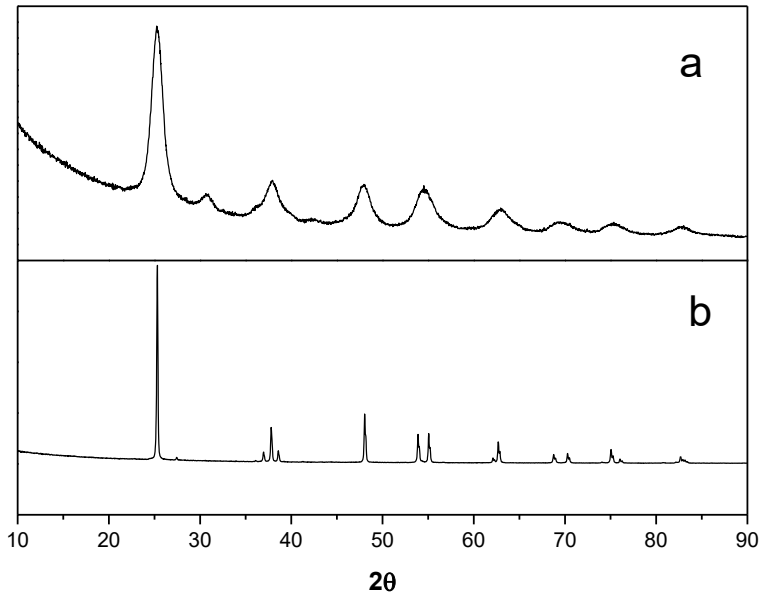

Figure 18. XRPD diffractograms of the AB sample (a) obtained by template-free synthesis method and P25 (b), a commercial sample obtained by spray pyrolysis.

Figure 18 shows the presence of different peaks correlated to peculiar polymorphic structures. The differences are due to the crystalline faces typical of peculiar polymorphic structures satisfying Bragg's law in correspondence with specific X-ray incident angles.[20]

Nonetheless, another important distinction between the diffractograms can be observed when considering the peaks broadening. This effect can be evidenced with crystallites smaller than 120 nm. [97] This widening of peaks reveals valuable insights into the crystallites' dimensions and the nanocrystals' strains.

The average size of nanocrystallites in nano-crystalline materials can be determined by analysing their diffractogram. The relationship between the size of crystallites and the width of diffractogram's peaks was first proposed by Paul Scherrer and is now widely known as the Scherrer equation. [99]

$$D = \frac{K\lambda}{\beta cos\theta} \qquad \text{Equation (3. 2)}$$

Where D is the particle size (in nm), λ is the X-ray wavelength (nm), β is the peak width of the diffraction peak profile at half maximum height resulting (FWHM) from small crystallite size (radians), and K is a constant related to crystallite shape, generally taken as 0.94. [100]
There are two essential factors affecting peak broadening: instrument- and sample-dependent effects. To decouple the two contributions is necessary to collect a diffraction pattern of a standard material. [100]

Once calculated the instrumental correlated broadening, the average crystalline size can be determined by fitting a plot obtained by applying the Sherrer formula to the diffractogram' peaks.

Figure 19 shows the plot obtained by application of the Sherrer formula to the diffractogram of the AB sample reported in Figure 18 (A). The slope of the fitting curve provides the average dimension of crystallites (D).

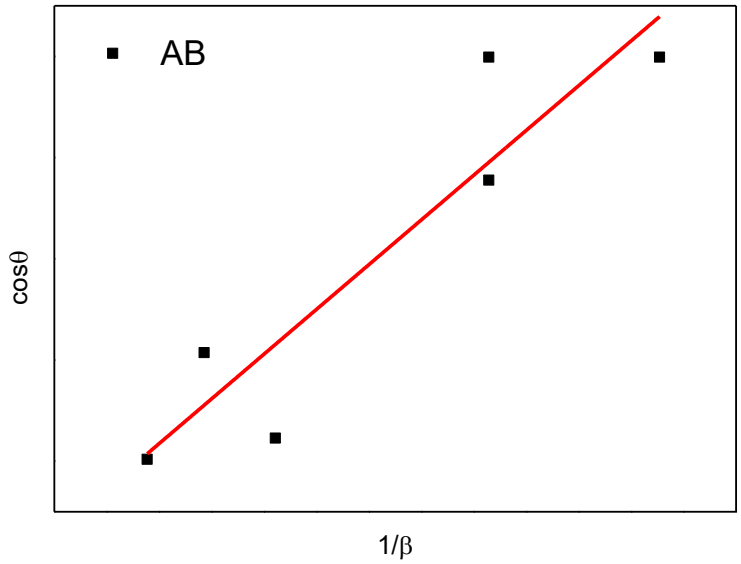

Figure 19. Scherrer plot of the AB sample. The red line represents a linear data fitting, and the crystalline size (D) is extracted from the slope of the fitting line.

By mathematical elaboration, the Scherrer plot can be converted into the Williamson-Hall (W-H) plot.

The W-H method does not follow a $1/\cos\theta$ dependency as in the Scherrer equation but instead varies with $\tan\theta$. This fundamental difference allows the separation of the strain-induced broadening component. This opportunity is possible because the contribution to broadening due to crystal imperfections and distortion is proportional to $1/\tan\theta$. [100] The two contributions were considered additive, and the plot obtained from the mathematical elaboration of the Scherrer equation was $\beta\cos\theta$ versus to $4\sin\theta$. The intercept of the fitting curve provided the average crystalline size determined by the W-H method.

Another important feature of XRPD analysis is the quantitative phase analysis (QPA) that provides the percentage of polymorphic structures in the analyzed sample. In this work, QPA was obtained by applying the Rietveld refinement method to the diffractograms.

The primary improvement of the Rietveld method on the nanocrystal analysis was overcoming the issues due to overlapping peaks occurring when microcrystalline powder, with many randomly oriented crystallites, was analyzed. [101]

Rietveld proposed a method to overcome this problem by obtaining the fitting of the measured diffractogram by changing several parameters, including various contributions such as the background, crystal lattice and symmetry, crystal structure, microstructure, instrumental factors, and others. [101] Different software offers the opportunity to execute such fitting operations by changing those parameters.

In this work, the X-ray powder diffraction (XRD) patterns were measured on an X'Pert Philips PW3040 diffractometer (Panalytical, Almelo, The Netherlands). The X-ray radiation was emitted by a Cu Kα source (2θ range = 10–100°; step size = 0.026° 2θ and time per step = 0.8 s). The obtained XRD patterns were indexed using the Powder Data File database (PDF 2000, International Centre of Diffraction Data, Newtown Square, PA, USA). The QPA was obtained using the full-profile Rietveld method (X'Pert High Score Plus 3.0e software). The average crystallite size was determined according to the Williamson-Hall plot (X'Pert High Plus 3.0e software Score).

3.3 N_2 adsorption-desorption isotherms at -196°C

The analysis of nitrogen adsorption-desorption measured at -196°C is one of the main techniques used for the surface characterization of materials.

There are different models used to describe gas adsorption on solid surfaces. One of the most used theories was proposed by Langmuir more than 100 years ago.[102]

According to Langmuir's adsorption theory, a material surface can be described by a certain number of adsorption sites interacting with gas molecules. Langmuir wrote his kinetical model based on two assumptions: i) the gas and adsorbed phases behave ideally (i.e., without intermolecular interactions), and ii) every binding site can be considered identical. [102]

One of Langmuir's theory's common applications is the specific surface area (SSA) measurement of microporous solids.
Another equation widely used for the estimation of SSA was proposed by Brunauer, Emmett, and Teller, and it is known as the BET equation reported in Equation (3. 3) in a common linearized rearrangement. [102]

$$B = \frac{P/P_0}{N_a(1 - P/P_0)} = \frac{1}{\Gamma_c} + \frac{c - 1}{\Gamma_c}(P/P_0) \qquad \text{Equation (3. 3)}$$

Where P/P_0 is the saturation pressure, Γ_c is the number of surface sites, c is the BET constant, B is a simple BET variable and N_a is the amount of gas adsorbed.

Brunauer, Emmett, and Teller described three regions along the adsorption-desorption isotherms reported, as an example, in Figure 20. The first part of the isotherm has a concave trend (region 1), and it is typical of low pressure, a linear region at intermediate pressure (region 2), and a convex region at high pressure (region 3). Within region 2, the values valid for evaluating the SSA from the BET equations can be extracted. [102]

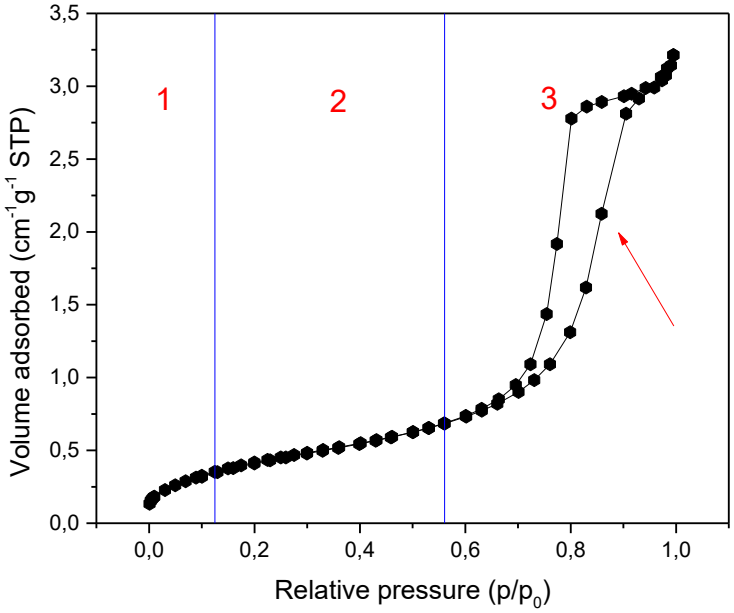

Figure 20. Typical isotherm of a mesoporous TiO_2 material, namely an undoped TiO_2 sample synthesized by three-block copolymer assisted sol-gel synthesis method

The BET model has been developed to estimate the SSA of materials, and it is appropriate for materials with mesopores (pore diameter of 2~50 nm).

The isotherm shape provides information regarding the material porosity and, according to IUPAC, can be categorized into six types. Figure 21 shows the proposed updated classification of physisorption isotherms according to the IUPAC technical report [103].

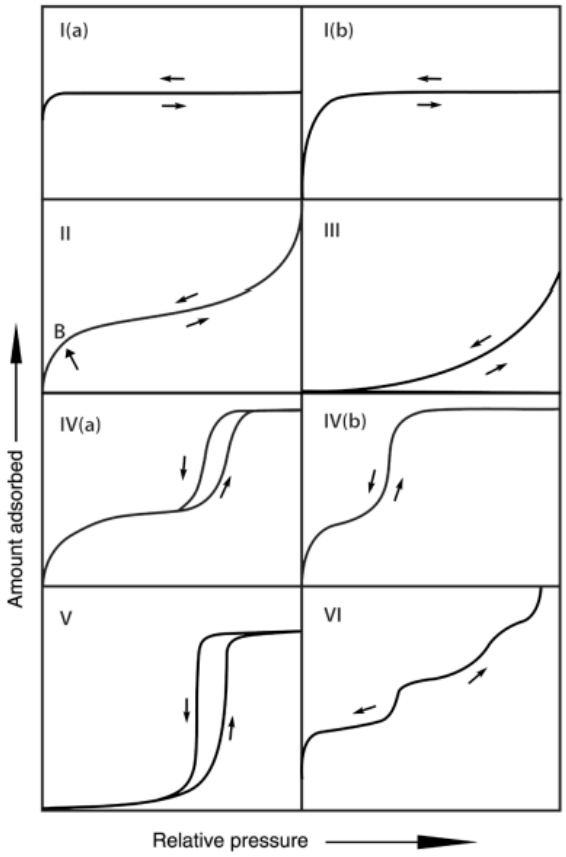

Figure 21. Classification of physisorption isotherms according to the IUPAC report. Adapted from ref. [103]

Mesoporous materials commonly show type IV isotherms, where the presence of pores induces an alteration of the condensation pressure of the gas. [104]

Types IV and V shapes of adsorption isotherms provide evidence that the complete, or almost complete, filling of the sample's pores occurs at a pressure lower than the vapor pressure of the gas. [104]

Concerning porosity analysis of the material, the most important features are the pore size distribution, pore geometry, and total pore volume.

The shape and the distribution of pores influence the shape of hysteresis loop. Commonly pores are divided into slit pores and ink bottle pores. In the former case the pores have the same geometry for the whole extension of the cavity while, in the latter case, the neck of the pores are smaller than the inner part. Different pores geometry induce peculiar condensation and evaporation processes.[105]

The Barrett–Joyner–Halenda (BJH) method can be used to evaluate the pore size distribution. This classical method for mesopores analysis was based on the Kelvin equation, which provides a connection between the pore dimension and the pressure of gas condensation. The Kelvin's law predicts that pore condensation shifts to a higher relative pressure with increasing pore diameter and temperature. In this work, the pores size was obtained by applying the BJH model to the isotherms' desorption branch. [106]

In this work, N_2 adsorption/desorption isotherms were measured at −196 ◦C on titania powders pre-outgassed at 150 °Cto remove water and other contaminants with the instrument Micromeritics ASAP 2020Plus, Micromeritics, Norcross, GA, USA.

3.4 UV-vis spectroscopy

UV-vis spectroscopy is a technique that analyses the discrete wavelengths absorbed, transmitted, or scattered by a sample interacting with UV, visible, and near-infrared (NIR) radiations.

The technique allows studying the electronic transitions, promoted by UV-vis source, in a sample. The studied sample can be solid, liquid or even in gas phases. Depending on the experimental conditions, the electronic transition information collected, can be exploited qualitatively or quantitatively.

3.4.1 UV-Vis spectroscopy applied to liquid solutions

Ultraviolet–visible (UV–vis) spectrophotometry is mostly a quantitative analytical technique correlated with the absorption of near-UV or visible radiations by chemical substances in a liquid solution.

The light absorption by molecules induces rotational and vibrational motions apart from purely electronic transitions typical of atoms inside the molecules. [107] Such electronic transitions are described by bands observed by UV-Vis spectroscopy analysis, and the Lambert-Beer law (Equation (3. 4)) summarizes the relationship between the absorption of the bands and the concentration of the investigated molecules.

$$A = \varepsilon bc \qquad \text{Equation (3. 4)}$$

Where A is the absorbance of the solution, ε is the molar absorptivity (mol^{-1} cm^{-1}), b is the path length of radiation through the absorbing medium (cm), and c is the molarity of the solution (mol L^{-1}).

Figure 22 shows the UV-Vis spectrum obtained for a paracetamol (APAP) solution with a 0.01mM concentration. The spectrum shows two bands at 194 nm and 243 nm, readily assigned to the $\pi \rightarrow \pi^*$ and the $n \rightarrow \pi^*$ electronic transitions of the aromatic ring and the C=O group, respectively.[59]

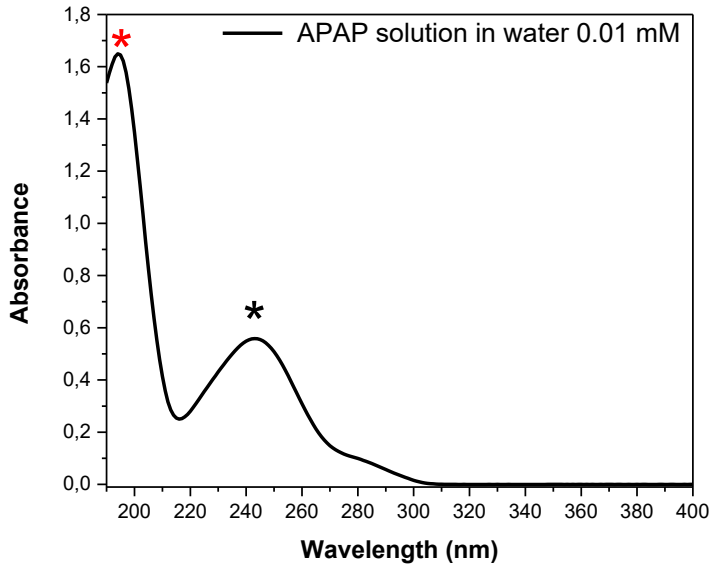

Figure 22. UV-Vis absorption spectrum of the 0.01 mM paracetamol aqueous solution. Absorption bands can be assigned to the $n \rightarrow \pi^*$ transition of the C=O group (black asterisk) and the $\pi \rightarrow \pi^*$ transition of the aromatic ring (red asterisk) [108]

The concentration of the solution makes feasible a quantitative analysis of the data. The quantitative data analysis is possible because, according to Lambert-Beer law, the concentration of the solution is proportional to the absorbance recorded in the spectrum. Furthermore, spectrum bands are due to the molecule's electronic transitions; a decreasing band intensity can be directly correlated with the reduced paracetamol solution's concentration.

In this work, the UV-Vis spectra were collected on a Cary 5000, Varian Instruments (Mulgrave, Australia) UV-Vis-NIR spectrophotometer.

3.4.2 Diffuse reflectance UV-Vis spectroscopy (DR-UV-Vis)

This spectroscopic technique offers the opportunity to analyze powder samples. The electronic transition of a solid sample is recorded as a function of the wavelength emitted by the instrument.

The diffuse reflectance UV-Vis spectroscopy spectra can be plotted by considering the Kubelka–Munk function reported in Equation (3. 5).

$$F(R_\infty) = \frac{(1 - R_\infty)^2}{2R_\infty} = \frac{K}{S} \qquad \text{Equation (3. 5)}$$

Where R_∞ is the fraction of incident UV-Vis light remitted by the layer considered infinitely thick a sample. On the right side of the equation, the two coefficients represent; S, the scattering coefficient, and K is the molar absorption coefficient when we assume an "infinite" thick layer. [109]

Figure 23 shows an example of the Kubelka-Munk (K-M) curve obtained by DR-UV-Vis analysis of the Titania sample obtained by the template-free sol-gel synthesis method (AB).

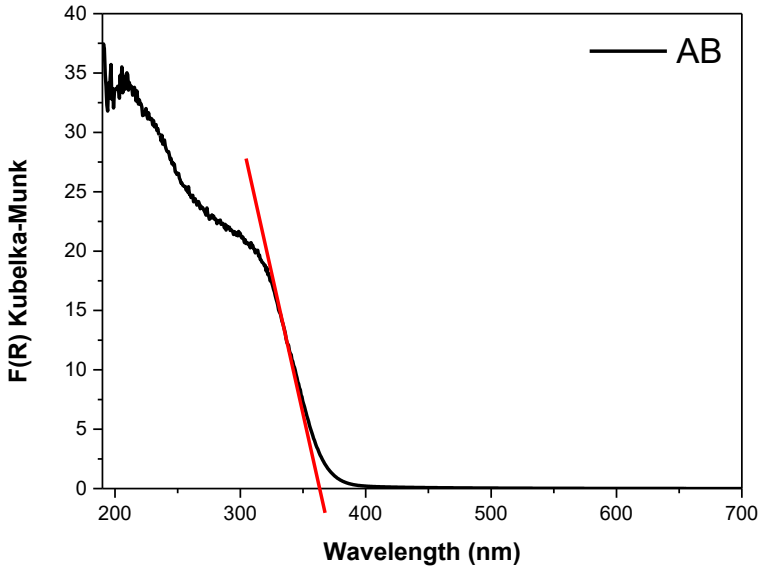

Figure 23. K-M curve obtained by DR-UV-Vis spectroscopy analysis of the AB sample

One of the most important pieces of information from this plot is estimating the sample's energy gap (Eg) value. This value was extrapolated from the onset of the curve by fitting with a line (red line) the linear part of the K-M curve.

Eg values can be extrapolated more precisely using the Tauc's plot method. This mathematical elaboration of the K-M curve considers the type of electron transition (indirect or direct) of the material we analyze and provides a curve.

When we consider a material with a direct band gap, according to the literature, Tauc's plot is obtained by plotting (F(R)*hν)2) versus hν, whereas in the case of an indirect band gap material, the plot is obtained by plotting (F(R)*hν)1/2) versus hν.[17]

Figure 24 shows the Tauc's Plots extrapolated by mathematical calculation from the K-M curve proposed in Figure 23 obtained by DR-UV-V analysis of the AB sample. The Tauc's plot was calculated and plotted considering an indirect band gap material (left) and a direct band gap material (right). The red lines are the linear fitting applied to the linear part of the plots used to obtain the Eg values.

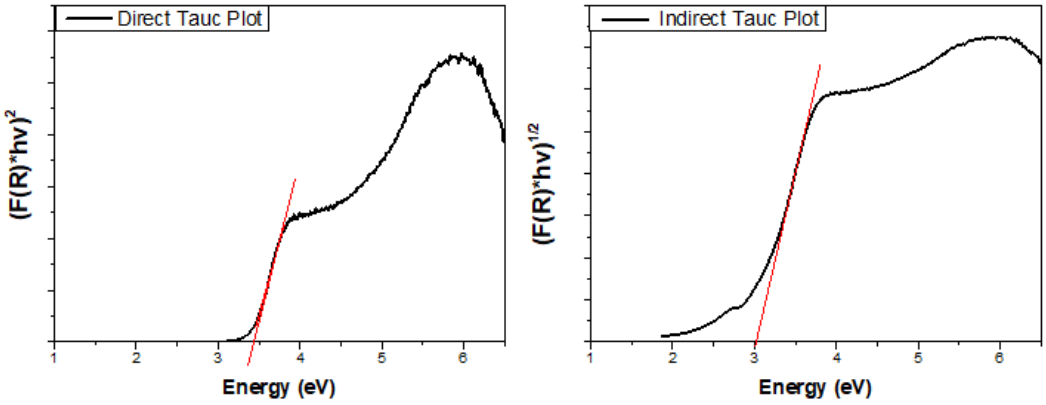

Figure 24. Tauc's plot calculated and plotted considering an indirect band gap of AB sample(left) and indirect band gap (right)

Both Tauc's plots were obtained by mathematical elaboration of the K-M curve reported in Figure 23: a sample can be considered a direct or an indirect semiconductor depending on the material's intrinsic properties or by the investigated electronic transition. [110]

When the polymorphic structure composing the material is known commonly one of the two plots is chosen to measure the Eg value. In this case, the AB sample was composed of 80 % of anatase which is a material showing an indirect band gap. For this reason, we considered the Tauc's plot obtained by applying the mathematical elaboration for indirect semiconductors.

In this work, the powder samples' Diffuse Reflectance (DR) UV-Vis spectra were collected on a Cary 5000 UV-Vis-NIR spectrophotometer (Varian Instruments, Mulgrave, Australia) equipped with a DR sphere.

3.5 Fourier-transformed infrared spectroscopy (FTIR)

The FTIR analysis is based on the vibrations induced by the infrared radiation in species (atoms, molecules), physisorbed or chemisorbed at the material's surface. These information are suitable for analysing materials' surfaces.

Molecular vibrations depend on the geometry of the molecules; they can range from the simple coupled motion of the two atoms of diatomic molecules to the most complex motion in a large polyfunctional molecule.

Each mode of vibration involves approximately harmonic displacements of atoms from their equilibrium positions, and the potential energy of those atoms can be calculated by Equation (3. 6).

$$V_{iv} = hf_i\left(v_i + \frac{1}{2}\right) \qquad \text{Equation (3. 6)}$$

Where h is Planck's constant, f_i the fundamental frequency of the particular mode, and v_i the vibrational quantum number of the I mode. [111]

The modes of vibration can be divided into two main categories :

- Stretching (where the interatomic distance and hence the bond length are affected)
- Bending (where the slant between the two bonds is altered).

Stretching modes can be divided into symmetric modes, where the two atoms simultaneously move closer and away from the central atom, and anti-symmetric modes, where the two atoms move in opposite directions concerning the central atom. [112]

Bending vibrations can be divided into four types of motions;

- rocking (the two atoms moving on a plane either clockwise or anti-clockwise).
- Scissoring (both atoms simultaneously move toward or away from each other on the same plane).
- Wagging (out-of-plane, where both atoms simultaneously move like a V sign back and forth).
- Twisting (out-of-plane, where one atom moves forward while the other moves backward).

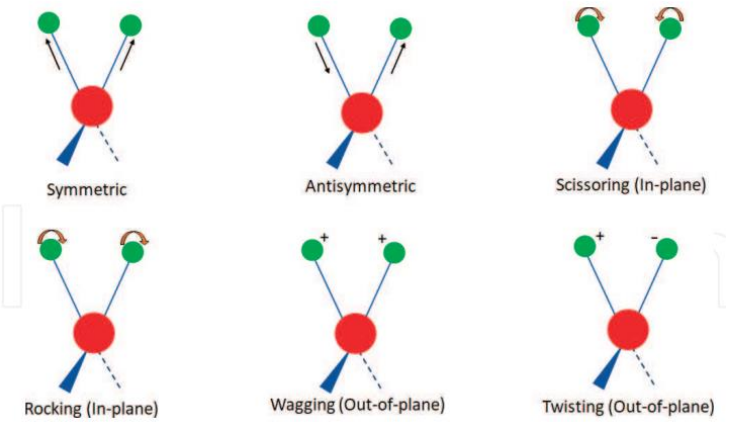

Figure 25. Bending vibration types adapted from ref [112]

Figure 26 shows a spectrum of a TiO_2 material. The sample analyzed, M-TiO_2, was studied by FTIR spectroscopy after evacuation at room temperature (black curve) at 100°C (blue curve) and at 200 °C (red line), and the resulting spectra show three main regions:

- 3500-2700 $cm^{-1,}$ broadband correlated to hydroxyl groups chemically bonded at the surface of TiO_2
- 1700-1100 $cm^{-1,}$ the bands are assigned to adsorbed carbonates and bi-carbonate species.
- < 1000 cm^{-1} modes of vibration typical of the lattice (also known as crystalline cut-off).

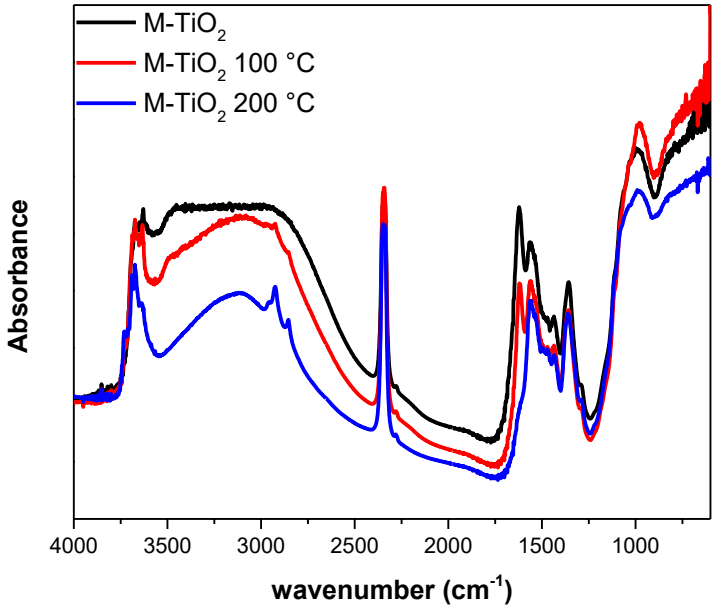

Figure 26. Typical FTIR spectra of a TiO_2 sample. The M-TiO_2 sample was outgassed at room temperature (black curve), at 100 °C for 1h (blue curve), and at 200 °C (red curve)

The evacuation processes at room temperature were used to remove weakly physisorbed water, without further perturbing the surface. [20]

The experimental settings also offered the possibility to outgas the sample during a thermal treatment to reduce the molecules physisorbed on the surface.

Finally, with the available experimental setting, it was possible to dose gasses/vapours inside the quartz cell where the sample was placed. Gas-solid interaction guarantees the possibility of investigating the peculiarity of surface species.

In a typical FTIR experiment with gas dosing, the probe gas/vapor was dosed stepwise at the increased pressures up to certain pressure, with spectra taken at each dosing step. Following saturation of the reactive sites on the surface, the cell was evacuated stepwise, with spectra taken at each evacuation step to follow even the desorption process of probe gas/vapor. [113]

In this work, the Fourier transform infrared spectroscopy (FTIR) spectra were recorded in the mid-infrared region (between 400 and 4000 cm^{-1}) at 2 cm^{-1}

resolution on a Bruker Equinox 55 spectrophotometer (Bruker Italia SrL, Milano, Italy) equipped with a mercury cadmium telluride (MCT) cryodetector.

The samples for IR measurements, were shaped into thin, self-supporting wafers (~2 mg cm^{-2}) by pressing proper amount of powder. The wafers were placed into gold sample holder properly adapted to allow the IR beam to cross the sample.

3.6 Electron microscopies

Optical microscopic techniques are based on the interaction of light with matter. The optical radiation depending on the wavelength, offers the opportunity, with the help of a lens, to observe samples with a resolution of 88 μm. [114]

The improvement in microscopy techniques was proposed in the 20th century when physicists discovered that particles have a wavelike character, and De Broglie proposed that their wavelength is given by

$$\lambda = h/p = h/(mv) \qquad \text{Equation (3. 7)}$$

Where h is the Planck constant = $6.626*10^{-34}$ Js; p represents the electron's momentum while m and v represent the electron's mass and speed. [115]

Electrons have an electric charge; consequently, the magnetic lens substituted the optical lens. Depending on the voltage applied, is possible to modulate the resolution and the different information obtained by these techniques.

With accelerated electrons, in the case of high-resolution transmission electron microscopy (HRTEM), a wavelength of less than 0.0027 nm can be obtained with a tremendous increase of resolution at the point to observe atoms.

The interaction between matter and accelerated electrons provides different information. Consequently, instruments and sample preparation are deeply correlated with the aim of the analysis. Figure 27 shows the wide range of information the interaction between electrons and matter produces.

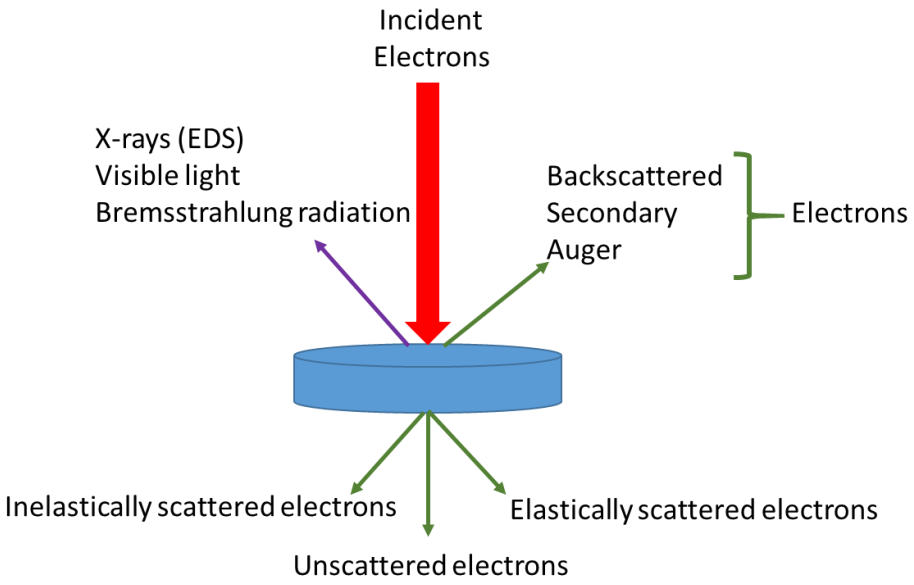

Figure 27. Interactions between electrons and matter adapted from [116]

Different detectors and instrument peculiarities offer the possibility of obtaining the requested information.

3.6.1 Field emission scanning electron microscopy (FE-SEM)

Field emission scanning electron microscopy (FE-SEM) is used to obtain microstructure images of materials.

The field emission scanning electron microscope (FE-SEM) is a type of electron microscope used to obtain images of the sample surface by scanning the (conductive) sample with a high-energy beam of electrons. [117]

Electrons are emitted in a range between 10kV and 40kV by a field emission gun. The peculiarity of field emission guns is the opportunity to produce up to 1000x the emission of a tungsten filament. [118]

After the electron beam's emission, electrons are confined and focused into a reduced wavelength range beam using magnetic lenses.

Finally, detectors of each type of electron emitted from the surface collect the signals to produce a micrograph of the specimen. [119]

A high vacuum is also needed for the quality of the images composed by collecting the emitted secondary and backscattered electrons perturbed by molecules in the chamber.

FE-SEM can also be equipped with an Energy Dispersive X-Ray Spectroscopy (EDX). This equipment offers the opportunity to map the surface and obtain information on the elemental composition of the samples. The deepness of this signal goes up to 1 μm in the models.

In this work, the FE-SEM images were collected by a Merlin FESEM instrument (Carl-Zeiss AG, Oberkochen, Germany) equipped with an EDX probe (Oxford Instruments, Abingdon, UK) for semi-quantitative elemental analysis.

Samples were covered by Ag thin layer to enhance the conductivity of the materials with a sputter coater Q 150T S (Quorum). The sputtering time chosen was 20 seconds at 30 mA.

3.6.2 High-resolution transmission electron microscopy (HRTEM)

Transmission electron microscopy (TEM) and high-resolution transmission electron microscopy (HRTEM) work with transmitted electrons.

Electronic microscopes comprise a column in which the electron beam emitted from a source is accelerated and collimated. Then, the whole system is kept under a vacuum, and magnetic lenses are positioned to reach the sample with a beam of electrons with a reduced wavelength range. [120]

The accelerating voltage in transmission electron microscopy can range between 100 kV to 1000 kV, and consequently, the resolution is well below the nm according to the De Broglie equation. [121]

The samples can be prepared depending on the material (Z of the atoms composing the sample) and the electron energy used. It is important to have thin samples to allow electrons to cross the specimen.

The TEM and HRTEM techniques offer the opportunity to study materials from different points of view. The two most important applications are morphology analysis with the opportunity to reach a level of magnification sufficient to observe atoms or the diffraction patterns of electrons. In the first case, diffraction fringes can be observed and associated with the lattice spacing of the sample by applying simple analysis methods. [122] Similar data can be obtained from the diffraction patterns associated directly with a crystalline structure.

In this work, were assessed the presence of different polymorphic structures with plane spacing analysis and electrons' diffraction patterns.

TEM and HRTEM can be equipped with Energy Dispersive X-Ray Spectroscopy (EDS) to associate crystallographic morphological and elemental analysis on the same sample area.

In this work, TEM micrographs were obtained by Philips CM12 (Philips, Eindhoven, Netherlands) instrument, operating at 120 kV with a LaB6 filament. While the HRTEM images were collected with a JEOL 3010-UHR (300 kV, LaB_6 filament) with a side entry. The samples were deposited on a Cu grid coated with a lacey carbon film. All digital micrographs were acquired by an UltraScan 1000 camera, and the images were processed by Gatan digital micrograph.

3.7 X-ray photoelectron spectroscopy (XPS)

X-ray photoelectron spectroscopy (XPS) is the most used electron spectroscopy for defining the elemental composition and/or speciation of the outer 1–10 nm of any solid substrate both qualitatively and quantitatively. (26)

The basic principle of XPS spectroscopy is detecting and analysing the kinetic energy electron initially bound (core level) to an atom/ion and ejected by an X-rays beam during the analysis. [123]

The kinetic energy of the ejected electrons is correlated to the binding energy (BE) that is element- and environment-specific. Consequently, the emitted electron provides information about the elements to whom the electrons belong before ejection. [123]

The BE of an energy level can be determined from the measured kinetic energy of the photoelectron derived from the particular level following Koopman's theorem, resulting from Hartree-Fock calculation, by the following relation:

$$E_B = hv - E_K - \varphi \qquad \text{Equation (3. 8)}$$

Where E_B is the binding energy, E_K is the kinetic energy, h is the Plank's constant, ν is the frequency of X-ray photon, and φ is the work function of the spectrometer. Both frequency and work function are constant for a given spectrometer. [124]

The surface specificity of information obtained by XPS spectroscopy is due to the limited flight path of electrons before losing a fraction of their kinetic energy. Furthermore, X-ray radiation can penetrate some micrometre below the surface, but the kinetic energy of photoemitted electrons (photoelectrons) is lost by crossing the atomic layers, and the signal will disappear within the spectral background. [125]

XPS spectroscopy can provide elemental identification and quantification of any elements (except for light atoms, i.e., hydrogen and helium) with a sensitivity down to 0.1 atomic %. [123]

In this work, two main applications of XPS analysis were used: i) survey analysis and ii) high-resolution (HR) analysis.

In the former case, survey analysis, samples were studied to investigate the atomic percentage of atoms in the atomic layers of 10 nm below the surface.

When the XPS analysis was performed in HR mode, the investigation of core bands correlated to specific elements was the purpose of the analysis. These bands could shift depending on the chemical state of a surface. The shift is due to an alteration of the electronic charge distribution in the nuclei that affects the core levels of atoms. [124] Furthermore, the fitting of HR curves provides information about the orbitals of the investigated atoms, and consequently, information regarding the coordination of elements can be extrapolated. [124]

Finally, another application of XPS analysis is the determination of the valence band of the material. This application is suitable because the valence band's electrons strongly interact with neighbouring atoms. Their energy distribution, and consequently their kinetic energy, is influenced by each atom's geometrical surroundings; hence, XPS analysis can exploit their analysis. [126]

In this work, X-Ray Photoelectron Spectroscopy (XPS) has been performed on a PHI 5000 VersaProbe (ULVAC-PHI, Physical Electronics Inc., Kanagawa, Japan) instrument, equipped with monochromatic Al Kα radiation (1486.6 eV energy) as X-ray source. Two different pass energy values were used for the survey (187.75 eV) and HR spectra (23.5eV). During the measurements, the charge compensation was obtained with a combination of an electron beam and a low-energy Ar beam system. The HR spectra were curve-fitted using the Casa XPS software (Casa Software Ltd.).

3.8 ζ potential measurement

Zeta potential is an analytical technique that is applied to determine the surface charge of NPs in solution.

Nanoparticle has a net surface charge when dispersed in solution. The surface charge induces the formation of a liquid layer of counter ions firmly bonded to the surface of the nanoparticles (Stern layer). When the nanoparticles diffuse in

solution, they will be involved by a diffuse outer layer that consists of loosely associated ions, as a result, an electrical double layer is created. [127]

The zeta potential is a measure of the difference in potential between the bulk fluid in which a particle is dispersed and the layer of fluid containing the oppositely charged ions correlated with the nanoparticle surface. [128]

During the analysis, a laser is passed through a nanoparticle solution inserted in a specific cuvette under the influence of an electric field.

Charged particles are attracted to the oppositely charged electrode, and their velocity is measured and expressed in unit field strength as their electrophoretic mobility. [129]

Light scattering is one of the most commonly used techniques for determining the electrophoretic mobility of particles. Laser Doppler electrophoresis measures small frequency shifts in the scattered light that arise from particle movement in an applied electric field. The frequency shift can be quantified, and it is summarized by Kaszuba et al. in Equation (3. 9):

$$\Delta f = \frac{(2v\ sin(\frac{\theta}{2}))}{\lambda} \qquad \text{Equation (3. 9)}$$

Where v is the particle velocity, λ is the laser wavelength, and θ is the scattering angle.

The measured electrophoretic mobility (U_E) is converted into zeta potential (ζ) through Henry's equation:

$$U_E = \frac{2\varepsilon\zeta F(\kappa\alpha)}{3\eta} \qquad \text{Equation (3. 10)}$$

Where ε is the dielectric constant of the dispersant, $F(\kappa\alpha)$ is the Henry function, and η is the viscosity. [129]

This equation is also known in a simplified version as the Smoluchowski equation, in which $F(\kappa\alpha)$ equals 1.5. [130] This approximation can be applied when $\kappa\alpha$ is large (approx. 100) and the double layer is thin compared to the particle radius. [129]

This technique is important in this work as titania nanoparticles show surface Ti-OH groups that have an amphoteric behaviour in water, being protonated and deprotonated depending on the pH of the solution. [131] The protonation and deprotonation of surface groups induced a variation of the electrical double layer,

and hence the surface charge of NPs could be measured in correspondence to different pH.

ζ-potential profiles in this work were obtained by evaluating the electrophoretic mobility as a function of pH. Electrophoretic light scattering (ELS) on a Zetasizer Nano-ZS (Malvern Instruments, Worcestershire, UK) was used.

Synthesis and characterization of undoped TiO_2

4 Undoped TiO_2 samples

Undoped TiO_2 photocatalysts were obtained by different sol-gel synthesis methods explained in Chapter 2. The peculiarities of each material were studied by several characterization techniques described in Chapter 3. This Chapter reports experimental results for each material, along with a final paragraph summarizing the most relevant experimental evidence.

4.1 Mesoporous TiO_2 obtained by template-assisted sol-gel synthesis (M-TiO_2)

Here the experimental results obtained during the mesoporous TiO_2 (M-TiO_2) characterization were proposed. The synthesis procedure of the three-block copolymer-assisted synthesis method and the discussion of the characterization results are presented in paragraphs 4.1.1 and 4.1.2.

4.1.1 Synthesis

The TiO_2 NPs (M-TiO_2) were synthesized by a soft template-assisted sol-gel method. The synthesis procedure was as follows: two solutions were prepared; solution A was obtained by dropwise adding 20.0 g $Ti(OBut)_4$ (titanium n-butoxide, 97%) to 120.0 mL acetic acid solution (20%, v/v), while solution B was obtained by mixing 12.0 g Pluronic P123 ((poly (ethylene glycol)-block-poly (propylene glycol)-block-poly (ethylene glycol)) and ~80.0 mL ethanol. Both solutions were kept under vigorous stirring for around 4 h.

Solution B was then added dropwise to solution A: the resulting mixture was sealed, stirred for 24 h at room temperature, and transferred into a Teflon autoclave for hydrothermal treatment at 98 °C for 48 h.

The resulting precipitate was centrifuged and rinsed with water and ethanol, dried at 80 ◦C, and calcined in air at 450 °C for 4 h. [27], [57], [132]

4.1.2 Physico-chemical characterization

The physico-chemical characterization of the synthesized powders includes:

- XRPD analysis.
- Nitrogen adsorption-desorption isotherms at -196°C.
- DR UV-Vis spectroscopy.
- FTIR spectroscopy.
- Transmission electron microscopy.
- XPS analysis.
- ζ-potential curve measurement.

The diffractogram reported in Figure 28 shows several peaks associated exclusively, with different crystallographic planes of anatase at 25.5 (101), 37.4 (004), 47.9 (200), 54.0 (105), 54.9 (211), 62.6 (204), 68.9 (116), and 82.5 (224) 2θ values (PDF-2 card number 01-084-128 the 5, released in 2004). [20]

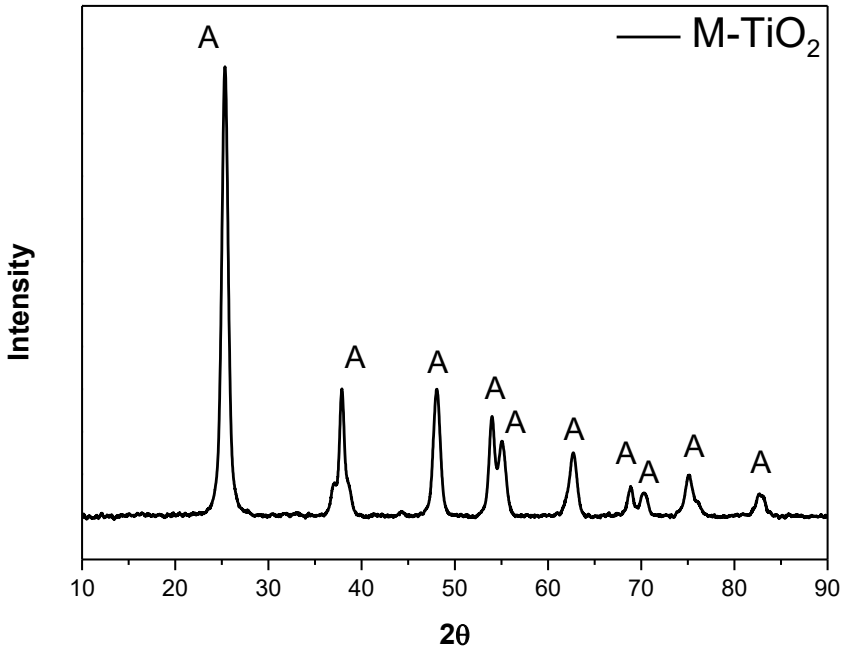

Figure 28. X-ray Powder Diffraction patterns obtained with the M-TiO_2 sample.

The QPA analysis obtained by Rietveld refinement confirmed the presence of anatase as a single polymorphic structure in the M-TiO_2 sample. By applying the

Williamson-Hall method to the diffractogram, an average crystallite size of 10 ± 0.6 nm was obtained.[20]

The isotherm obtained by N_2 adsorption-desorption isotherms at -196 °C is reported in Figure 29. M-TiO_2 sample showed a type IV isotherms with an H2 hysteresis loop typical of ink-bottle mesopores.

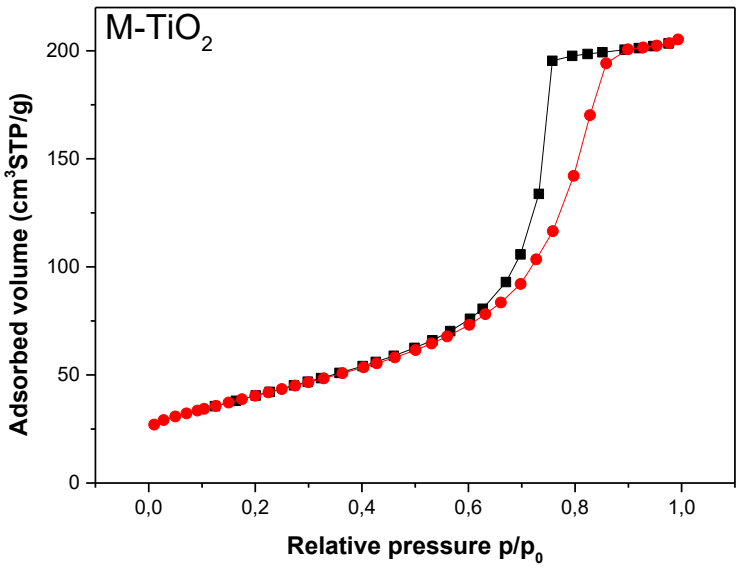

Figure 29. Nitrogen adsorption-desorption isotherm of M-TiO_2.

By applying the BET equation to the linear part of the adsorption isotherm (P/P_0 between 0.2 and 0.5), a specific surface area (SSA) of 150 m^2g^{-1} was obtained. Furthermore, the BJH method was applied to the desorption branch, and the pore size distribution (PSD) was obtained. The PSD showed an asymmetric distribution of mesopores with a maximum at 7.5 nm.[27]

The Kubelka-Munk (K-M) curve obtained with the M-TiO_2 sample is reported in Figure 30. The absorption onset of the K-M curve measured below 400 nm suggests an Eg value that can be reached by UV light. The broad absorption band between 300 and 400 nm was due to the charge transfer (CT) transition from O^{2-} to Ti^{4+} species.[133], [134]

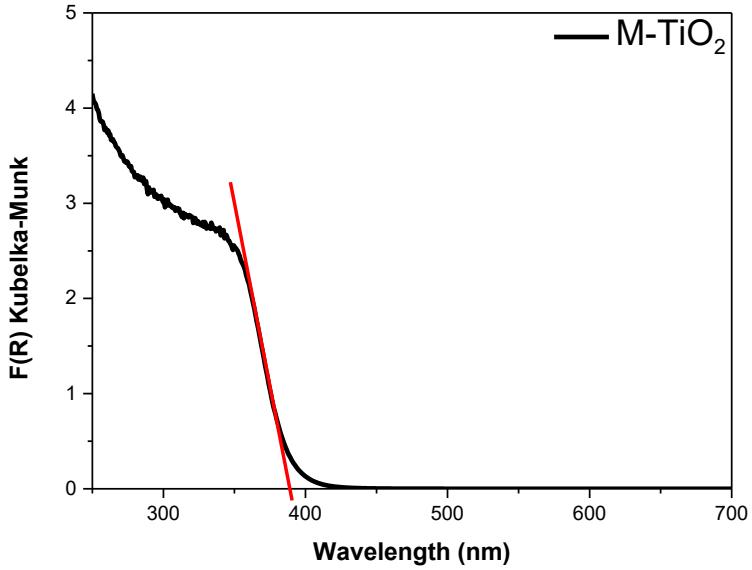

Figure 30. DR-UV-Vis spectrum obtained with the M-TiO_2 sample.

The Tauc's plot (Figure 31) was obtained by applying the proper mathematical function for indirect semiconductors since anatase (indirect semiconductor) is the unique polymorphic structure in the M-TiO_2 sample.

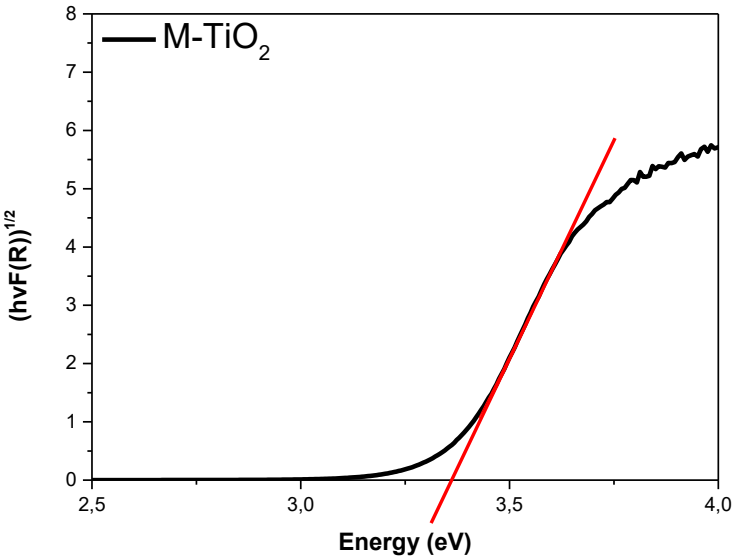

Figure 31. Tauc's plot, as obtained for M-TiO_2 by assuming a behavior of indirect semiconductors.

By fitting the linear part of Tauc's plot Eg value was extrapolated (proposed in Table 4) and it was in the range of UV light, as commonly happens with undoped titania samples. Figure 32 reports the IR spectra of M-TiO_2 after outgassing at room temperature (black curve), at 100°C (blue curve) and 200 °C (red line)

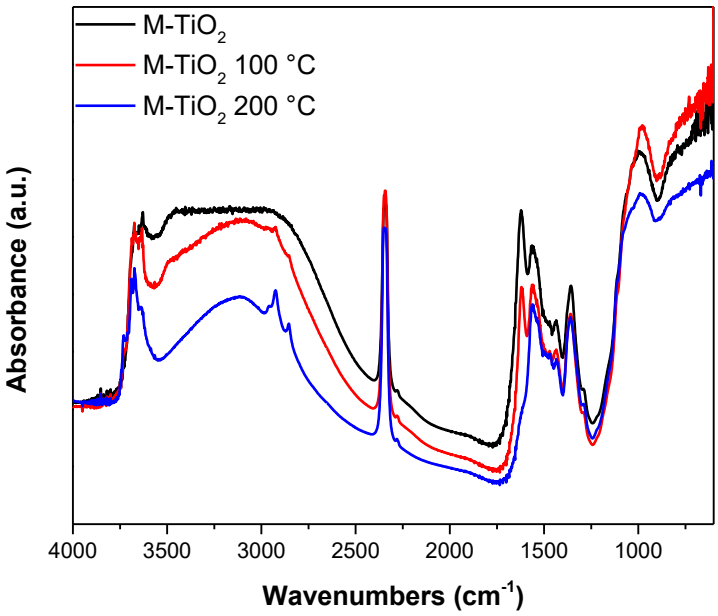

Figure 32. FTIR spectra of M-TiO_2, outgassed at room temperature (black curve), outgassed 100°C (red line), and outgassed 200°C (blue line).

First, a band envelope occurs in the region of carbonates and bicarbonates (1750 -1250 cm^{-1}). These species' formation on the sample's surface was attributed to the reaction of CO_2 interacting with the thermally activated sites at the material surface The available carbon dioxide molecules were due to calcination atmosphere and/or derived from the organic template degradation. The differences among the three spectra in this region were due to the thermal treatment under vacuum condition leading to the degradation of carbonates and bicarbonates or the adsorbed molecular water loss (band at 1620 cm^{-1}).

The band at 2346 cm^{-1} was ascribed to linear CO_2 molecule physisorbed on the material's surface. [135] The CO_2 molecules were probably blocked within some pores, no more accessible after calcination, and were not released even after the thermal treatments. The broad band between 3800 cm^{-1} and 3000 cm^{-1} was assigned to OH stretching. [20] The thermal treatment (blue line) induced a depletion of the wide band due to progressive surface dihydroxylation.

Figure 33 reports the IR spectra (OH stretching range: 3800–3400 cm^{-1}) of the M-TiO_2 sample before and after thermal treatment. The bands at ~3460 cm^{-1} and 3630 cm^{-1} (green asterisks) were assigned to the symmetric and asymmetric OH stretching modes of water molecules strongly adsorbed on Ti^{4+} sites.[136]. Furthermore, the bands evidenced in the spectra at 3672, 3688, and 3735 cm^{-1}(orange asterisks) become more pronounced after the thermal treatment showing a dependence on the treatment conditions, such as temperature, time, and vacuum degree. It is generally accepted that these bands are ascribable to either isolated Ti–OH groups or OH groups bonded to each other by hydrogen bridges or situated in adjacent unit cells. [137] Furthermore, as demonstrated by Gu et al., the bands at 3672 and 3735 cm^{-1} were primarily observed on anatase samples with dominant (101) plane exposition. [137]

In the case of the 3672 and 3688 cm^{-1} bands, the bridging configuration of hydroxyls was proposed $(Ti^{4+})_2$–OH or Ti^{4+}–OH–Ti^{3+}, according to the literature, where surface reactivity of the Ti-OH groups was studied by gas probe analysis. [137]

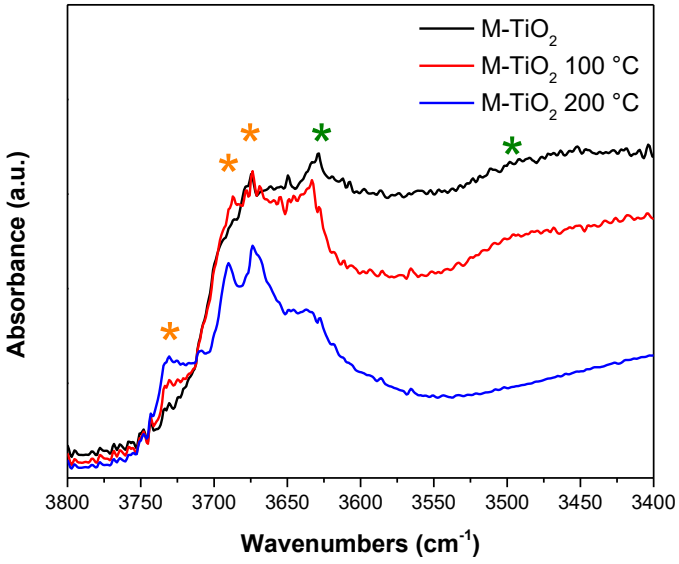

Figure 33. Magnification of the IR spectra of M-TiO_2 sample, outgassed at room temperature (black curve), 100°C (red line) and 200°C (blue line). Evidenced bands at ~3460 cm^{-1} and 3630 cm^{-1} (green asterisks) and 3672, 3688 and 3735 cm^{-1} (orange asterisks).

Overall, according to the surface characterization performed by FTIR spectroscopy, the presence of anatase with a preferential exposition on the surface of 001 crystallographic planes is proposed.

Concerning NPs morphology, Figure 34 reports a selected TEM micrograph of the M-TiO_2 sample showing the homogenous elongated particles shape with some agglomeration.

The TEM image allowed the observation of the intra (orange arrows) and interparticle (blue arrows) mesoporosity, in agreement with nitrogen adsorption/desorption isotherms described in our previous papers. [138][139]

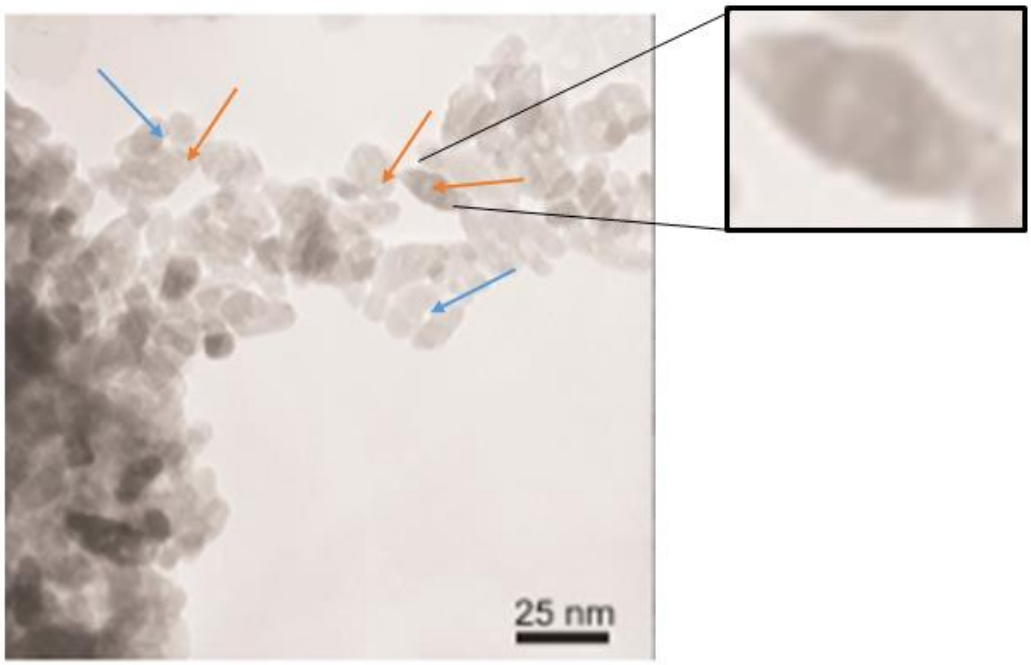

Figure 34. selected TEM micrographs of the M-TiO_2 sample. Evidenced intraparticle's mesoporosity (orange arrows) and interparticle (blue arrows) mesoporosity. In the inset, residual intraparticle porosity was evidenced.

Figure 35 shows the ζ-potential curve obtained with the M-TiO_2 sample by measuring the electrophoretic mobility as a function of pH.

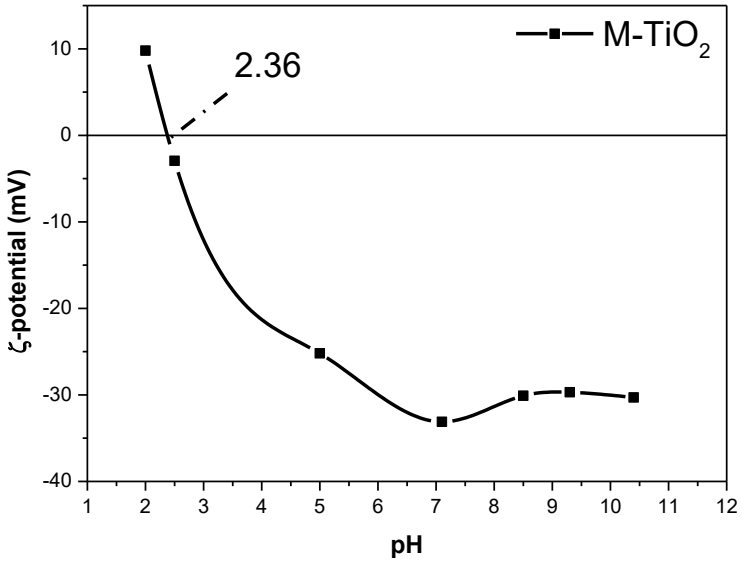

Figure 35. ζ-potential curve obtained with the M-TiO_2 sample by measuring the electrophoretic mobility as a function of pH

A very low point of zero charge was obtained compared to the literature, where the anatase point of zero charge was reported between 5.1 and 5.4 [140]. According to the literature, the factors influencing the pH_{IEP} samples differ, including SSA or particle size, polymorphic structure, and synthesis method.[27] This experimental result can be explained by considering the small NPs size. [27]

4.1.3 Discussion

The adopted synthesis method provided M-TiO_2 samples with a mesoporous structure with intraparticle and residual interparticle mesoporosity, evidenced by TEM micrograph analysis.

The N_2 adsorption isotherm confirmed mesopores' presence of inkbottle geometry with an average diameter of 7.5 nm.

XRPD showed the presence of anatase as a unique polymorphic structure with a crystallites dimension of ~10 nm. The material's electronic properties are typical of an undoped TiO_2 material with no evidence of other bands except for the common band of a titanium dioxide material. In Table 4, data obtained by the characterization technique, applied to the M-TiO_2 sample, were summarized.

Table 4 Some relevant textural and surface properties of the M-TiO_2 sample as obtained by XRPD[a] followed by a Rietveld refinement, [b] N_2 isotherms at −196 ° C, [c] Kubelka-Munk curve [d] and Tauc Plot for indirect semiconductors [e] extrapolations and electrophoretic measurements. The unique polymorphic structure anatase is identified by (A).

Sample	QPA (Phase wt %)[a]	Crystallite size, nm (±)[b]	SSA [m^2/g][c]	Total pore volume [cm^3/g][c]	Eg [eV]	pH_{IEP}[f]
M-TiO_2	100 (A)	10 ± 0.6 (A)	150	0.28	3.28[d] 3.35[e]	2.37

4.2 Nanostructured TiO_2 obtained by reverse micelles-assisted sol-gel synthesis

Here the experimental results obtained during the nanostructured TiO_2 (RM-TiO_2) characterization were proposed. The synthesis procedure of the reverse micelles assisted synthesis method and the discussion of the characterization results were proposed in paragraphs 4.2.1 and 4.2.2.

4.2.1 Synthesis

The nanostructured titania sample (RM-TiO_2) was obtained by the reverse micelles assisted sol-gel synthesis method detailed as follows :34.35 g of di-block copolymer (polyoxyethylene (20) oleyl ether (commercially known as Brij O20) was dissolved in 150 ml cyclohexane (oil) phase by stirring at 50 °C. Then, 4.5 mL bidistilled water was added into the cyclohexane mixture and stirred for 45 min, forming a water-in-oil (w/o) micro emulsion where micelles act as surfactant-encapsulated aqueous nanoreactors. 12.015 mL titanium(IV) butoxide ($Ti(O(CH_2)_3CH_3)_4$, 98%) was then slowly added to the microemulsion, which was isothermally (50 °C) stirred for 2 h. Finally, the microemulsion was broken by adding 150 ml of 2-propanol and sonicated. The resulting solid was rinsed with water and ethanol and separated by centrifugation. Finally, the solid was dried at 100 °C for 12 h and calcined for 2 h in the air at 500 °C with a temperature increase rate of 2.5 °C min^{-1} to burn the surfactant and promote crystallization. [141], [142]

4.2.2 Physico-chemical characterization

The physico-chemical characterization of the sample proposed in the following paragraphs included:

- XRPD analysis.
- N_2 adsorption-desorption isotherms at -196°C analysis.
- DR UV-Vis spectroscopy.
- FE-SEM micrograph analysis.
- XPS analysis.
- ζ-potential curve measurement

Figure 36 reports the XRPD pattern of the undoped titania sample obtained by the reverse micelles-assisted sol-gel method (RM-TiO_2). The diffractogram shows the peaks associated with the three most common polymorphs of TiO_2: anatase, rutile, and brookite. Along with the peaks of anatase (at 25.2 (101), 37.8 (004), 47.9 (200), 53.8 (105), 54.9 (211), 62.6 (204), 68.7 (116) 2θ values), a weak and broad peak due to the (121) brookite diffraction was observed at about 30.7 2θ.[27] The presence of rutile was evidenced by a unique and very weak peak at 27.4 2θ typical of the (110) facet of the rutile phase. [143] The peaks were assigned according to the following cards: JCPDS file: 01-078-2486 for anatase, JCPDS file: 01-083-2242 for rutile, and CPDS file: 96-900-4138 for brookite. [131]

An important evidence was the presence of overlapped and broad peaks at 25.2, 37.8, 47.9, 53.8, 54.9, 62.6, and 68.7 2θ values assigned to anatase and brookite. Peaks overlapping and broadening are typical of materials showing small crystallites (< 120nm) with differently oriented exposed planes.[101][97]

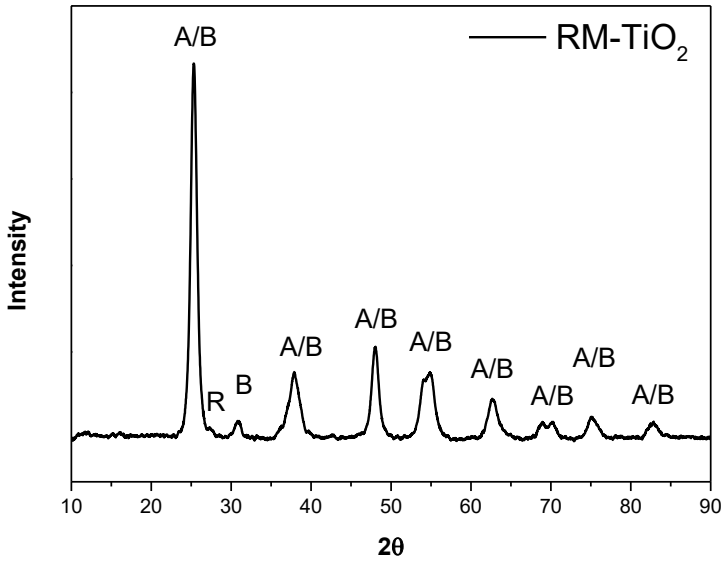

Figure 36. Powder XRD patterns in the 10–90 2θ range of RM-TiO_2 sample. XRD peaks ascribed to anatase rutile and brookite are labeled as A, R, and B, respectively.

By Rietveld refinement, the (QPA) analysis was performed (Table 5), showing 84.3 % anatase, 15.6 % brookite, and 0.1 % rutile. [131] Crystallite size estimation was performed by applying the Williamson-Hall method and showed an average crystallite size (Table 5) of 9.3 nm for anatase, while smaller crystallites of brookite were observed (5.8 nm). The determination of rutile crystallites dimension was impossible due to their negligible amount.

The N_2 adsorption/desorption isotherm measured at −196 °C on the RM-TiO_2 sample is reported in Figure 37. The RM-TiO_2 sample showed a type IV isotherm with an H2-type hysteresis loop. The shape of the isotherm was due to multi-layer adsorption and capillary condensation within the interparticle mesopores. [27]

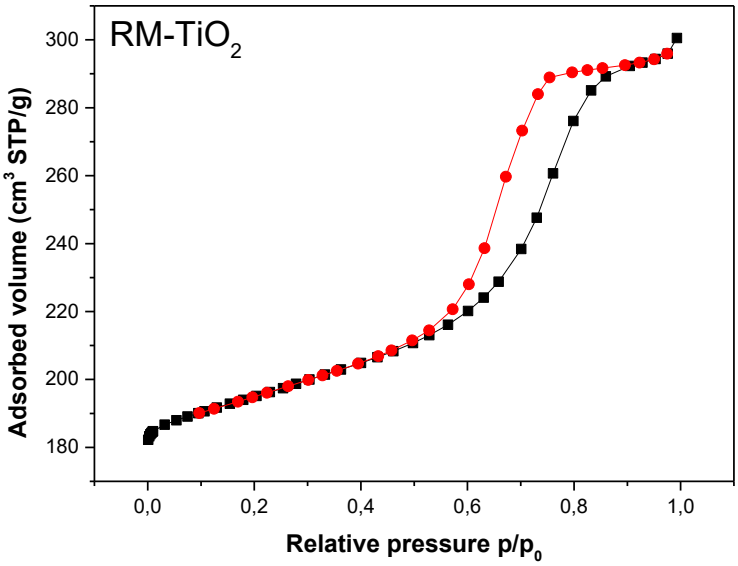

Figure 37. Nitrogen adsorption-desorption isotherm at -196°C obtained with RM-TiO_2 sample.

The formation of interparticle mesopores can be due to the calcination process that led to the formation of porous aggregates/agglomerates while removing the organic template.

Further quantitative information obtained by elaborating the adsorption-desorption isotherm was reported in Table 5, where the average pores diameter was reported. By PSD analysis RM-TiO_2 sample showed a sharp peak centered around 4 nm, including the distribution of small interparticle mesopores. [27]

Figure 38 reports the K-M curve obtained by DR UV-Vis spectroscopy of the undoped RM-TiO_2 sample. The RM-TiO_2 sample showed an onset of absorption at 410 nm. The intense absorption at a wavelength lower than 350 nm was due to the charge transfer transition (CT) from O^{2-} to Ti^{4+} species.[131]

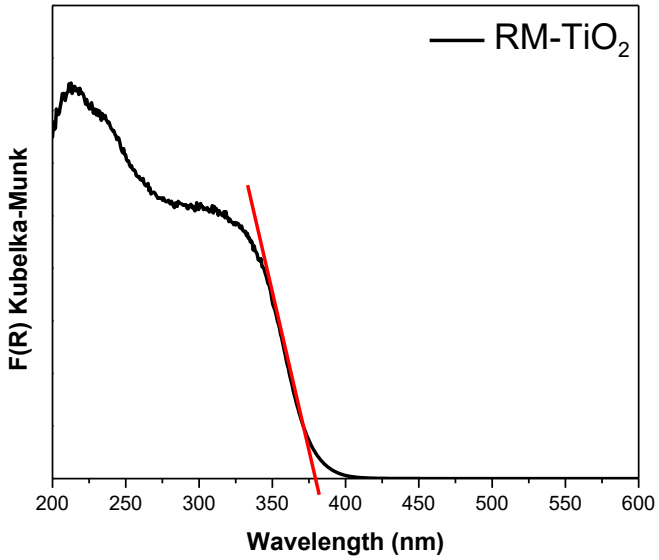

Figure 38. DR-UV-Vis spectrum in the 200–600 nm range of the RM-TiO_2 sample.

Figure 39 shows Tauc's Plot obtained by K-M curve elaboration. Since anatase is the most abundant phase, Tauc's method for an indirect semiconductor was considered.

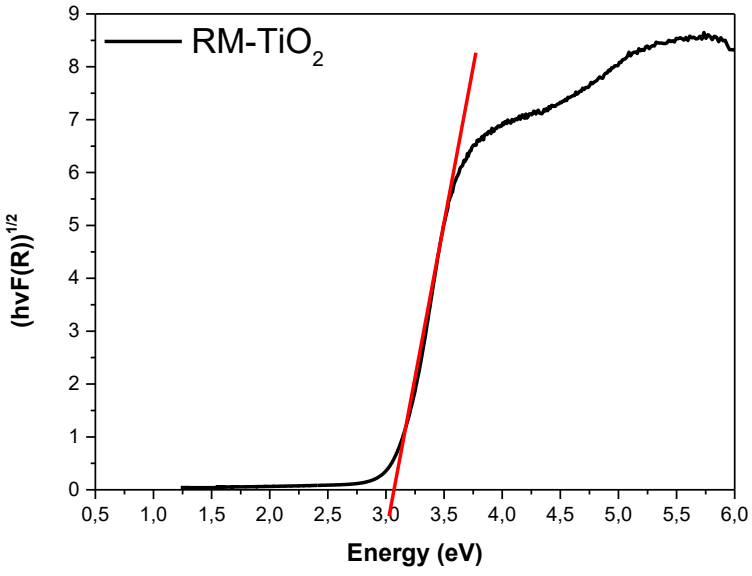

Figure 39. The Tauc's plot was obtained by assuming the indirect semiconductor behavior of the RM-TiO_2 sample.

Table 5 reported the Eg values obtained by linear extrapolation of the onset of absorption from the Kubelka Munk (3.31 eV) curve and the Tauc's plot (3.13 eV). The Tauc's plot obtained assuming a direct band gap (not shown) provided a higher Eg (3.29 eV). The explanation proposed was correlated with the presence of Brookite which is a direct semiconductor with an Eg that spans from 3.1 to 3.4 eV, while anatase is an indirect semiconductor with Eg value of 3.0 eV.[9]

A selected micrograph obtained by FE-SEM analysis of the RM-TiO_2 sample was reported in Figure 40. In the image, small round particles with an average size of 12 nm were observed. [141] The NPs showed a marked aggregation/agglomeration with residual porosity between them.

The dimensions of the NPs can be tuned by controlling the reverse micelles' size. Firstly, the critical micelles concentration (CMC) concentration should be obtained [144] Furthermore, according to the literature reverse micelles' size can be tuned by the variation of the [polar solvent]/ [surfactant] ratio. [93]

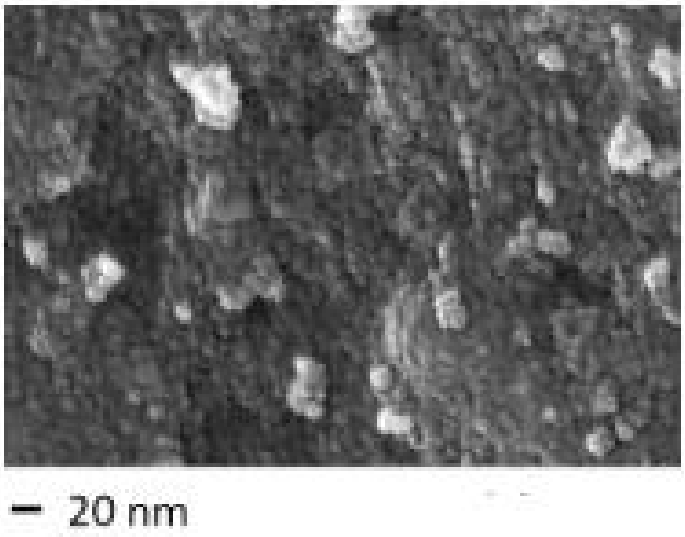

Figure 40, Selected FE-SEM micrograph of the RM-TiO_2 sample.

HR XP analysis of the Ti 2p line reported in Figure 41(left) showed the typical spin-orbit splitting doublet of the Ti $2p_{3/2}$ and Ti $2p_{1/2}$ lines whit a splitting of 5.7 eV, confirming the sole presence of surface Ti^{4+} species. [131] Concerning the O1s line, Figure 41 (right), two components have been observed: the peak at the lower binding energy (BE) is assigned in literature to lattice oxygen (O^{2-}) species. In contrast, the line at higher BE can be associated with surface adsorbed water/OH groups. [27]

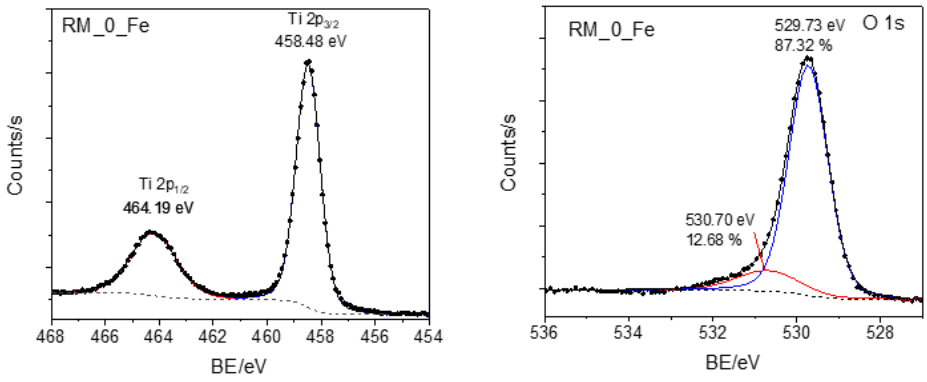

Figure 41. HR XP spectroscopy results obtained by RM-TiO_2 sample analysis. Ti 2p line (left) and O 1s line (right).

Figure 42 shows the ζ-potential curve of the RM-TiO_2 sample. The obtained pH_{IEP} was 3.5, higher than the value obtained with the M-TiO_2 sample (2.37). The difference between the two samples can be due to the presence of rutile on the surface of the RM-TiO_2 nanoparticles, which in literature is reported as the polymorphic structure with higher pH_{IEP} among the three main polymorphic structures. [140]

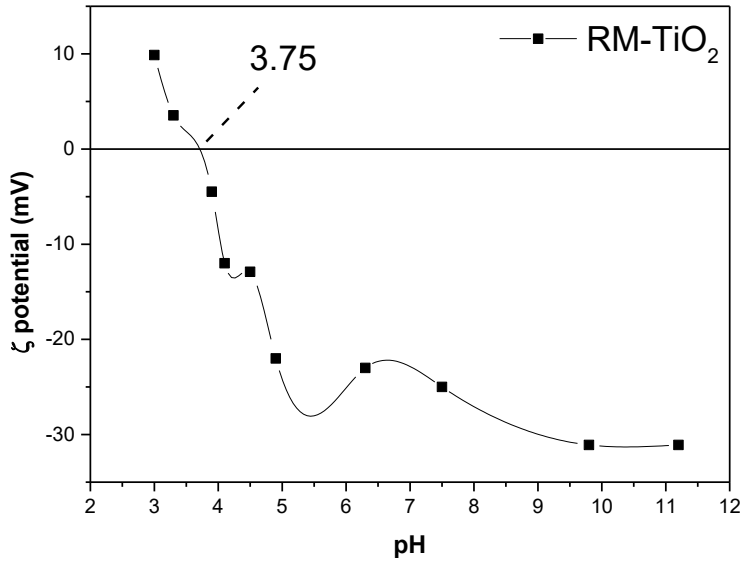

Figure 42. ζ-potential curves obtained by measuring the electrophoretic mobility as a function of pH obtained with RM-TiO_2 sample.

4.2.3 Discussion

The reverse micelles-assisted sol-gel method allowed for obtaining undoped mesoporous titania (RM-TiO_2). The RM-TiO_2 sample showed a mixed polymorphic structure with anatase and brookite prominent presence. Furthermore, the synthesis method induced the formation of round nanoparticles that agglomerate/aggregate during the calcination process with the formation of interparticle mesoporosity. The specific surface area was lower than M-TiO_2, but the average size of pores was smaller.[27] HR XPS analysis confirmed the presence of sole Ti^{4+} species on the surface of the material. The surface charge of the material was investigated by ζ-potential curve analysis, and the particles showed a pH_{IEP} of 3.50.Table 5 reports the data obtained from the characterization techniques used to study the RM-TiO_2 sample.

Table 5. Some relevant textural and surface properties of the M-TiO_2 sample as obtained by XRPD[a] followed by a Rietveld refinement, [b] N_2 isotherms at −196 ° C, [c] Kubelka-Munk curve [d] and Tauc Plot for indirect semiconductor [e] extrapolations and electrophoretic measurements [f]. The polymorphic structures anatase is identified by (A), rutile is identified by (R) while (B) stands for brookite polymorphic structure.

f

Sample	QPA (Phase wt%)[a]	Crystallites size, nm (±)[b]	SSA [m^2/g][c]	Total pore volume [cm^3/g][c]	Eg [eV]	pH_{IEP}[f]
RM-TiO_2	84.3 (A) 15.6 (B) 0.1 (R)	7.4 (0.2) (A) 7.2(0.3) (B) N/A	105.7	0.203	3.31[d] 3.16[e]	3.50

4.3 Mesoporous TiO_2 obtained by a template-free sol-gel synthesis at pH 2 (AB and ABR)

Here the experimental results obtained during the nanostructured TiO_2 (RM-TiO_2) characterization were proposed. The synthesis procedure of the material obtained by template free sol-gel synthesis method and the discussion of the characterization results were proposed in paragraphs 4.3.1 and 4.3.2.

4.3.1 Synthesis

The AB and ABR samples were obtained by a template-free sol-gel method under pH control to tune the brookite formation. In a typical preparation, a solution was prepared from 30.0 mL $Ti(OPr)_4$ (titanium(IV) isopropoxide) and 30.0 mL isopropyl alcohol. The obtained solution was stirred for 20 min, and bi-distilled water (300 mL) was added during stirring. The obtained mixture was heated in a Teflon autoclave for 5 h at 80 °C inside a stove and then cooled to room temperature. After cooling, the pH of the solution was varied by dropwise adding 1.0 M HNO_3 solution to obtain a pH equal to 2.0 for both samples (AB and ABR). The sol was stirred at r.t. for 20 h to obtain a gel, which was repeatedly washed with bi-distilled water and isopropanol, centrifuged dried at 100°C for 12 h in a drying oven. The resulting product was divided into two aliquots that were calcined in a muffle furnace. The calcination temperatures were 200 °C for the AB sample and 600 °C for the ABR sample. The same calcination time of 2 h was adopted for both samples. Finally, both powders were rinsed four times using an ethanol/water mixture and centrifuged.[145] The final cleaning process was adopted to prevent the leaching of residual organic components.

Regarding the AB sample, four batches were synthesized, showing a deep similarity in the XRPD analysis results. For this reason, only data regarding the Batch 1 sample were presented in these paragraphs.

4.3.2 Physico-chemical characterization

The physico-chemical characterization of the sample proposed in the n following paragraphs included:

- XRPD analysis.
- N_2 adsorption-desorption isotherms at -196°C analysis.
- DR UV-Vis spectroscopy.
- FTIR spectroscopy.

- HRTEM micrographs and electron diffraction patterns.
- XPS analysis.
- ζ-potential curve measurement.

Figure 43 shows the XRP diffractograms obtained by the AB and ABR samples analysis. Both samples showed mixed phase compositions. The AB sample showed anatase and brookite diffraction peaks. The peaks were assigned to both polymorphic structures at 25.2, 37.8, 47.9, 53.8, 54.9, 62.6, and 68.7 2θ values. The typical peaks of the two polymorphic structures were overlapped and the broad shape suggested the presence of small crystallites. The presence of brookite was confirmed by the presence of the peak at 30.7 2θ assigned in the literature to (121) brookite crystallographic plane. [27]

The ABR sample diffractogram showed the same peaks assigned to anatase and brookite, but a peak at 27.4 2θ typical of the (110) facet of rutile was noticed. [143] Furthermore, the peak shape evidenced in the ABR diffractogram suggested the presence of larger crystallites when compared to the AB sample. [27]

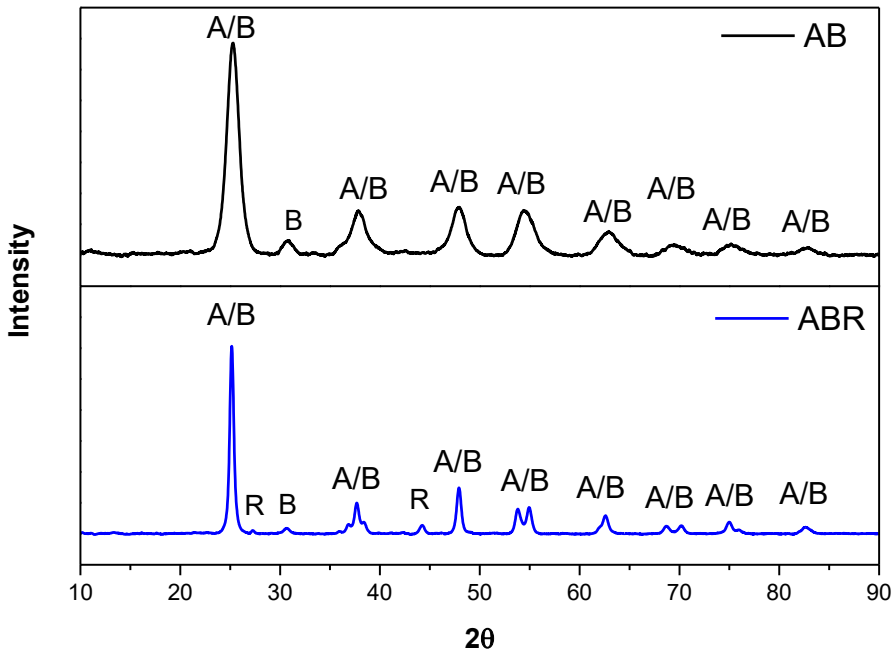

Figure 43. Powder XRD patterns in the 10–100 2θ range of AB (black line) and ABR (blue line) sample. XRD peaks ascribed to anatase rutile and brookite are labeled as A, R, and B, respectively

The QPA obtained by Rietveld refinement (Table 6) summarized the evidence of a decrease in brookite content in the ABR sample together while some rutile formation. This result agreed with the literature where brookite may favor the transition to rutile in mixed anatase/ brookite NPs synthesized in an acid medium. [146] The crystallites average dimension analysis performed by the W-H method (Table 6) provided evidence of increased crystallite size for every polymorphic structure in the case of the ABR sample. Furthermore, according to W-H data, the rutile crystallites showed an average dimension of 39 nm. This dimension is above 35 nm, which is reported in the literature as the lower limit of stability of rutile nanocrystals. [15]

Figure 44 reports the N_2 adsorption-desorption isotherm of AB and ABR samples. Both isotherms were classified as type IV isotherms with H2 hysteresis loop type. [27] This hysteresis geometry is typical of ink bottle mesoporosity. The shape of the loop is associated in the literature with a narrow distribution of pore bodies with a wide neck size distribution.[105] The differences in the isotherms between AB and ABR could be associated with some differences in these distributions, but both samples showed ink bottle mesopores.

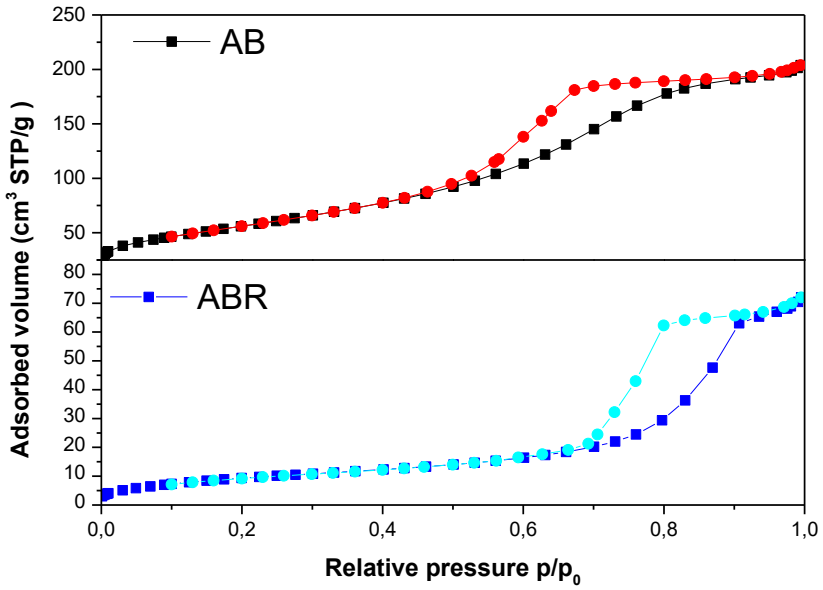

Figure 44. Nitrogen adsorption-desorption isotherms at -196°C obtained with AB and ABR samples.

The PSD of the AB and ABR samples (Figure 45) were evaluated by the BJH method and confirmed differences in their pore size distribution. The PSD of AB

sample was applied to adsorption branch because the hysteresis loop of this material closed near 0.42 P/Po that is the cavitation limit for liquid nitrogen. On the other hand, the BJH method was applied to the desorption branch of ABR isotherms. The AB sample showed a PSD cantered around 5 nm, while the ABR sample showed a decreased porosity where only a few larger mesopores were observed (Figure 45). [27]

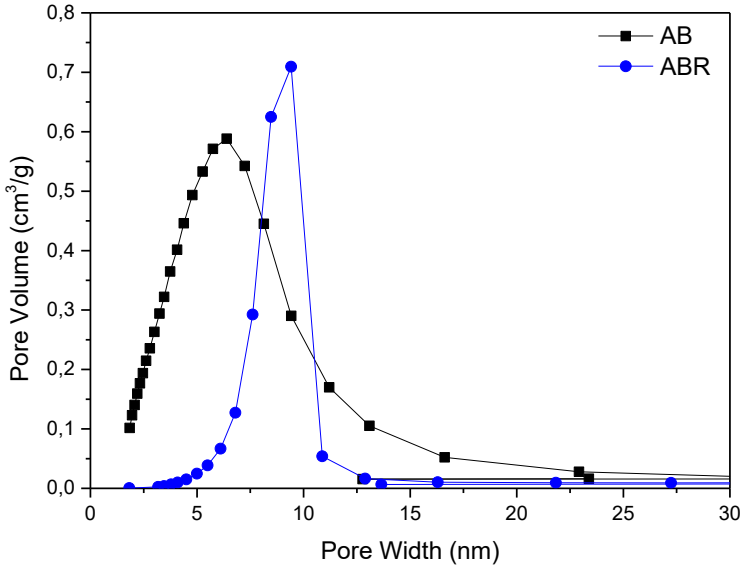

Figure 45 Pore size distribution as obtained by BJH method application on adsorption branch for AB sample (black line) and desorption branch for ABR sample (blue curve)

SSA (Table 6) obtained by BET equation application showed a decrease ranging from 210 m^2g^{-1} for AB to 31 m^2g^{-1} for the ABR sample. The calcination temperature, hence, affected the surface of the materials.[27]

Figure 46 shows the Kubelka-Munk curve obtained by DR UV-Vis analysis of AB and ABR samples. The onset of the Kubelka-Munk curves was different, showing different light absorption edges. The ABR sample's Kubelka Munk curve was shifted at a higher wavelength than AB's K-M curve. This difference can be due to a rutile phase presence in the ABR sample as in the literature, rutile is known as the polymorphic structure with smaller Eg among anatase, rutile, and brookite.[9]

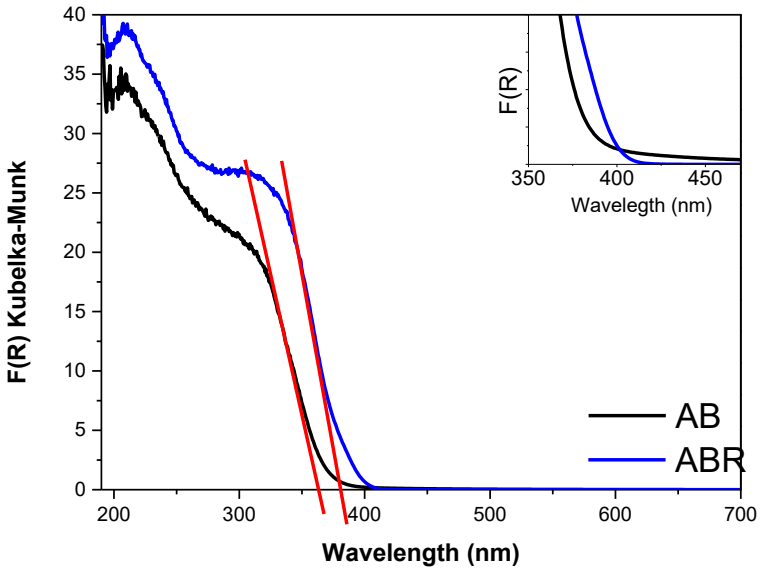

Figure 46. DR-UV-Vis spectrum in the 200–700 nm range of AB (black curve) and ABR (blue curve).

Figure 47 reports the extrapolated Tauc's plot, obtained considering an indirect semiconductor due to the majority presence of anatase in both samples. The main evidence of these curves was the occurrence of a pronounced Urbach tail in the AB sample curves (inset Figure 46 and green arrow Figure 47). This tail is an exponential part of the energy spectrum due to different sources of lattice disorder in the crystals, like amorphous phase, doping, or mixed phase presence.[147]-[148]

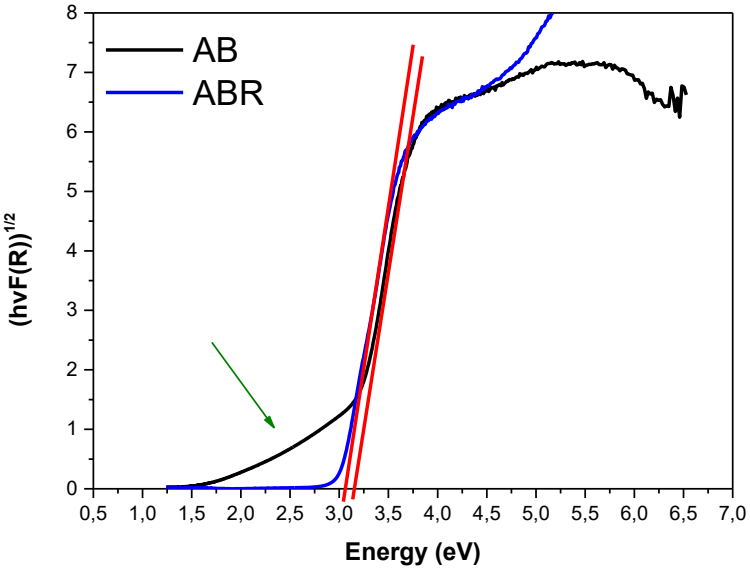

Figure 47. The Tauc's plots were obtained by assuming the indirect semiconductor behavior of the AB sample (black curve) and ABR sample (blue curve), green arrow indicating the Urbach Tail.

The extrapolation of the band gap considered the presence of the Urbach tail that significantly reduced the band gap to a value of ca. 2.2 eV for the AB sample. This value of Eg could enhance visible light adsorption and improve photocatalytic properties. On the other hand, the ABR sample showed the presence of rutile, a direct semiconductor with smaller Eg compared to other polymorphic structures. [9] The advantage of a direct band gap, in case of allowed direct transition, is the possibility of having e-/h+ separation without involving phonons to guarantee the transition. Consequently, electrons can be excited from VB to CB directly. [17]

Figure 48 shows FTIR spectra of AB and ABR samples after a prolonged outgassing process at room temperature. Both studied samples showed the presence of molecular water and, consequently, H-bonding.

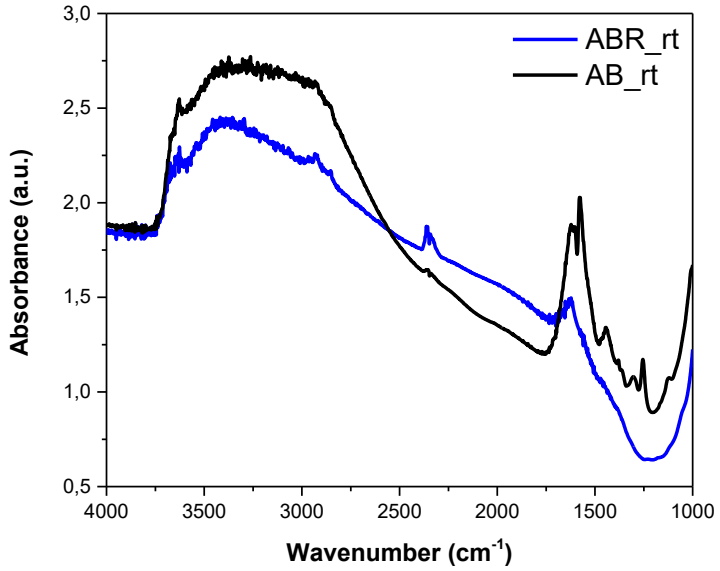

Figure 48. FTIR spectra of AB and ABR samples outgassed at room temperature.

Atmospheric water adsorbed on the surface is evident in the 3800 – 3000 cm^{-1} range, where different OH species can be observed. The broad and intense absorption band due to the H-bonding between water molecules is the first difference between the two spectra; this signal is particularly intense with the AB sample, having a larger SSA and lower calcination temperature.

The second region showing differences was the carbonate-like region characterized by bands in 1750 – 1200 cm^{-1}. (Figure 49) The bands observed by IR spectroscopy of the AB sample (green asterisk) were:

- The band at 1370 cm^{-1} assigned to bidentate carbonate[149]
- The bands at 1580 and 1445 cm^{-1} assigned to bicarbonates[150]

The most interesting band observed at c.a. 1250 cm^{-1} (red asterisk)(Figure 49)was assigned to CO_2^- radical ions, which are highly reactive intermediates of CO_2 reduction forming during the calcination process. According to the literature, the formation of this species is associated with CO_2 molecules adsorption on Ti^{3+} sites. [151]

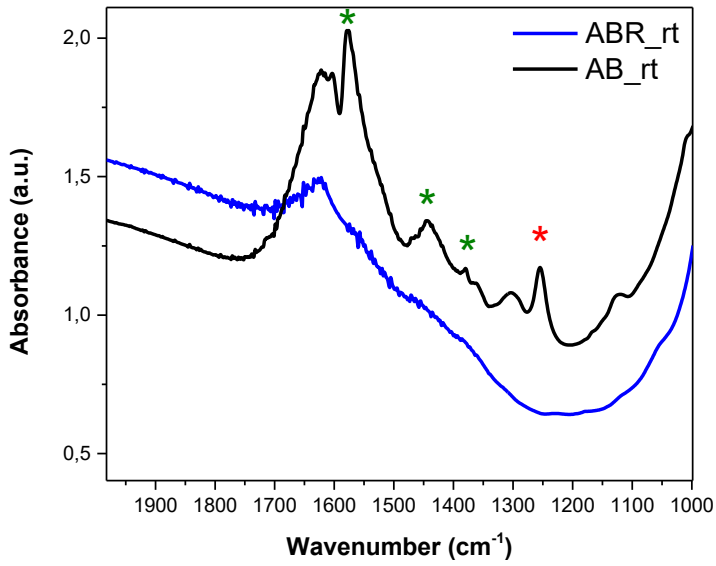

Figure 49. FTIR spectra of AB and ABR samples in the range 2000 to 1000 cm^{-1}.

The presence of CO_2^- radical ions is the main result of this analysis. The effects of the existence of these species on the surface can explain some features of the AB sample, including the Urbach tail.

Furthermore, a calcination test was performed in a controlled environment to confirm the band's formation at c.a 1250 cm^{-1} during the calcination process. The thermal treatment was performed under air atmosphere at 200°C for 2h as requested by the synthesis method, to avoid phase transitions. The pellet obtained from the AB sample was analyzed by FTIR spectroscopy before and after the calcination (Figure 50).

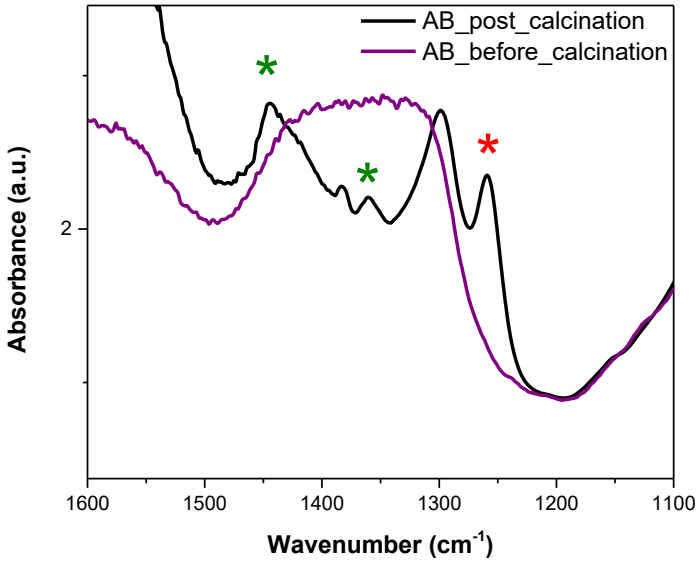

Figure 50. IR spectra obtained before (violet line) and after (black line) thermal treatment performed in air at 200°C for 2h on pellet obtained from undoped AB sample.

The investigated band at 1250 cm^{-1} appeared after thermal treatment at 200°C (red asterisk). The controlled calcination process showed the peculiarity of this band which was not evidenced with any bands before calcination (violet curve)

Further investigation of CO_2^- radical ions on the surface of the AB sample showed that by exposure of the material to a vacuum atmosphere, these species were desorbed around 200°C. After desorption, no further formation was observed by consequent controlled treatment in CO_2-rich atmospheres. This evidence showed that the formation of CO_2^- radical ions on the surface of the sample was a thermally activated process, taking place as a consequence of the specific condition of calcination, including the available residual organic compounds.

Notably, Figure 50 also shows the appearance of other carbonates-related bands after the calcination process at 200 °C. These species were probably formed by the interaction with atmospheric CO_2 or carbon dioxide originated by organic molecules (i.e., isopropyl alcohol) degradation. Some broad bands were evidenced before calcination, testifying to organic compounds on the surface.

The aforementioned results were typical of the AB sample. The ABR sample analyzed by IR spectroscopy did not show any of these carbon-related species bands, probably because of the higher calcination temperature (600 °C). Another

possible explanation was the differences within polymorphic structures on the sample's surface.

Figure 51 reports the HRTEM images obtained with AB and ABR samples to investigate the heterojunction between polymorphs' presence and distribution. In Figure 51, the fringe of diffractions offered the opportunity to distinguish between anatase and brookite phases. The presence of anatase/brookite heterojunctions is highlighted by dashed red circles in the case of the AB sample and green circles with the ABR sample. For clarity, in the right column of Figure 51, the Fast Fourier Transform (FFT) images correlated with morphological images were reported.

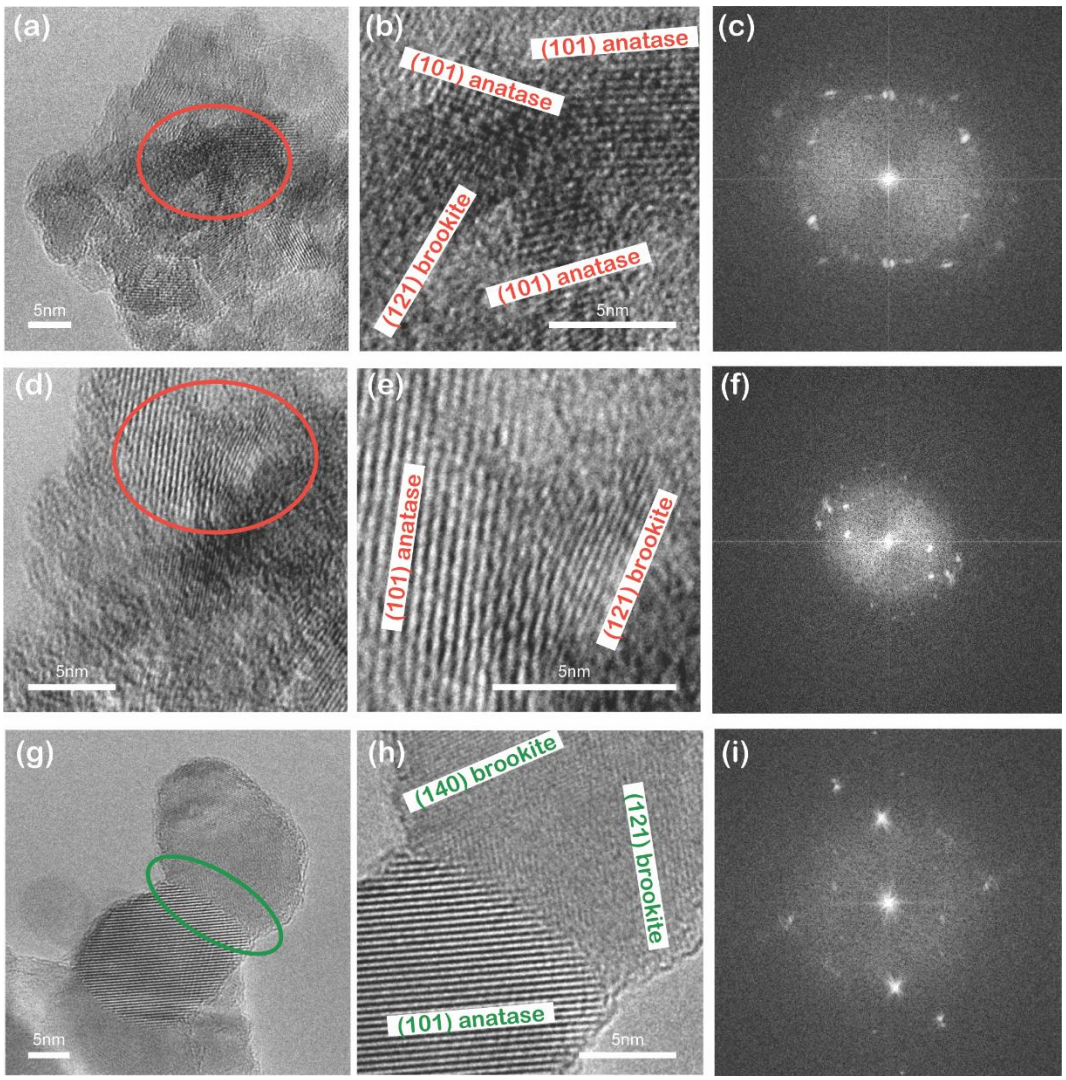

Figure 51. Representative HRTEM images of AB (a,b,d,e) and ABR (g,h) samples and relative electron diffraction patterns.

The amount of anatase-brookite heterojunctions were estimated: these defective areas cover about 32% of the total acquired HRTEM images. It is also important to highlight the evidence that anatase/brookite heterojunctions were also detected on the ABR sample. In the ABR sample, larger crystals facilitated the observations of these defective areas, but anatase/brookite heterojunctions covered just around 19 % of the acquired images.

The presence of heterojunctions was demonstrated in the literature, improving the photocatalytic performance of TiO_2 material. [24] Furthermore, the heterojunctions area, which is a highly reactive area, could act as a substrate for CO_2^- radical ions formation on the surface of the AB sample. This hypothesis could explain the absence of these species in the ABR sample, distinguished by the lower amount of heterojunction and larger highly crystalline domains.

Figure 52 shows the curves obtained by the ζ-potential curve measurement of AB and ABR.

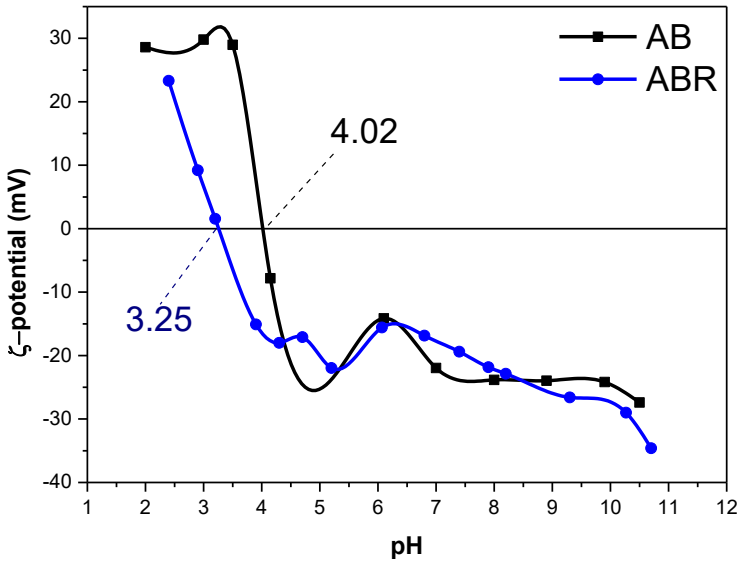

Figure 52. ζ-potential curves obtained by measuring the electrophoretic mobility as a function of pH obtained with AB (black line) and ABR (blue line) samples.

ζ-potential curves obtained for AB and ABR samples showed two different pH_{IEP} values. The higher pH_{IEP} obtained with the AB sample was ascribable to NPs size and phase composition. According to the literature NPs with a diameter below 10 nm have higher pH_{IEP} compared to larger NPs. [152] Furthermore, anatase was observed by other authors as the polymorphic structure with the highest pH_{IEP},

while rutile and brookite showed more basic pH_{IEP} values. [140] Overall, the ABR pH_{IEP} value could be due to larger NPs and a brookite-rich surface.

4.3.3 Discussion

The two samples were synthesized through a template-free sol-gel synthesis method based on a pH control to obtain a mixed polymorphic structure.

The differences between the two samples can be attributed to the calcination temperature, the only parameter that varied during the synthesis (200°C for the AB sample and 600°C for the ABR sample).

The SSA and the total pore volume were affected by calcination temperature, with a decrease of both values for the ABR sample due to agglomeration and growth of the crystallite size at high temperatures.

Furthermore, a variation of the polymorphic structure occurred with a decrease of brookite content in the ABR sample compared to AB, while the increase of rutile was observed. This difference in the polymorphic structure induced a change in the electronic properties of the samples, this aspect was confirmed by literature, where the rutile phase has a lower Eg among the three polymorphs.

Another important peculiarity in the electronic properties analysis was the Urbach tail's presence in the AB sample. This experimental evidence induced further investigation about the effective Eg of this sample.

By extrapolating the value of Eg from the Tauc's plot, considering the Urbach's tail, a value of 2.2 eV for the AB sample was assessed. [147] According to this Eg value AB sample can be considered as a photocatalyst able to exploit visible light in the light-green region of the spectrum. This Eg reduction compared to the ABR sample can be ascribed to midgap-states' presence.

FTIR spectroscopy experiments explained the presence of these midgap levels where a peculiar band in the AB sample was observed. The band was located at c.a. 1250 cm^{-1} and was assigned to CO_2^- radical ions. These species formed during the calcination process and released after thermal treatment at 200 °C under vacuum conditions can be obtained by interacting CO_2 molecules with Ti^{3+} ions. [151]

CO_2^- radical ions species interacting with titania nanoparticles can enhance the photocatalytic properties of the material by:

- acting as an electron-withdrawing agent promoting electron-hole separation. [153]
- Enhancing the oxidative ability of photo-generated holes. [153]

- Acting as a photosensitizer agent to promote visible-light photocatalytic activity of TiO_2. [153]

The peculiarity of these species on the surface of the AB sample could be due to the presence of well-evidenced (by HRTEM analysis) heterojunctions between anatase and brookite, offering defective areas on the surface. On the other hand, the ABR sample showed less extended heterojunction areas and, together with the higher calcination temperature, could be considered as the reasons for the absence of CO_2^- radical ions species.

Table 6 summarizes the physicochemical characterization data obtained by AB and ABR sample analysis.[27]

Table 6. Some relevant textural and surface properties of the AB and ABR samples, as obtained by XRPD[a], followed by Rietveld refinement, [b] N_2 isotherms at −196 ° C, [c] Kubelka-Munk curve [d] and Tauc Plot for indirect semiconductors extrapolations, and electrophoretic measurements [f]. The polymorphic structures anatase is identified by (A), rutile is identified by (R) while (B) stands for brookite polymorphic structure.

Sample	**QPA (Phase wt%)[a]**	**Crystallites size, nm (±)[b]**	**SSA [m^2/g][c]**	**Total pore volume [cm^3/g][c]**	**Eg [eV]**	**pH_{IEP}[f]**
AB	78 (A) 22 (B)	5.5 (0.6) (A) 3.8 (0.4) (B)	210	0.31	3.37[d] 3.20[e]	4.02
ABR	88 (A) 9.3 (B) 9.1 (R)	39.0 (5.5)(A) 16.8 (3.6)(B) 52.1 (8.1)(R)	31	0.09	3.22[d] 3.02[e]	3.25

5 Synthesis and characterization of Fe-doped TiO_2 samples

By modifying the synthesis procedures adopted to obtain the undoped M-TiO_2, RM-TiO_2, and AB samples, Fe-doped TiO_2 photocatalysts were obtained. Doping with Fe is one of the most common choices, as this metal is non-toxic, abundant in the earth and capable of red-shift TiO_2 absorption. [131]The literature reports different conventional synthesis methods proposed in the literature for Fe-doped TiO_2. [154]–[157] The sol-gel synthesis methods adopted in this work offer valuable strategies by combining the pros of sol-gel methods (low synthesis temperature, control over microstructure, and its ability to tune the particle size, distribution, and morphology through the reaction parameters) with the benefits of Fe-Doping. The nominal iron content introduced varied among samples, and different sets of samples were obtained. This chapter reports experimental results for each set of Fe-doped TiO_2 photocatalysts, along with a final paragraph summarizing the most relevant experimental evidence.

5.1 Iron-doped Mesoporous TiO_2 obtained by three-block copolymer assisted sol-gel synthesis

The analysis of the effects of iron doping on mesoporous titania obtained with a triblock copolymer-aided sol-gel synthesis is reported below. Different amounts of iron precursor were introduced during the synthesis to estimate the differences among samples.

The sample characterizations are reported in the following paragraph. The samples were named depending on the nominal weight percentage of iron with the general name M-TiO_2_X_Fe where X is the weight percentage of iron added during the synthesis.

5.1.1 Synthesis

The Fe-doped TiO_2 NPs with nominal iron contents of 1, 2.5, and 3.5 wt. % were prepared by following a soft template-assisted sol-gel method. The synthesis procedure was as follows: two solutions were prepared. Solution A was obtained by dropwise adding 20.0 g $Ti(OBut)_4$ (titanium n-butoxide, 97%) to 120.0 mL acetic

acid solution (20%, v/v). Solution B was obtained by mixing 12.0 g Pluronic P123 ((poly (ethylene glycol)-block-poly (propylene glycol)-block-poly (ethylene glycol)) and ~80.0 mL ethanol and both solutions were kept under vigorous stirring for approximately 4 h. To solution A, after the dispersion of titanium butoxide, 0.254, 0.568, and 0.777 g of iron(III) chloride hexahydrate, $FeCl_3 \cdot 6H_2O$ were added to obtain the M-TiO_2_1_Fe; M-TiO_2_2.5_Fe; M-TiO_2_3.5_Fe samples respectively (Figure 53).

Solution B was then added dropwise to solution A: the resulting mixture was sealed, stirred for 24 h at room temperature, and transferred into a Teflon autoclave for hydrothermal treatment at 98 ◦C for 48 h.

The resulting precipitate was centrifuged and rinsed with water and ethanol, dried at 80 ◦C, and calcined in air at 450 °C for 4 h. [20], [27], [57], [132]

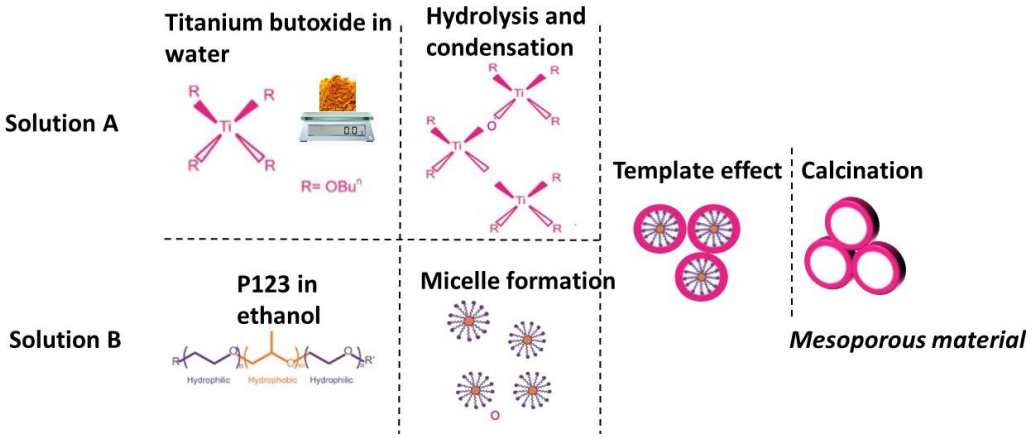

Figure 53 Simplified scheme of the steps leading to the production of TiO_2 NPs using three-block copolymer assisted sol-gel synthesis method. (adapted from [83])

5.1.2 Characterization

The physico-chemical characterization of the sample proposed in the following paragraphs included:

- XRPD analysis.
- N_2 adsorption-desorption isotherms at -196°C analysis.
- D-R UV-Vis spectroscopy.
- FTIR spectroscopy.
- TEM micrographs.
- XPS analysis.
- ζ-potential curve measurement.

Figure 54 reports the diffractograms obtained by the analysis of the whole set of samples of mesoporous iron-doped titania samples. The peaks at 25.5 (101), 37.4 (004), 47.9 (200), 54.0 (105), 54.9 (211), 62.6 (204), 68.9 (116), and 82.5 (224) 2θ values were associated to anatase. The presence of Fe did not bring any significant shift of the anatase peaks observed with the undoped TiO_2 sample (Figure 28) (PDF-2 card number 01-084-1285, released in 2004). [20] Furthermore, no peaks correlated to other polymorphic structures or assigned with iron species were observed. [20]

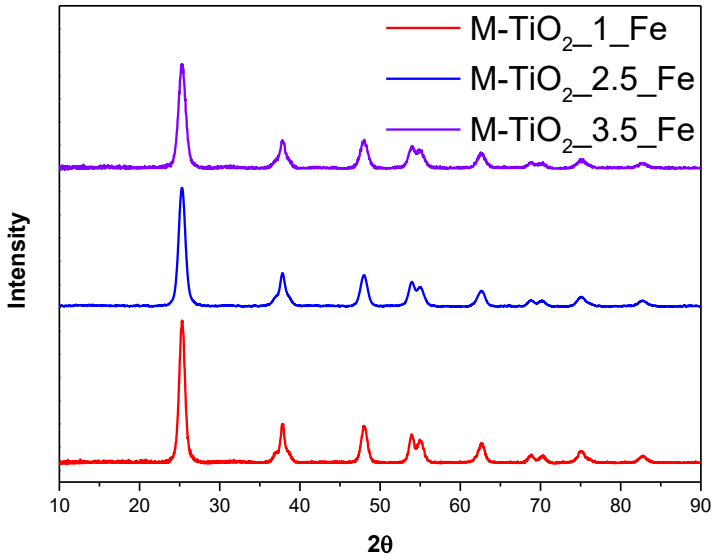

Figure 54. X-ray Powder Diffraction patterns obtained with M-TiO_2_3.5_Fe (red), M-TiO_2_2.5_Fe (blue), and M-TiO_2_1_Fe (violet). All the peaks correspond to anatase. [20]

Concerning crystallite dimension analysis, Fe doping induced a variation of the crystallite size, as obtained by applying the Williamson–Hall method. The corresponding values are reported in Table 7 [20]. As a whole, Fe doping led to an overall decrease in the crystallite size showing an influence of iron atoms on the bulk of the material. This evidence was probably due to Fe^{3+} presence during the synthesis retarding the growth of anatase nanocrystals as already demonstrated in the literature. [158] On the other hand, by Rietveld refinement, the anatase cell volume variation with respect to nominal wt. % Fe was observed and reported in Figure 55.

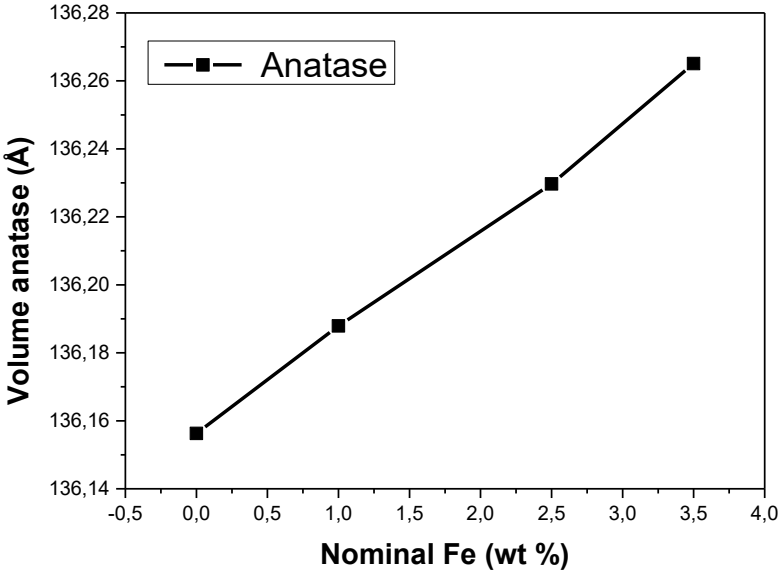

Figure 55. Trend of the cell volumes of anatase versus the nominal Fe content (wt.%).

The trend observed was a correlation between the nominal iron amount and anatase cell volume. The elementary cell volume increased by introducing iron. The possible explanation is the isomorphic substitution of Fe^{3+} in the Ti^{4+} sites of the lattice. [31][131] The proposed explanation for the cell volume growth was the difference in ionic radius of the two involved cations showing 0.75 and 0.79 Å, respectively. [35]Interestingly the crystallite size and the cell volume showed an opposite trend with iron introduction.

Table 7 Crystallites dimension as obtained by applying the Williamson–Hall method of iron-doped M-TiO_2 samples and undoped M-TiO_2 presented as a benchmark.

Sample	**Crystallites size [nm]**
M-TiO_2	12.4 ± 1.3 (A)
M-TiO_2_1_Fe	9.4 ± 0.4 (A)
M-TiO_2_2.5_Fe	8.4 ± 0.6 (A)
M-TiO_2_3.5_Fe	7.1 ± 0.6 (A)

Figure 56 reports the N_2 adsorption-desorption isotherms of the studied samples. All the samples showed a type IV isotherm ascribed to the occurrence of multi-layer adsorption and capillary condensation within both intra- and inter-particle mesopores. The shape of the hysteresis loop indicated the presence of slit pores. On the other hand, N_2 adsorption-desorption isotherms of the M-TiO_2 sample (Figure 29) showed an H2 hysteresis loop typical of inkbottle mesopores. The difference was associated with Fe doping inducing surface disorder in the system. [20]

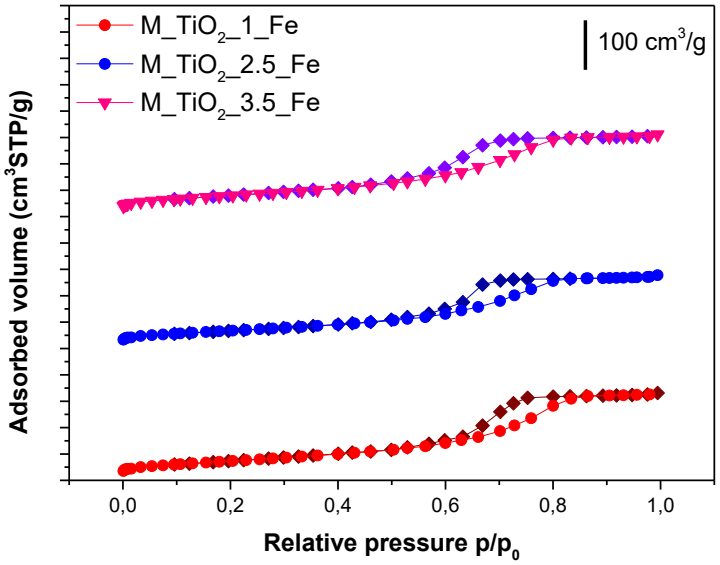

Figure 56. N_2 adsorption/desorption isotherms at −196 ◦C obtained with the following samples: M-TiO_2_3.5_Fe (red), M-TiO_2_2.5_Fe (blue), and M-TiO_2_1_Fe (violet). [20] Isotherms were shifted vertically for graphical reasons.

The effects of iron on the SSA and total pore volume values reported in Table 8 were negligible but were associated with small variations in the surface properties of the samples.

Table 8. SSA and total pore volume as obtained by applying BET equation to N_2 adsorption-desorption isotherms of M-TiO_2_1_Fe, M-TiO_2_2.5_Fe, and M-TiO_2_3.5_Fe samples M-TiO_2 presented as a benchmark [20]

Sample	SSA [m^2/g]	Total pore volume [cm^3/g]
M-TiO_2	150	0.28
M-TiO_2_1_Fe	135	0.25
M-TiO_2_2.5_Fe	130	0.25
M-TiO_2_3.5_Fe	145	0.24

Figure 57 reports the Kubelka-Munk curves obtained by DR UV–Vis spectroscopy of the samples.

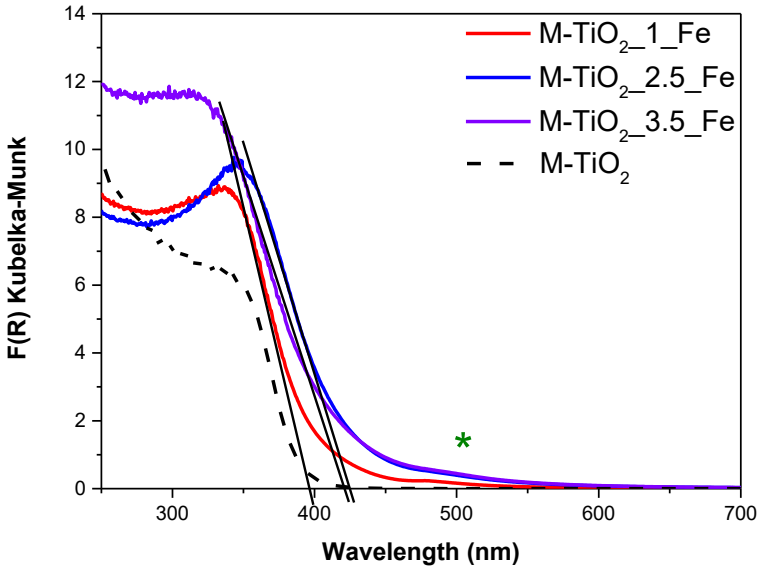

Figure 57. DR-UV-Vis spectra obtained with M-TiO_2_3.5_Fe (red), M-TiO_2_2.5_Fe (blue), M-TiO_2_1_Fe (violet) samples and M-TiO_2 (black dashed line). Band associated with surface iron species at 475 nm evidenced by a green asterisk. [20]

Depending on Fe doping, different absorption onsets were recognized in the Kubelka-Munk curves. In addition, the onset of the curves shifted to a longer wavelength depending on the nominal iron content. Additionally, a new band at 475 nm (green asterisk) was noticed with this set of doped samples, not evidenced in

the undoped sample. The literature ascribes this signal to the d–d transition of octahedrally coordinated Fe^{3+} ions. [159]

Such iron ions were likely located at the surface of the particles and probably belonged to Fe_2O_3 clusters or Fe-oxo/hydroxide clusters. [160][161] The evidence of these iron species on the surface was not detected by XRPD analysis, probably because of their low crystallinity or low amount presence. [160], [161]

The differences in the onset of the Kubelka-Munk and in Tauc's plot (Figure 58) curve demonstrate a variation of the Eg of the studied samples. The presence of the signals correlated with Fe_2O_3 clusters or Fe-oxo/hydroxide clusters were evidenced in Figure 58 by green asterisk and were located at ca. 2.70 eV.

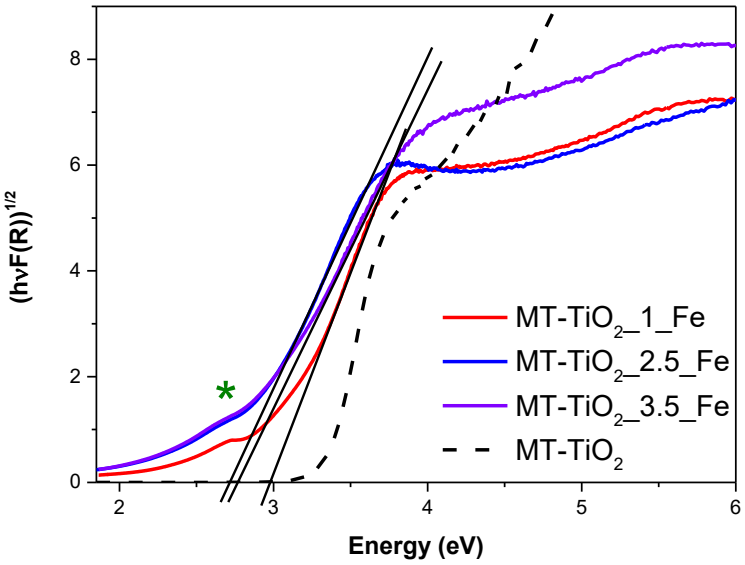

Figure 58. Tauc's plot elaboration for indirect semiconductor applied to M-TiO_2_3.5_Fe (red), M-TiO_2_2.5_Fe (blue), and M-TiO_2_1_Fe (violet) samples.). Band associated with surface iron species at 475 nm evidenced by a green asterisk. [20]

As reported in Table 9. the Eg value decreased by increasing the Fe content, especially up to a nominal content of 2.5 wt.%, while at the highest Fe content, the effect on Eg was smaller. This evidence proved that Fe doping was also effective in the bulk and did not concern only the NPs' surface. [20]

Table 9. Eg values, as obtained from DR UV–Vis spectra by applying different methods M-TiO_2_1_Fe, M-TiO_2_2.5_Fe, and M-TiO_2_3.5_Fe samples M-TiO_2 presented as a benchmark [20]

Sample	Eg extrapolated from Kubelka Munk curve[eV]	Eg extrapolated from Tauc Plot[eV]
M-TiO_2	3.28	3.35
M-TiO_2_1_Fe	3.10	3.01
M-TiO_2_2.5_Fe	2.88	2.74
M-TiO_2_3.5_Fe	2.99	2.70

Figure 59 shows the FTIR spectra of the studied samples. The outgassing procedure was necessary to remove weakly physisorbed water molecules, but no further thermal treatment was performed in this case. The bands correlated to carbonates and bicarbonates species, and the hydroxyl region did not show relevant differences among the studied samples.

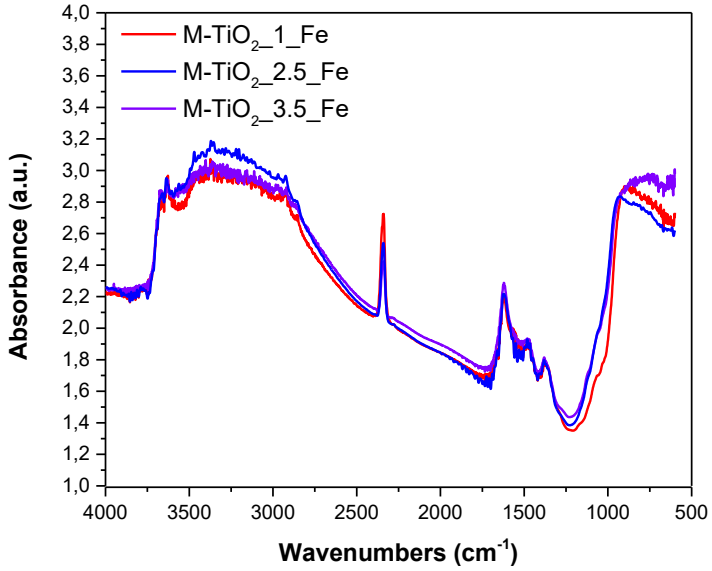

Figure 59. FTIR spectra obtained for M-TiO_2_3.5_Fe (red), M-TiO_2_2.5_Fe (blue), and M-TiO_2_1_Fe (violet) samples [20] outgassed at room temperature.

Figure 60 reports the IR spectra (OH stretching range: 3800–3000 cm^{-1}) of two selected samples, namely, the M-TiO_2 sample and the M-TiO_2_2.5_Fe sample (at intermediate Fe content) after prolonged evacuation at room temperature, in order to remove weakly physisorbed water molecules, without further perturbing the surface. [20]

The hydroxyl region spectra were dominated by the presence of the H- bond due to adsorbed water. The bands at 3630 cm^{-1} and ~3460 cm^{-1}(green asterisk) were ascribed to the asymmetric and symmetric OH stretching modes of H_2O molecules strongly adsorbed on Ti^{4+} sites.[136] The bands at 3674 and 3644 cm^{-1} were ascribed to different types of Ti-OH species, usually observed at the surface of anatase crystalline planes. [137] The band at 3360 cm^{-1} (red asterisk) was peculiar to the M-TiO_2_2.5_Fe sample and was tentatively ascribed to the presence of another kind of OH species induced by the presence of Fe at the NPs' surface. [162] The same band was hardly discernible with the M-TiO_2_1_Fe sample but still visible with the M-TiO_2_3.5_Fe sample, in agreement with the low and high Fe contents. [20]

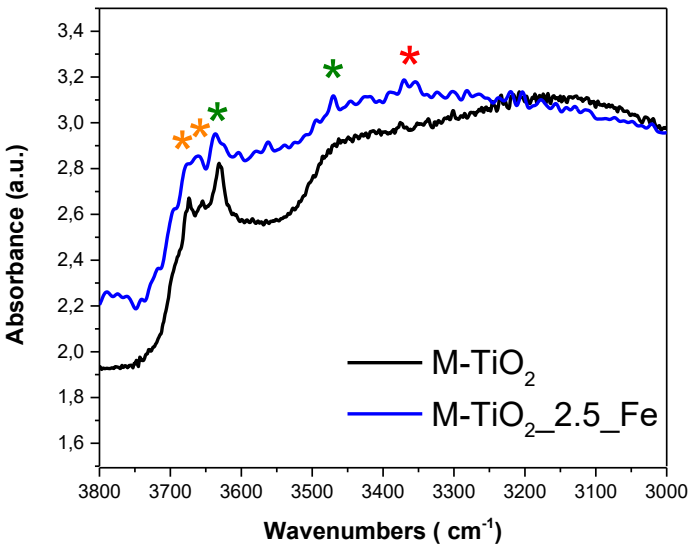

Figure 60. FTIR extract of spectra of M-TiO_2 and M-TiO_2_2.5_Fe outgassed at room temperature peculiar band of the doped sample at 3360 cm^{-1}(red asterisk), bands associated to H_2O molecules strongly adsorbed on Ti^{4+} sites (green asterisk) and Ti-OH correlated bands (orange asterisk).

Figure 61 shows selected TEM images obtained with M-TiO_2_2.5_Fe sample and undoped M-TiO_2 for morphological properties comparison.

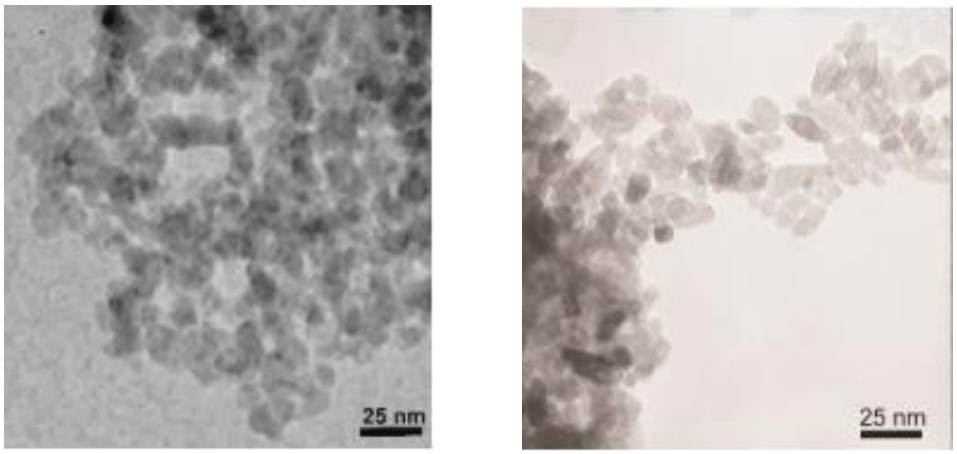

Figure 61. Selected TEM images of M-TiO_2_2.5_Fe (left) and M-TiO_2 (right).[163]

In the TEM micrograph obtained with the M-TiO_2_2.5_Fe sample, uniform morphology was observed with elongated particles, consistent dimensions, and partial agglomeration/aggregation leading to intra and interparticle mesoporosity. No differences between the two samples were recognized, indicating Fe-doping did not influence NPs morphology. The NPs dimensions was in agreement with crystallite size obtained by WH method suggesting monocrystalline nanoparticles for both samples.

Figure 62 shows ζ-potential curves obtained by measuring the electrophoretic mobility as a function of pH obtained with the studied samples.

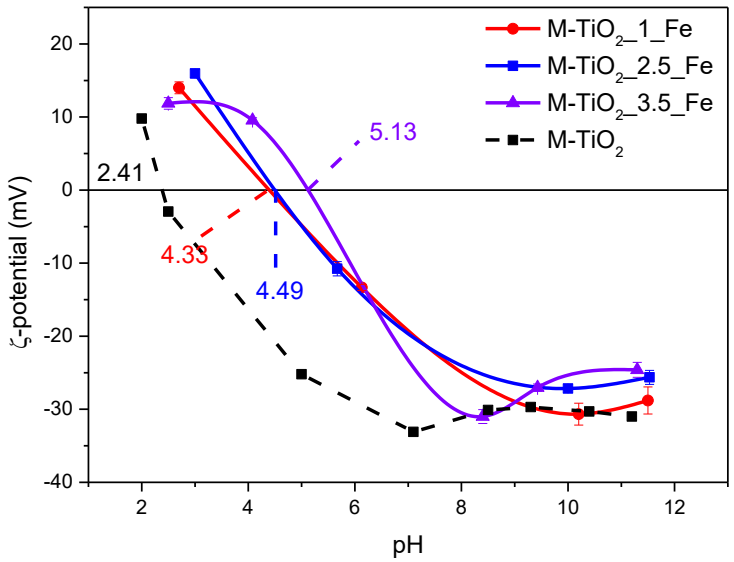

Figure 62. ζ-potential curves obtained by measuring the electrophoretic mobility as a function of pH obtained with M-TiO_2_3.5_Fe (red), M-TiO_2_2.5_Fe (blue), M-TiO_2_1_Fe (violet) samples and M-TiO_2(dashed black line). [20]

The pH_{IEP} obtained with iron-doped M-TiO_2 was more basic than the undoped sample (pH_{IEP} was 2.41). Hence, iron doping induced an increase in surface basicity. The surface basicity plays a role in during photocatalytic processes because it influence the absorption of pollutants.[164]

The differences in the pH_{IEP} indicated the occurrence of Fe species at the NPs' surface. According to the literature, Fe_2O_3 exhibited a pH_{IEP} in an aqueous solution between 5.80 and 6.20 [165]. Consequently, the shift to the basic pH of the pH_{IEP} of this set of samples can be due to the presence of Fe_2O_3 clusters or Fe-oxo/hydroxide clusters on the surface of nanoparticles.

Further information about iron presence on the surface of the NPs of this set of samples was evidenced by XPS survey analysis. (Table 10)

Table 10. Nominal and obtained by XPS analysis content of iron atoms measured for the 3 doped M-TiO_2 sample.

Samples	Nominal Fe/Ti atomic ratio	XPS surface Fe/Ti atomic ratio
M-TiO_2_1_Fe	0.014	0.034
M-TiO_2_2.5_Fe	0.037	0.069
M-TiO_2_3.5_Fe	0.052	0.128

The iron/titanium atomic ratios obtained by XPS analysis were higher than the nominal values expected according to stoichiometric calculation. This experimental evidence confirmed the trend observed by other techniques concerning the iron species' presence on the surface of the NPs.

5.1.3 Discussion

The iron-doped M-TiO_2 set of samples confirmed the advantages offered by the soft template-assisted synthesis method, like high specific surface area and intraparticle and interparticle mesoporosity.[20]

With iron doping, a decrease in crystallite size was observed, promoted by the effect of iron ions during the synthesis on the bulk of the material. [158] However, XRPD analysis recognized anatase as a unique polymorphic structure. [20] Interestingly, the effect of iron on the cell volume was opposite to the influence on crystallite size. An increased cell volume was measured with iron introduction.

Regarding the effects on the material's electronic properties, a decrease of the Eg was evidenced with doped samples up to a certain nominal content (2.5 wt%). [20] This evidence showed the influence of iron doping on the bulk of the material.

The surface properties of the nanoparticles were influenced by the iron presence, with a moderate decrease in SSA and total pore volume values. Furthermore, the formation of iron-rich species like Fe_2O_3 clusters or Fe-oxo/hydroxide clusters on the surface of the nanoparticles was confirmed by different techniques like FTIR, XPS, DR-UV-Vis, and by ζ-potential curves analysis.

The NPs elongated shape and their agglomeration was not influenced by iron doping as demonstrated by TEM images. By comparison of NPs dimensions with HRTEM images and WH analysis of XR diffractograms was proposed the monocristallinity of NPs.

5.2 Iron-doped mesoporous TiO_2 obtained by reverse micelles-assisted sol-gel synthesis method

The analysis of the effects of iron doping on physical/chemical properties of mesoporous titania obtained by a reverse micelles-assisted sol-gel synthesis is reported below. The samples were named depending on the nominal weight percentage of iron with the general name RM-TiO_2_X_Fe where X is the weight percentage of iron added during the synthesis.

5.2.1 Synthesis

The Fe-doped TiO2 NPs with nominal iron contents of 1, 2.5, and 3.5 wt. % were prepared by following the reverse-micelles assisted sol-gel method as detailed in the following and schematically resumed in Figure 63:34.35 g of the di-block copolymer (polyoxyethylene (20) oleyl ether, also known commercially as Brij O20) was dissolved in 150 ml cyclohexane (oil) phase by stirring at 50 °C. Then, in 4.5 ml of bidistilled water was dissolved the proper amount of iron(III) chloride hexahydrate, $FeCl_3 \cdot 6H_2O$ (0.132 g, 0.331 g, and 0.465g to obtain RM-TiO_2_1 _Fe, RM-TiO_2_2.5 _Fe, and RM-TiO_2_3.5_Fe respectively.

The obtained solution was added to the cyclohexane mixture and stirred for 45 min, forming a water-in-oil (w/o) microemulsion in which micelles act as surfactant-encapsulated aqueous nanoreactors. 12.015 mL titanium(IV) butoxide (Ti(O(CH2)3CH3), 98%) was then slowly added to the microemulsion, which was isothermally (50 °C) stirred for 2 h.

Finally, the microemulsion was broken by adding 150 mL of 2-propanol and sonicated. The resulting solid was rinsed with water and ethanol and separated by centrifugation. Finally, the solid was dried at 100 °C for 12 h and calcined for 2 h in air at 500 °C with a temperature increase rate of 2.5 °C min^{-1} to burn the surfactant and promote crystallization. [131], [141], [142]

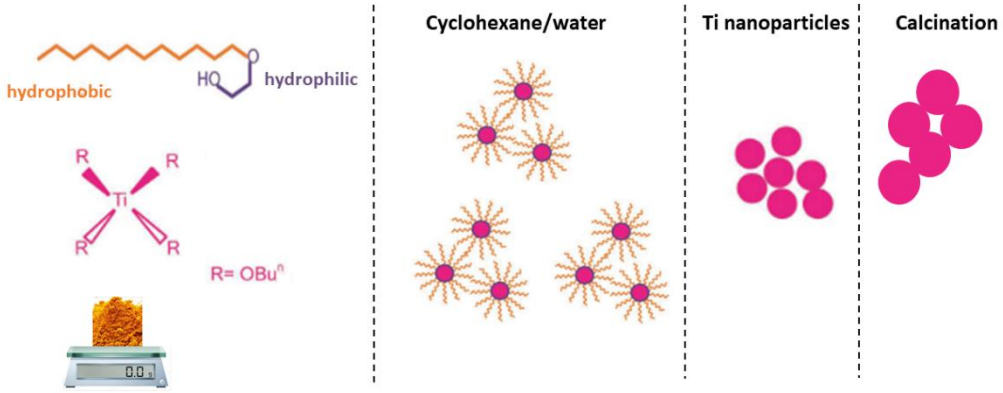

Figure 63 Simplified scheme of the steps leading to the production of TiO_2 NPs using reverse micelle-assisted sol-gel synthesis (adapted from [83])

5.2.2 Physico-chemical characterization

The physicochemical characterization of the sample proposed in the n following paragraphs included:

- XRPD analysis.
- N_2 adsorption-desorption isotherms at -196°C analysis.
- DR UV-Vis spectroscopy.
- FE-SEM micrograph.
- XPS analysis.
- ζ-potential curve measurement.

Figure 64 shows the diffractograms of the doped RM-TiO_2 set of samples. By the diffractograms analysis, a mixed polymorphic structure was observed for the whole set of samples.

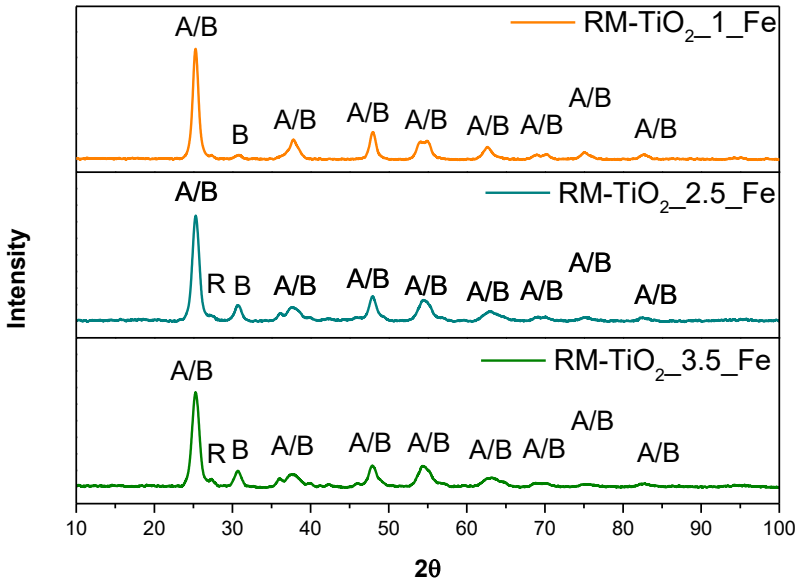

Figure 64. XRPD diffractograms of RM-TiO_2_1_Fe (orange) RM-TiO_2_2.5_Fe (light blue) and RM-TiO_2_3.5_Fe (green).

Along with the peaks of anatase (at 25.2 (101), 37.8 (004), 47.9 (200), 53.8 (105), 54.9 (211), 62.6 (204), 68.7 (116) 2θ values), a weak and broad peak due to the (121) brookite crystalline plane diffraction was observed at about 30.7 2θ.[27] The presence of rutile was evidenced by a unique and very weak peak at 27.4 2θ typical of the (110) plane.[143] The peaks were assigned according to the following reference cards: JCPDS file: 01-078-2486 for anatase, JCPDS file: 01-083-2242 for rutile, and CPDS file: 96-900-4138 for brookite. [131]

The peak at 27.4 2θ assigned to rutile was barely visible for the sample RM - TiO_2_ 1_Fe but it became more evident with a higher amount of Fe. The diffractograms show that several peaks due to brookite and anatase (at 25.2 (101), 37.8 (004), 47.9 (200), 53.8 (105), 54.9 (211), 62.6 (204), 68.7 (116) 2θ values) overlapped due to peak broadening

Peak broadening was explained by W-H analysis of diffractograms that evidenced the presence of small crystallites (Table 11). Furthermore, the QPA was carried out by Rietveld refinement, and the polymorphic structure composition was obtained and reported in Table 11. [131]

Table 11. Polymorphic structure abundance as obtained by QPA analysis and crystallite size as obtained by Williamson-Hall method of doped and undoped RM-TiO_2.

Sample	Anatase		Rutile		Brookite	
	Abundance (wt%)	Crystallite Size (nm) (±)	Abundance (wt%)	Crystallite Size (nm)	Abundance (wt%)	Crystallite Size (nm)
RM-TiO_2	84.3	7.4 (0.2)	0.1	N/A	15.6	7.2 (0.3)
RM_TiO_2_ 1Fe	82.2	8.2 (0.2)	0.1	12.1 (0.3)	15.6	7.2 (0.3)
RM -TiO_2_ 2.5 Fe	54.1	7.1 (0.2)	3.6	10.3 (0.4)	42.4	7.5 (0.1)
RM -TiO_2_ 3.5 Fe	51.9	6.5 (0.2)	6.6	9.0 (0.2)	41.5	7.9 (0.1)

As previously described, the presence of rutile is negligible in the sample RM -TiO_2_ 1Fe while it increased with the amount of iron. QPA (Table 11) showed the increase of the rutile phase at the expense of anatase, while the brookite content was similar for the whole set of samples.

This evidence could be noticed by observing the diffractograms where the brookite-related peak at 30.8 2θ showed the same intensity for the whole set of samples. On the other hand, a decreased intensity of other peaks assignable only or mainly to anatase (for example, the peaks at 53.8, 55.0, and 62.6 2θ) was noticed.

The possible explanation for these changes in the phase composition of the samples was the presence of Fe^{3+} ions within the reverse micelles' core. The presence of iron ions can have two main effects on brookite formation:[131][11]

- pH lowering
- Coordination agent for nucleation of crystals

During the synthesis, the pH of the iron precursor salt and water solution reached values around 2.

The coordination effect of ions during the synthesis was already observed by using the same synthesis procedure with other metallic dopants. [91][166] [11].

The rutile formation should occur at a higher calcination temperature than the adopted one (450°C). The rutile content increase could be due to brookite presence, which may favor the anatase-to-rutile thermal transition[163][146]. Furthermore,

the Fe^{3+} ions presence defined as “low charge cations” (i.e., <+4), can act as anatase-to-rutile transition promoters[14].

Figure 65 shows the variation of crystallite size (a) and cell volume of the polymorphic structures (b) with the variation of nominal Fe percentage.

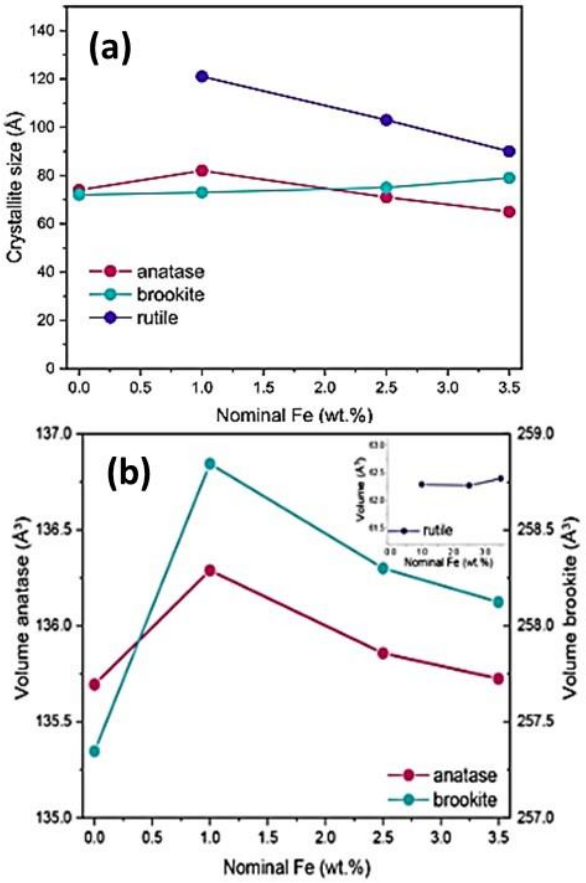

Figure 65. (a) Trend of the crystallite size versus the nominal Fe content (wt.%) for anatase, rutile, and brookite (s) and trend of the cell volumes of the three polymorphs versus the nominal Fe content (wt.%) (b).[131]

The effect of iron weight percentage on the crystallite size was presented in Figure 65a. where the pronounced influence on rutile and anatase crystallites was shown. On the other hand, brookite’s crystallite sizes seemed not influenced by the iron introduction in the lattice.

The difficulties in assessing the rutile amount in the RM_TiO_2_1_Fe sample described before hampered the possibility of monitoring the variation of the rutile cell dimension in the case of rutile. The most significant changes in cell volume with increased iron doping were observed with anatase and brookite in RM - TiO_2__RM_1_Fe sample. [131]. The anatase and brookite cell volume increased at

1 wt.% Fe while a decrease in cell dimension was observed with the higher amount of iron introduced in the samples.

The possible explanation, already observed in the literature [166], with this synthesis method was the formation of a substitutional solid solution with iron atoms replacing titanium atoms in the TiO_2 lattice. The isomorphic substitution of Ti^{4+} by Fe^{3+} ions was possible according to similar ionic radium 0.75 and 0.79 Å, respectively.[35]

The consequent decrease of the cell volume at higher iron loading was explained by the inability of iron atoms to enter the TiO_2 lattice anymore. Consequently, iron ions were forced into interstitial sites.[131]

The nitrogen isotherms measured at −196 °C on this set of samples reported in Figure 66 showed, even in this case, a type IV isotherm with an H2-type hysteresis loop due to capillary condensation within inter-particle mesopores.

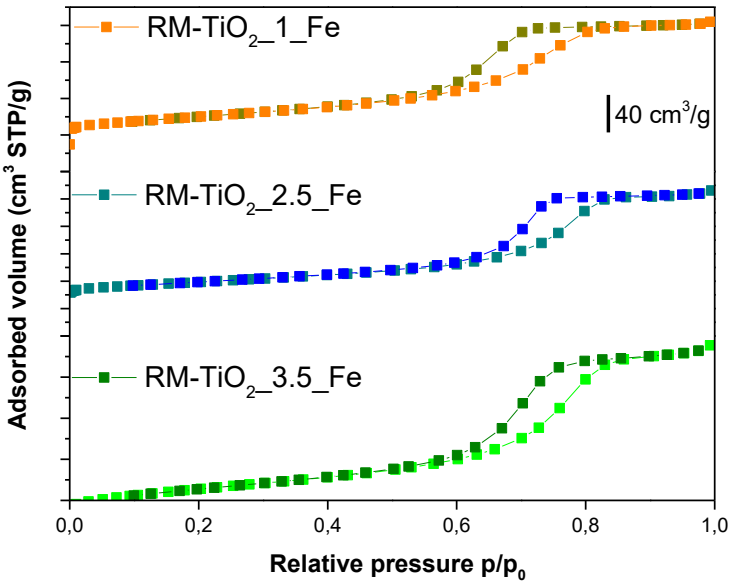

Figure 66. N_2 adsorption-desorption of RM-TiO_2_1_Fe (orange) RM-TiO_2_2.5_Fe (light blue) and RM-TiO_2_3.5_Fe (green) samples Isotherms were shifted vertically for graphical reasons.

The effects of iron doping on SSA and total pore volume are summarized in Table 12. Iron doping had a limited effect on the surface properties of RM-TiO_2_1_Fe, whereas 2.5 wt.% Fe led to both higher porosity and SSA compared to undoped samples. The SSA increasing with iron content was not observed with 3.5

wt.% Fe. Such behaviour was probably due to the presence of surface iron species already evidenced in the case of iron-doped M-TiO_2 (paragraph 5.1.2).

Table 12 SSA and total pore volume as obtained by applying BET equation to N_2 adsorption-desorption isotherms of RM-TiO_2_1_Fe, RM-TiO_2_2.5_Fe, and RM-TiO_2_3.5_Fe samples RM-TiO_2 was presented as a benchmark. [20]

Sample	**SSA [m^2/g]**	**Total pore volume [cm^3/g]**
RM-TiO_2	105	0.203
RM-TiO_2_1_Fe	106	0.203
RM-TiO_2_2.5_Fe	116	0.212
RM-TiO_2_3.5_Fe	98	0.252

Figure 67 reports the Kubelka-Munk curve obtained by diffuse reflectance UV-Vis spectroscopy with undoped RM-TiO_2 and iron-doped RM-TiO_2 samples. The samples showed a strong absorption band at ca. 230 nm associated with the charge transfer transition from O^{2-} to Ti^{4+} species. [131]

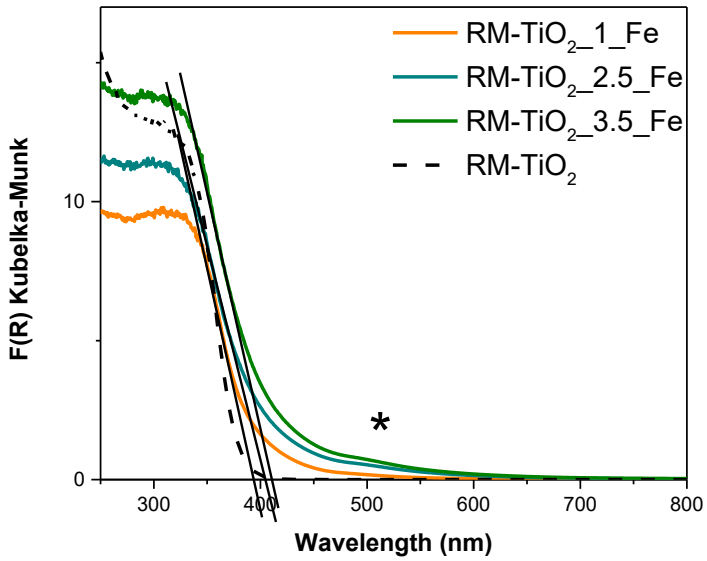

Figure 67 DR-UV-Vis spectra obtained with RM-TiO_2_1_Fe (orange curve) RM-TiO_2_2.5_Fe (light blue curve), RM-TiO_2_3.5_Fe (green curve) samples and RM-TiO_2 (black dashed line). Band associated to surface iron species at 490 nm evidenced by black asterisk.

As confirmed by the literature, the iron doping increase led to the bathochromic shift (red shift) of the onset of the Kubelka-Munk curves. [41] The presence of iron also induced the formation of a broad absorption at ca. 490 nm (asterisk), likely due to the d-d transitions of Fe^{3+} ions [37], [167], [168] in Fe-oxohydroxo clusters at the surface of the NPs. These species were already observed in the literature when other synthesis methods were used to obtain Fe-doped TiO_2 powders (i.e.Fe-doped M-TiO_2 samples described in paragraph 5.1.2) or other Fe-doped materials. [20], [161], [163]

The proposed Tauc's plot (Figure 68) was obtained from Kubelka-Munk curves with mathematical elaborations considering indirect semiconductors since anatase was the most abundant polymorph.

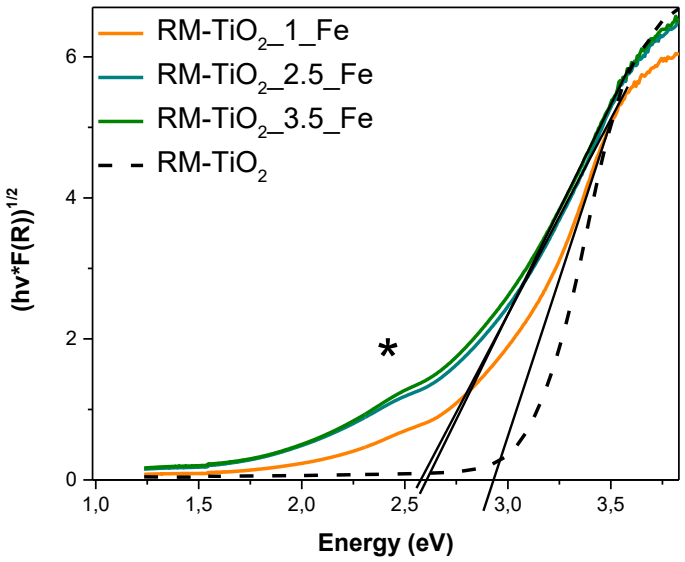

Figure 68. Tauc's plot elaboration for indirect semiconductor applied to RM-TiO_2_1_Fe (orange curve) RM-TiO_2_2.5_Fe (light blue curve), RM-TiO_2_3.5_Fe (green curve) and RM-TiO_2 (black dashed line) samples. Band associated to surface iron species at 2.3 eV evidenced by black asterisk.

The Eg values (Table 13), extrapolated by linear fitting of the curves, decreased up to 2.5 % weight iron introduction. However, further increase of iron doping did not lead to a significant reduction of Eg. Probably, the phenomenon occurring at higher iron loading was the formation of larger Fe-oxohydroxo clusters on the surface of TiO_2, reducing the iron ions penetrating inside the lattice. Another explanation was proposed in literature where the change between interstitial and substitutional doping induced different mid-gap states. [169] According to the variation of the cell volume and the hypothesis of iron ions forcing to interstitial sites of the lattice above 1%wt of iron, the similarities of the Eg values between RM-TiO_2_2.5_Fe and TiO_2_3.5_Fe could be explained.

Table 13. Eg values, as obtained from DR UV–Vis spectra by applying linear extrapolation of the absorption edge and by applying Tauc's plot method for indirect semiconductors on RM-TiO_2_1_Fe, RM-TiO_2_2.5_Fe and RM-TiO_2_3.5_Fe samples RM-TiO_2 presented as a benchmark.

Sample	**Eg extrapolated from Kubelka Munk curve[eV]**	**Eg extrapolated from Tauc Plot Indirect Semicon. [eV]**
RM_TiO_2	3.31	3.13
RM_TiO_2_1_Fe	3.22	2.97
RM_TiO_2_2.5_Fe	3.00	2.65
RM-TiO_2_3.5_Fe	3.03	2.65

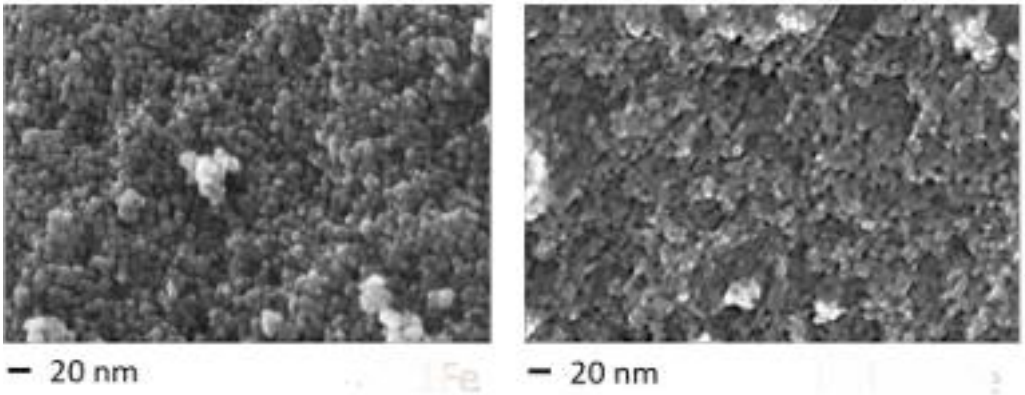

Figure 69 FE-SEM micrographs of RM-TiO_2_1_Fe (left) and RM-TiO_2_2.5_Fe (right) [131]

In the FE-SEM micrographs of RM-TiO_2_1_Fe and RM-TiO_2_2.5_Fe samples (Figure 69) round-shaped NPs were observed. NPs showed a round shape with homogenous size (ca. crystallite size), showing agglomeration/aggregation. The presence of surface iron species did not affect NPs morphology and agglomeration in this case, as already shown in the literature. [91], [166], [170]

The HR XP spectra reported in Figure 70 report the Ti 2p and the O1s lines obtained by iron-doped samples analysis.

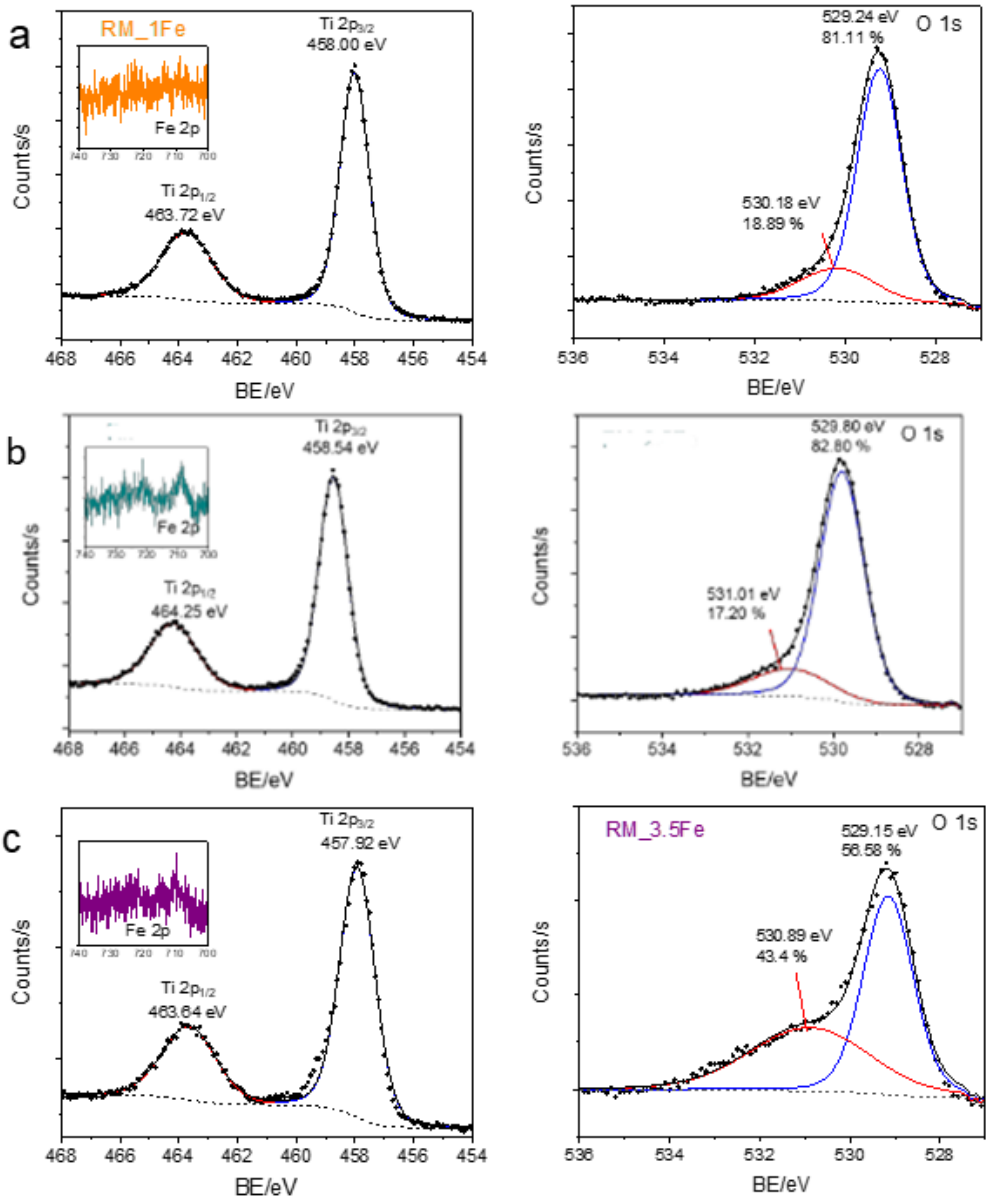

Figure 70 . HR spectra (Ti2p line analysis (left) and O 1s (right) obtained by RM-TiO_2_1_Fe (a line) RM-TiO_2_2.5_Fe (b line). RM-TiO_2_3.5_Fe (c line) samples analysis.

The analysis of the Ti 2p line led to the evidence that the typical spin-orbit splitting doublet of Ti $2p_{3/2}$ and Ti $2p_{1/2}$ states are constant. All the samples, including the undoped one, showed an observed splitting equal to 5.7, confirming the presence of only Ti^{4+} states. [171] Furthermore, the Ti 2p peaks shifted to lower BE values for doped samples. This effect was already observed in the literature with

Fe-doped TiO_2 and was assigned to Ti ions substitution by Fe^{3+} ions in the lattice.[172]

Concerning the O 1s line (right column), all the samples showed two components: the band at the lower BE was assigned to lattice oxygen (O^{2-}) species, and the one at the higher BE to surface adsorbed water or OH groups [172].

The relative abundance of the higher BE band is much higher with the RM_TiO_2_3.5_Fe sample. [172] This evidence confirmed the presence of Fe-oxo/hydroxo clusters on the surface of the NPs already proposed by other characterization methods.

Finally, the opportunity to study Fe 2p lines was evaluated (insets on the left column). The low amount of doping with respect to the parent matrix hampered any curve-fitting procedure, as Fe 2p lines were weak in intensity and extremely noisy. Other information obtained by XPS analysis, in this case, by standard survey analysis of elements in the first few atomic layers of the NPs, is reported in Table 14.

Table 14. XPS survey analysis of the surface of iron-doped RM-TiO_2

Samples	**Nominal Fe/Ti atomic ratio**	**XPS surface Fe/Ti atomic ratio**
RM-TiO_2_1_Fe	0.014	< 0.0048
RM-TiO_2_2.5_Fe	0.037	0.021
RM-TiO_2_3.5_Fe	0.052	0.120

Evidence of a preferential positioning of iron atoms on the surface with increased iron doping was shown only for the RM-TiO_2_3.5_Fe sample.

Figure 71 reports the ζ-potential curves of iron-doped RM-TiO_2. The differences between the three samples regarding the pH_{IEP} were negligible, even with a change in iron doping. The presence of the surface Fe species did not significatly affect the pH_{IEP}, as the undoped sample showed a pH_{IEP} of 3.5. According to the literature, the pH_{IEP} of Fe_2O_3 is found at higher pH (between 5.80 and 6.20). [165]

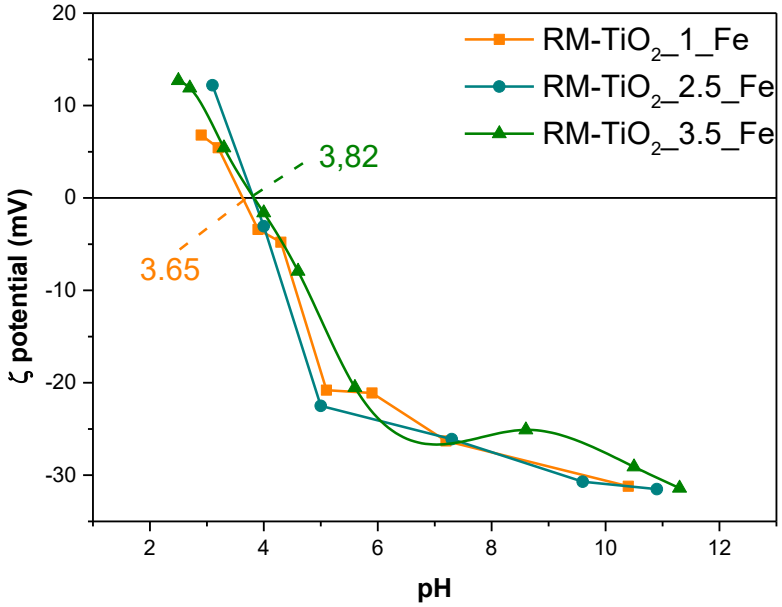

Figure 71. ζ potential curves of iron-doped RM-TiO_2 set of samples

According to the literature, the stability of a suspension is guaranteed with a ζ-potential below +30 and -30.[139], [158] For this reason, the stability of the NPs suspension in water was not guaranteed. At the same time, suspended particles showed a negative charge for a pH higher than 3.8 for the whole set of samples.

5.2.3 Discussion

The main properties of this set of samples were similar to the undoped RM-TiO_2 sample valorizing the evidence that the reverse micelles-assisted sol-gel method was optimized even for doped samples. The obtained samples were composed of agglomerated round nanoparticles with inter-particle mesopores.

This set of samples characterized in this chapter offered some insights into the iron doping effect on titania samples. XRPD diffractograms analysis provided evidence of the iron influence on the polymorphic structure. According to QPA, iron presence affected: rutile (moderate) and brookite (intense) contents.

Another result was the study of the possible substitutional/interstitial positioning of iron ions inside the TiO_2 matrix. Analysis of cell volumes, by XRPD diffractogram elaborations, showed an iron ions concentration threshold (1 %weight) upon which the substitutional solution is no longer possible, and iron atoms likely occupied interstitial sites of the TiO_2 cells.

By DR-UV-Vis spectroscopy, the formation of Fe_2O_3 clusters or Fe-oxo/hydroxide clusters on the surface of the NPs was evidenced for the whole set of samples. However, with a low weight percentage of iron introduced (1 and 2.5), the effects on the bulk of the titania samples, i.e., energy gap reduction, were noticed, confirming the effective inclusion of iron in the crystalline structure.

At higher iron content (3.5 wt. %), the reduction of the Eg was not evidenced, and by XPS analysis was possible to notice a preferential positioning of iron atoms in the first atomic layers (reaching a value higher than the nominal amount).

The peculiarity evidenced by the ζ-potential curves analysis where the presence of Fe-oxohydroxide clusters on the samples' surface did not influence the pH_{IEP}. However, in the iron-doped M-TiO_2 samples (paragraph 5.1.2.), a correlation between iron-rich clusters on the surface and the trend of the ζ-potential curve was evidenced. The possible explanations were differences in the dimensions and distribution of iron-rich clusters or an increased inclusion of iron atoms inside the NPs obtained by the reverse micelles-assisted sol-gel synthesis method.

5.3 Iron-doped template-free Mesoporous TiO_2

The analysis of the effects of iron doping on mesoporous titania obtained by a template-free sol-gel method is reported below. Different amounts of iron precursor were introduced during the synthesis to estimate the differences among samples.

The samples were named depending on the weight percentage of iron concerning titanium introduced. The generic name was AB_X_Fe, where X stands for the weight percentage of iron raised.

In this set of samples, a new weight percentage of iron (0.05 %wt) was proposed. The literature showed that the positive effects of iron doping commonly reached a certain percentage, and then for higher amounts, the photocatalytic properties of the material decreased. [42], [43]This effect was attributed to the enhanced recombination of energy carriers induced by mid-gap state. [44] Conversely, the mid-gap states can promote the charge separation of energy carriers by temporally trapping one between e^- or h^+ and letting the other migrate to the surface to interact with adsorbed species. [44] The trapping effect can be detrimental when the trap states are too deep (in the Eg) because, in this case, these extra levels would promote recombination. Furthermore, when the dopant atom's presence induces this trapping mechanism even far from the surface, the charge carriers would be trapped many times before reaching the surface. [44] For all these reasons, Zhang et al.; proposed that the doping amount should be tuned depending

on particle size. For large particles, bulk doping should be avoided to inhibit the multiple-trapping effect induced by a large amount of doping in the bulk of nanoparticles. [44]

5.3.1 Synthesis

The doped anatase/brookite TiO_2 mixed-phase samples were synthesized according to a template-free sol-gel method under pH control briefly schematized in Figure 72 Simplified scheme of the steps leading to the production of TiO_2 NPs using template free sol-gel synthesis (adapted from [83]). [31] In a 150 mL beaker, 10.0 mL $Ti(OPr)_4$ (titanium(IV) isopropoxide, 97%) was mixed with 10.0 mL isopropyl alcohol (≥99.8%): the solution was then stirred for 20 min at 500 rpm. To the solution was added 100 mL of bi-distilled water where the proper amount of $FeCl_36H_2O$ (Iron(III) chloride hexahydrate, 97%) was dissolved.

The $Ti(OPr)_4$/isopropyl alcohol/water mixture was poured into a Teflon autoclave, heated inside a stove for 5 h at 80 ◦C, and cooled to room temperature. The solution pH was then changed by dropwise adding 1.0 M HNO_3 solution until a pH equal to 2.0 was obtained. The acidic solution was stirred at room temperature for 20 h to obtain a gel, which was repeatedly washed with bi-distilled water and isopropanol and centrifuged. Then, it was dried at 100 ◦C for 12 h in a stove and calcined at 200 ◦C for 2 h obtaining the iron-doped AB samples. Finally, the powder was washed four times using an ethanol/water (1/3) mixture, centrifuged, and dried for 24 h at 60°C. [31][173]

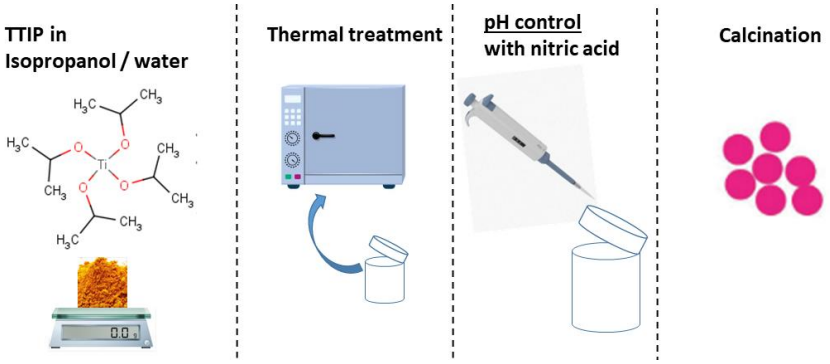

Figure 72 Simplified scheme of the steps leading to the production of TiO_2 NPs using template free sol-gel synthesis (adapted from [83])

5.3.2 Physico-chemical Characterization

The physico-chemical characterization of the sample proposed in the following paragraphs included:

- XRPD analysis.
- N_2 adsorption-desorption isotherms at -196°C analysis.
- DR UV-Vis spectroscopy of the powders.
- FE-SEM micrograph analysis.
- XPS analysis.
- ζ-potential curve measurement.

Figure 73 shows the diffractograms of iron-doped AB samples. The shape of the peaks suggested a low crystallinity of the samples already observed in the undoped sample (Figure 43). This low crystallinity was due to the low calcination temperature (200°C).

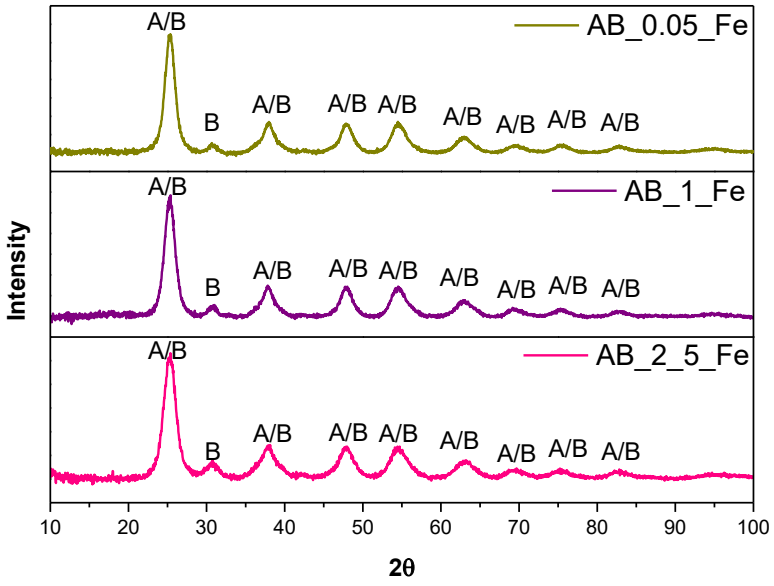

Figure 73. XRPD diffractograms of iron-doped AB sample: AB_0.05_Fe (yellow curve) AB_1_Fe (violet curve), and AB_2.5_Fe (pink curve).

As shown in Figure 73, a slight decrease in anatase and brookite crystallite size was noticed, with average crystallite size dropping respectively from 5.2 and 7.1 nm to 4.4 and 5.7 nm in the AB_2.5Fe sample.[31]

As already demonstrated in the literature, the small dimension of crystals in the case of iron doping is due to the presence of Fe^{3+} ions. This effect of crystalline domain dimension reduction is due to a retardation of crystalline growth due to Fe^{3+} ions in the anatase/brookite system. [158]

Furthermore, the effects of iron weight percentage on the cell volume of polymorphic structures were investigated. The results of this investigation are reported in Figure 74.

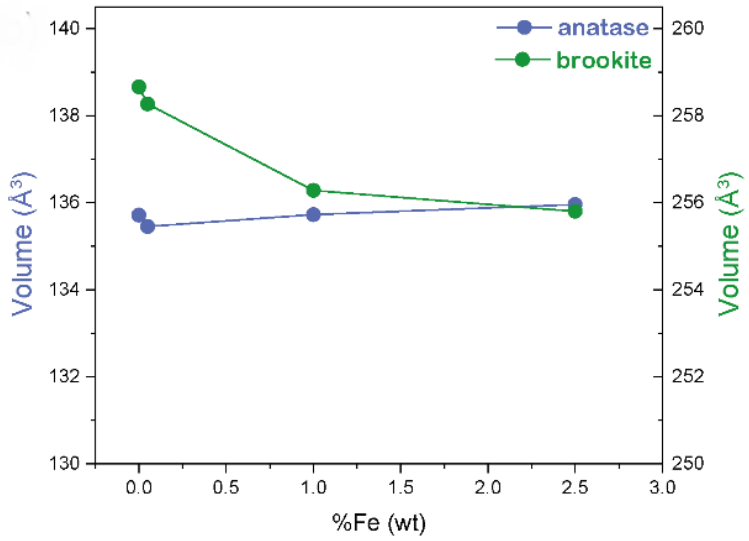

Figure 74. Values of the cell volumes of anatase and brookite versus the nominal Fe content (wt.%). [31]

The effects on brookite's cell volume were evident with different iron doping weight percentages, while anatase cell volume was less affected by iron atoms' presence.

To understand the Fe^{3+} positioning in the iron-doped AB structure is important to remind what was described in paragraph 4.2 where Fe-doped RM-TiO_2 samples were analysed. In that case, the inclusion of iron ions induced a change in anatase and brookite cell volume. In the doped RM-TiO_2 case, an initial expansion of both the anatase and brookite cell volumes occurred at 1.0 wt.% Fe, and then the cell volumes decreased at a Fe content above 1.0 wt.%. The former effect on cell volume was attributed to the isomorphic substitution of Ti^{4+} by Fe^{3+} ions inducing cell volume growth, while the latter was caused by the occupation of interstitial sites by (extra) Fe^{3+} ions. [31][131]

In the case of iron-doped AB samples, the peculiar synthesis procedure helps the latter process (interstitial positioning of Fe^{3+} ions), which mainly affects the brookite phase, characterized by a more disordered and open structure than anatase. [11] Table 15 reports the crystallite size and QPA of the iron-doped AB samples as obtained by Rietveld refinement and W-H method application to the diffractograms.

Table 15. Some relevant data obtained from XRPD of iron-doped AB samples analysis. The resumed values were obtained by Rietveld refinement and Williamson-Hall method applied to diffractograms.

Sample	Anatase		Brookite	
	Abundance (wt%)	Crystallite Size(nm) (±)	Abundance (wt%)	Crystallite Size (nm)
AB	77.7	5.2 (0.2)	22.3	7.1(0.1)
AB_0.05_Fe	76.9	5.0 (0.1)	23.1	5.6 (0.2)
AB_1_Fe	79.3	4.7 (0.1)	20.7	6.0 (0.2)
AB_2.5_Fe	78.4	4.4 (0.1)	21.6	5.7 (0.2)

Figure 75 reports the N_2 adsorption-desorption isotherm at -196°C of iron-doped AB samples. All the studied samples showed type IV isotherms with H2 hysteresis loops. In addition, the same isotherms type was observed with undoped samples (Figure 44) indicating the formation of interconnected mesopores during the template-free synthesis. [31]

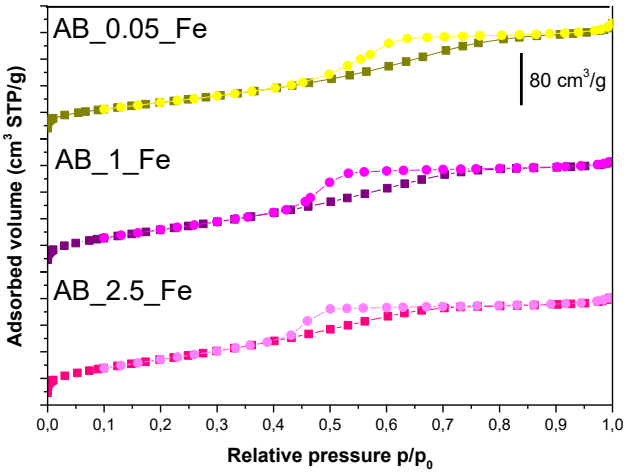

Figure 75. Nitrogen adsorption-desorption isotherms of iron-doped: AB samples AB_0.05_Fe (yellow curve) AB_1_Fe (violet curve) and AB_2.5_Fe (pink curve).

The pore size distribution obtained from the adsorption branch with the BJH method showed differences in pore size with different iron doping. The distribution of pores (Figure 76) was centered at ca. 4 nm for AB_1.0_Fe, and AB_2.5_Fe, as in the undoped sample. However, the AB_0.05_Fe sample showed a broader peak distribution, probably due to some disorder induced by the structure of the surface of the material by this low amount of iron doping. [31]

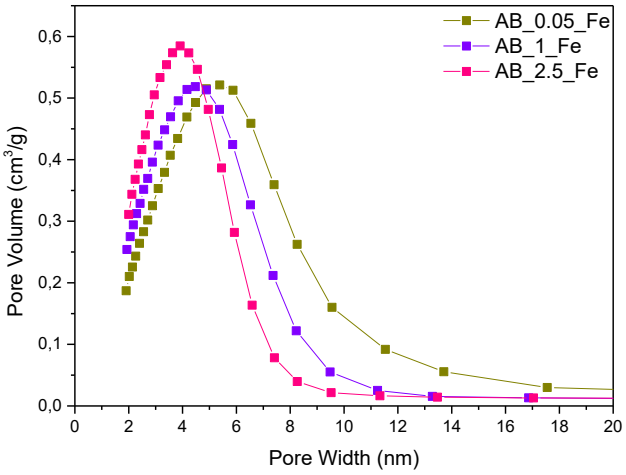

Figure 76 PSD obtained by BJH method applied to the adsorption branch of isotherms of AB_0.05_Fe (yellow curve) AB_1_Fe (violet curve) and AB_2.5_Fe (pink curve).

The iron doping effect on SSA is summarized in Table **16**. The presence of iron induced the growth of specific surface area values except for the AB_0.05_Fe sample, which showed an SSA value almost identical to the undoped sample. [31]

Table 16. N_2 adsorption-desorption obtained data for the iron-doped AB set of samples.

Sample	**SSA [m²/g]**	**Total pore volume [cm³/g]**
AB	236	0.293
AB_ 0.05_Fe	233	0.286
AB_ 1_Fe	243	0.253
AB_ 2.5_ Fe	263	0.245

The Kubelka-Munk curves reported in Figure 77 showed the typical band due to electronic transitions of charge transfer from O^{2-} to Ti^{4+} for the whole set of samples. In addition, the Urbach tail (inset Figure 77) already explained for the undoped sample was still visible in the doped samples.

A peculiarity of the spectrum obtained by AB_0.05_Fe sample analysis was the band at ca. 235 nm that, according to literature, can be assigned to charge transfer (CT) from O^{2-} to Ti^{4+}ions in a perturbed environment. The alteration of the crystalline structure was due to the presence of Fe^{3+} ions within the lattice of the material [17]. The perturbation of the electronic structure observed in AB_0.05_Fe was not marked with the samples at higher iron content. The possible explanation for this unicity can be the higher substitution level of Fe atoms inside the TiO_2 matrix when low amounts of Fe were introduced. [31]

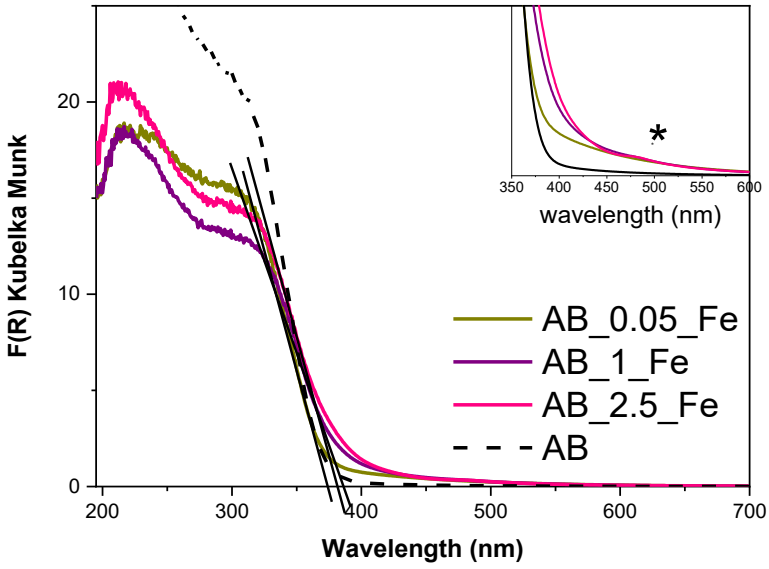

Figure 77. DR-UV-Vis spectra obtained for AB_0.05_Fe (yellow curve) AB_1_Fe (violet curve), AB_2.5_Fe (pink curve) undoped AB (black dotted line) samples. Band associated to surface iron species at 490 nm evidenced by a black asterisk in the inset.

The Tauc's plots reported in Figure 78 were calculated using the Tauc's Plot method for indirect semiconductors due to the higher amount of anatase. However, the samples showed a consistent presence of brookite (direct band gap), and consequently, the Eg values were also extrapolated from the K-M curves.

Tauc's plots showed an influence of iron doping with a red shift of the light absorption and, consequently an effect on the Eg values.

Furthermore, another effect of iron presence was noticed with a high weight percentage of iron (i.e., 2.5 % where the band associated to surface Fe-oxohydroxo clusters (already observed with iron-doped M-TiO_2 and RM-TiO_2 samples) was observed (asterisk).

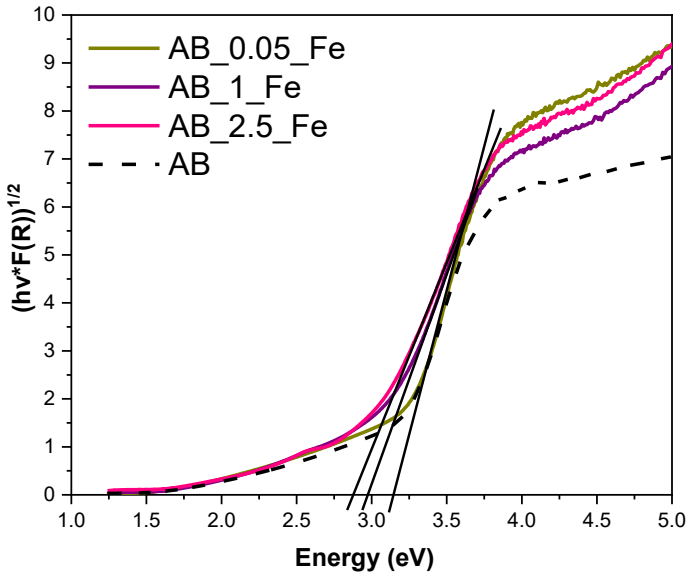

Figure 78. Tauc's plots calculated for indirect material. AB_0.05_Fe (yellow curve) AB_1_Fe (violet curve), AB_2.5_Fe (pink curve) and undoped AB (black dotted line) samples.

Concerning the Eg, iron doping led to a decrease in Eg, as reported in Table 17. This effect was observed with other doped samples and was due to the presence of iron inside the bulk of the material.

Table 17. Eg values of iron-doped AB samples as extrapolated by Kubelka-Munk curve and from Tauc Plot compared with the value extrapolated for undoped AB sample (red).

Sample	Eg extrapolated from Kubelka Munk curve [eV]	Eg extrapolated from Tauc Plot Indirect Semiconductor [eV]
AB	3.31	3.10
AB_ 0.05_Fe	3.22	3.07
AB_ 1_Fe	3.10	2.92
AB_ 2.5_ Fe	3.01	2.85

Figure 79 shows the selected FE-SEM micrographs of the samples, including the undoped one reported for comparison. All the samples showed small NPs with high agglomeration/aggregation, but by analyzing the micrographs, no evidence of the influence of iron doping on the NPs size was observed. [31]

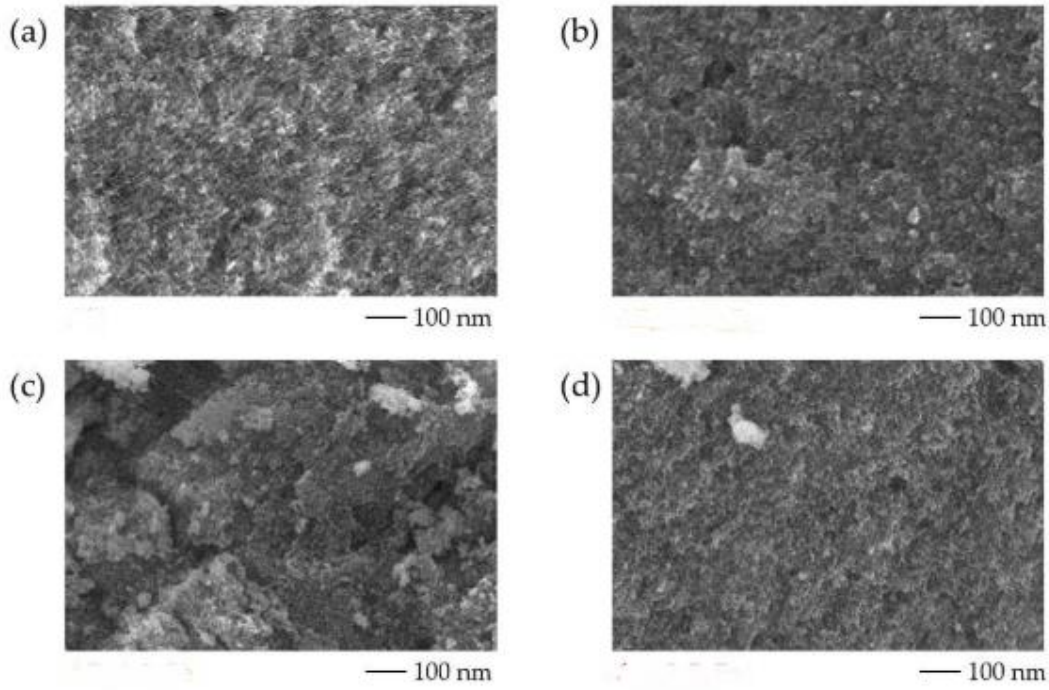

Figure 79. FE-SEM images of the samples: AB (a) AB_0.05_Fe (b) AB_1_Fe (c) AB_2.5_Fe (d).[31]

The EDS maps (not reported) collected during the analysis with FE-SEM showed a homogenous dispersion of iron in the samples. [31] The EDS images

offered the opportunity to notice the presence of iron even in the low-doped sample. This result was possible because EDS analysis detected the presence of iron in the section of the material below the surface. On the other hand, with the present samples, XPS analysis detected the presence of surface Fe atoms only with the AB_2.5_Fe sample. A Fe/Ti atomic ratio equal to 0.071 was measured by XPS, higher than the nominal value of 0.037, indicating that some Fe oxyhydroxide species may occur at higher Fe content. These species' presence was observed even by DR UV-Vis spectroscopy. [31]

Figure 80 reported the ζ potential measurement curves obtained with iron-doped AB samples.

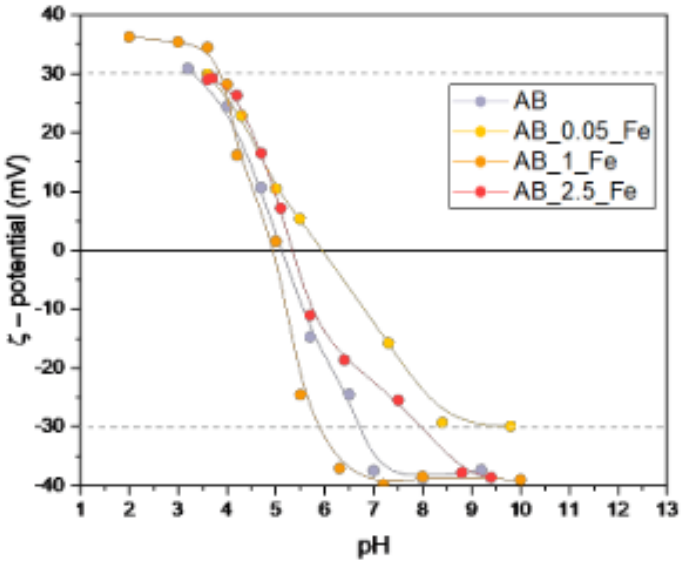

Figure 80. ζ potential measurement curves of doped AB samples and undoped AB samples. [31]

The isoelectric point of the whole set of samples was in the range of 5 to 6. These results were in agreement with the literature as long as the pH_{IEP} of brookite and anatase is around 5.10 and 6.00 [59].

Iron-related species on the surface of the AB_2.5_Fe sample can change the pH_{IEP} but not excessively because Fe_2O_3 has an isoelectric point between 5.80–6.20 [165].

The pH_{IEP} obtained from Figure 80 gave us two primary pieces of information: AB_1.0_Fe and AB_2.5_Fe samples showed pH_{IEP} similar to the undoped sample, while AB_0.05_Fe sample had a slightly higher pH_{IEP}.

Concerning the AB_0.05_Fe sample, the difference in pH_{IEP} was attributed to the higher abundance, on the surface of aggregates, of exposed anatase nanoparticles.[31]

5.3.3 Discussion

The analysed samples obtained by template-free sol-gel synthesis method showed, even in this case, the main properties of the undoped sample, with a mixed polymorphic structure composition and a high SSA compared to other samples presented in previous paragraphs.

The effect of iron doping on the samples was observed through i) some properties influenced by the iron presence, ii) some others not influenced by the iron presence, and iii) some peculiarities obtained with the AB_0.005_Fe sample.

Iron doping did not influence the polymorphic structure composition of the studied samples.

On the other hand, iron introduction inside the samples affected the Eg values of the TiO_2-based materials. A decrease in the Eg was noticed.

Evidence of some changes in the material by introducing a very low amount of iron (0.05 wt %) was detected by different characterization techniques:

- By DR-UV-Vis, the presence of a peculiar band at 235 nm was noticed.
- By ζ-potential measurement, a slight increase in pH_{IEP} was observed.

The most prominent explanation proposed for these peculiarities is the alteration of agglomeration/aggregation of the AB_0.05_Fe sample process due to a low iron content. Furthermore, this alteration in the aggregation/agglomeration caused some changes in the surface properties (i.e., pore size distribution) and within the first atomic layers of the nanoparticles.

Finally, by DR-UV-Vis analysis of the AB_2.5_Fe sample was noticed the presence of Fe_2O_3 clusters or Fe-oxo/hydroxide clusters. Other characterization techniques like XPS and EDS analysis supported these species' existence, showing an iron ion accumulation close to the surface. According to XPS analysis, the obtained Fe/Ti atomic ratio with AB_ 2.5_ Fe was 0.071, which was higher than the nominal value of 0.037 as reported in paragraph 5.3.2.

6 Photocatalytic tests

6.1 Introduction

The photocatalytic tests were performed with the TiO_2-based photocatalysts described in the previous Chapters. The photocatalytic degradation of emerging pollutants described in Chapter 1 was tested with different photocatalysts, and the experimental settings were adapted to the pollutant peculiarities.

The photocatalytic tests aimed to understand the photocatalytic properties of the samples after the physico-chemical characterization with the aim of interconnect the photocatalytic efficiency and the intrinsic aspects of the samples.

Two different strategies were adopted.

- Experimental settings were kept unaltered with a set of pollutants, and the experiments focused on the photocatalyst's properties. Possible by-products and degradation mechanisms were proposed.
- With other TiO_2-based samples commonly used as benchmarks for photocatalytic properties assessment of materials, the photocatalytic process was optimized by the variation of the experimental settings.

6.1.1 Paracetamol, simazine, and N-phenyl-urea photocatalytic tests settings

The photocatalytic degradation of paracetamol and herbicides was investigated with unaltered experimental settings to assess the photocatalytic properties of undoped photocatalysts.

During the photocatalytic test, the reactor used was a quartz testing tube where liquid/solid suspension with a proper concentration (commonly, 1 g/L) was continuously stirred using a magnetic stirrer at ca. 300 rpm. For common quartz material, the absorption of light between 150- 3500 nm is negligible, allowing the exploitation of the whole solar simulated and the UV spectra without absorption by the reactor material. [174]. The reaction mixture was not deaerated; consequently, the atmospheric oxygen was the unique source of oxygen available. No oxygen or air-bubbling-inducing supersaturation in the solution was exploited in the system. The external addition of oxygen could help the formation of reactive oxygen species

(ROS), as proposed in the literature, but the experimental setting was chosen to assess the photocatalysts' intrinsic properties. [175]

The first step of the photocatalytic tests was called “dark,” in which the adsorption/desorption equilibrium of the target molecule on the photocatalyst was allowed for one hour without irradiation.

During the photocatalytic tests at constant time intervals (commonly 1 h), 3 mL suspension was withdrawn and immediately centrifuged (Thermo-Fisher Scientific SL 16R centrifuge, Thermo Electron LED GmbH, Osterode am Harz, Germany). The centrifugation was used to separate just the supernatant solution and avoid the noise induced by the powder during UV-Vis analysis. The remaining solution was analyzed on a UV-Vis-NIR spectrophotometer (Cary 5000, Varian Instruments, Mulgrave, Australia) in the 800 -190 nm wavelength range. The photocatalytic experiments were conducted in ambient condition.

Notably, pollutants concentration was chosen to guarantee the exploitation of the linear regime of the Lambert-Bear law (assessed for every pollutant with a calibration line), where the absorbance is proportional to the concentration of a specific functional group and, consequently, the presence of the whole molecule or its by-products.

The lamp used for this set of experiments was a plasma lamp (LIFI STA-40, LUXIM, Santa Clara, CA, USA). The lamp was correctly positioned from the reactor to simulate solar light (AM 1.5 G, 100 mW cm^{-2}). Consequently, the intensity obtained on the suspension was 1 SUN, i.e., ~1000 W m^{-2} in the visible range and ~22 Wm^{-2} in the UV range.

During the photocatalytic degradation of the two studied herbicides (namely, simazine and N-phenylurea), the photocatalytic degradation settings were adapted, and a UV lamp was also tested, to boost the photocatalytic degradation of such stable molecules. These compounds were considered particularly harmful, and the opportunity to abate them induced the choice of testing the photocatalytic processes in harsh conditions. In those cases, the chosen UV lamp (LC3, Hamamatsu Photonic, Hamamatsu, Japan.) was a medium-pressure Hg lamp providing a light intensity of 55 $mWcm^{-2}$.

6.1.2 Photocatalytic degradation of dyes.

This photocatalytic test set was performed in collaboration with the University of Salerno. In this set of photocatalytic experiments, the target molecules were cationic and anionic dyes; the chosen photocatalysts were the doped ones, and the

corresponding undoped sample was chosen as a benchmark. The experimental parameters were varied during these photocatalytic experiments to optimize the processes.[20][131]

The reactor used for this set of experiments was a cylindrical batch photoreactor in Pyrex with a total volume of 200 mL. The photocatalytic tests of the acid orange 7 (AO7) and crystal violet (CV) dyes were performed with 100 mL aqueous solution in a cylindrical Pyrex photoreactor operating in batch mode. In these cases, the "dark" condition was adapted to 2 hours because the adsorption/desorption equilibrium of the dye on the photocatalyst was considered particularly relevant. This hypothesis is supported by the presence of chromophores groups in dye molecules, and consequently, these pollutants could induce sensitizing effects on titania. [176] When illumination started under visible light (total duration: 180 min), ca. 3 mL suspensions were withdrawn every hour from the photoreactor, centrifuged, and analyzed by a UV-Vis spectrophotometer (Thermo Scientific Evolution 201, Thermofisher Italia, Monza).

A peculiarity of this experiment is that the airflow maintained inside the solution (Qair = 150 cm^3min^{-1} (STP)). The airflow was purged into the reactor through an air distributor system to guarantee optimal oxygen availability in the reaction medium. Also, in this case, the system's temperature was kept at 25–30°C.

By UV-Vis spectroscopy, the decolourization of the solution was monitored considering a dye concentration in the linear Lambert-Beer region. In this scenario, peculiars bands of the dyes were analyzed, and the kinetic data of the reaction were obtained.

In addition to UV-Vis spectroscopy, the supernatant's total organic carbon (TOC) was measured. The TOC value is a parameter correlated with mineralization because this process describes the degradation of a compound to its mineral components, i.e., carbon dioxide and water. [177] The TOC was evaluated from the analysis of CO_2 evolved during the post-process of the solution. After the reaction, the liquid sample received a catalytic oxidation at (680 °C), and the CO_2 produced in the gas phase was analyzed by a continuous system (Uras 14, ABB spa, Sesto San Giovanni, Milan, Italy).

For this set of photocatalytic tests, the light source was a white led light with an emission range in the visible light (440 and 600 nm peaks). LED strips were physically placed around the external body of the reactor to irradiate the whole volume of the solution.

6.2 Photocatalytic degradation of paracetamol

Paracetamol, also known as acetaminophen (APAP), has a solubility in water of 0.115 M (3) and we selected a concentration of 0.01 mM in an aqueous solution for the experiments. The paracetamol aqueous solution has natural pH of (pH = 5.7), at which the molecule is neutral (pK_a = 9. 5). [59]

The paracetamol solution absorption spectrum proposed in Figure 81 showed two bands at 243 nm and 194 nm. According to the literature, these bands can be assigned to the n → π* transition of the C=O group (243nm, black asterisk) and the π → π* transition of the aromatic ring (194 nm, red asterisk). [59]

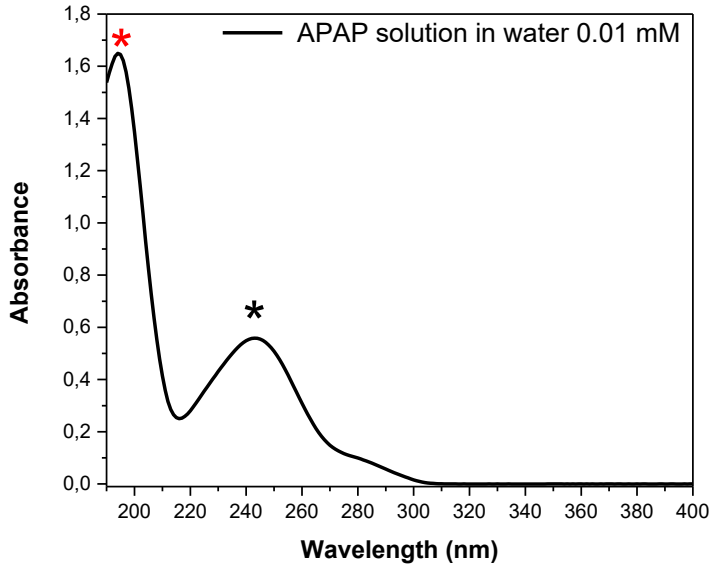

Figure 81. UV-Vis absorption spectrum of the 0.01 mM paracetamol aqueous solution. Absorption bands can be assigned to the n → π* transition of the C=O group (black asterisk) and the π → π* transition of the aromatic ring (red asterisk). [59]

As described in the previous paragraph, the UV-Vis spectra provided information about the degradation of the paracetamol molecules.

The band at 243 nm evolution with time was considered as a reference for evaluating the amount of paracetamol molecules available in the solution. Furthermore, a kinetic study of the degradation rate was proposed to compare the photocatalytic efficiency of the photocatalysts.

Figure 82 (panels a, c, and d) reports the results obtained during the photocatalytic tests performed with a photocatalyst (AB, ABR, and the benchmark P25) concentration of 1 g L^{-1}, whereas the kinetic behavior of the photocatalytic reactions was proposed on the right (Figure 82).

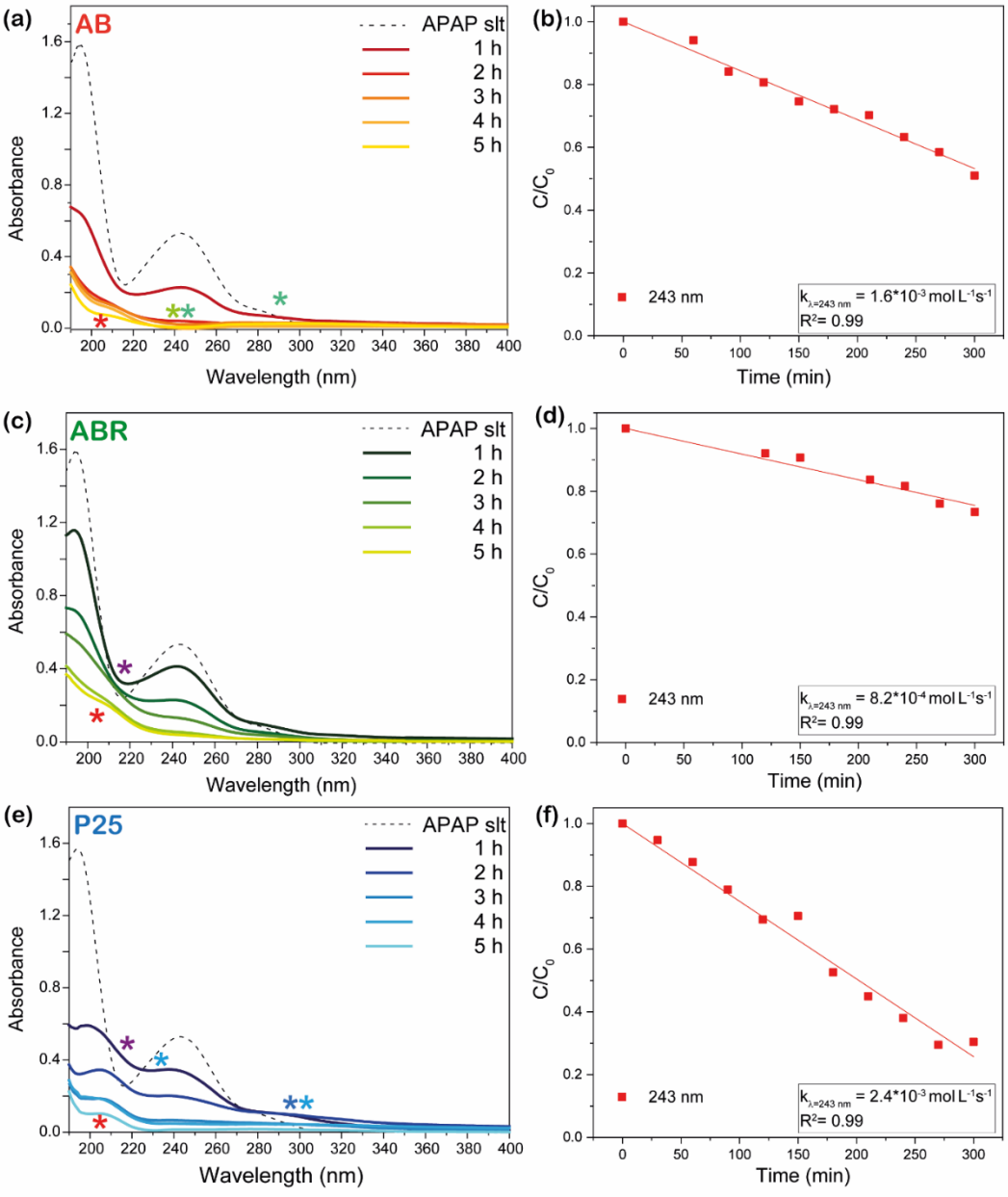

Kinetic data were obtained by photocatalytic tests performed with a photocatalyst concentration of 0.15g L^{-1} because the by-products' presence

Figure 82 UV-Vis spectra of the starting 0.01 mM paracetamol solution (APAP slt, dashed line) and of the supernatant aliquots withdrawn after 1, 2, 3, 4, and 5 h solar illumination with the 1.0 g L^{-1} of AB (a), ABR (b) and P25 (c) powders. The colored asterisks indicate bands ascribable to some possible by-products.

interfered with the band at 243 nm, hampering monitoring during the photocatalytic tests.

According to Figure 82, complete photocatalytic degradation of paracetamol molecules was achieved in 300 min with solar simulated light.

Colored asterisks were placed in correspondence with peculiar bands associated with the literature with typical by-products of paracetamol degradation.

By photocatalytic degradation of paracetamol with the AB sample, bands ascribable to hydroxylated compounds to 4-aminophenol were not formed at the beginning of the reaction.

For this reason, the path suggested by Moctezuma et al. l[108] is proposed, in which the hydroxyl radicals interact with the substituent of the aromatic ring and, in some cases, lead to the formation of hydroquinone (band at 290 nm). With the ongoing reaction (after 3 h irradiation), a peculiar inflection of curves at 240 nm was noticed and assigned to the presence of hydroquinone, nitrophenol, and resorcinol (light- and dark-green asterisks, respectively). Hydroquinone was the last by-product observed before ring opening and small carboxylic acid formation.

Nitrophenol's presence after 3 h irradiation suggested the presence of an aliquot of by-products showing the nitrogen-containing substituent of the aromatic ring. These molecules were considered as intermediate by-products. On the other hand, after 3h irradiation, another portion of molecules had already reached the hydroquinone molecule considered an advanced by-product. The coexistence of the by-products is supported by literature because the oxidation of p-nitrophenol may undergo two main paths i) hydroxylation in ortho-position to OH group in phenol with eventual formation of nitrocatechol [178] and ii) hydroxylation in para-position to OH group with subsequent NO_2 elimination to form hydroquinone. [108][179]

The last possibility is the dominant reaction; hence, hydroquinone is supposed to be a by-product of nitrophenol photocatalytic oxidation. [180] Hydroquinone during photocatalytic processes was probably mainly oxidized to 1,2,4-trihydroxy benzene, but no evidence of this compound was observed by UV-Vis spectroscopy. According to the literature, most of the ring cleavage comes from the 1,2,4-benzene-triol compound, and the subsequent carbon chains were degraded to smaller moieties. [181] The final species were likely acetic and formic acid, according to the band at 205 nm. [59]

By photocatalytic degradation of paracetamol with the ABR sample, the band at 215 nm (violet asterisk) is associated with hydroxylated compounds (i.e., 1,2,4-benzenetriol).[108] This unique indication of the by-product's presence suggested the loss of the majority of the paracetamol molecules of the –NH–CO group. According to the literature, the photocatalytic oxidation of 1,2,4-benzene-triol degradation proceeds by electron transfer, as shown in Figure 83, to give a radical cation that undergoes subsequent oxidation with ring cleavage to produce low molecular weight acids (red asterisk). The proposed degradation mechanism (Figure 83) is proposed in the literature where TiO_2 /UV light systems were adopted for photocatalytic degradation of paracetamol. [108]

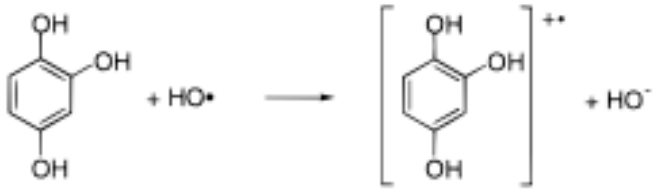

Figure 83. 1,2,4-trihydroxy benzene degradation proceeds by electron transfer to give a radical cation. [181]

ABR sample induced the formation of the 1,2,4-trihydroxybenzene according to the experimental evidences. On the other hand AB sample induced the formation of hydroquinone molecules which, according to literature, should undergo hydroxylic attack and reach the 1,2,4-trihydroxybenzene structure before ring opening. [181]. Still, the time requested to ring opening and the final small carboxylic acids achievement differed for the two samples, with the AB sample inducing the ring cleavage after 2 h irradiation.

Figure 82 panel e shows the photocatalytic degradation experiment performed with P25 commercial powder used as a benchmark. According to the UV-Vis spectra, a drastic decrease of the prominent paracetamol bands at 243 nm occurred after 1 h irradiation. The formation of by-products occurred immediately, and two bands at ca. 230 nm and 300 nm (light blue asterisks) were evidenced. These two bands were ascribed to the formation of 4-aminophenol, which can be further oxidized to nitrophenol (blue asterisk) and 1,2,4-trihydroxy benzene (purple asterisks) as reported in the literature. [108] After 240 mi, the band at 205 nm (red asterisk) was observed even with the P25 sample.

Figure 84 shows the possible photocatalytic degradation mechanisms of paracetamol obtained by the whole set of samples. In the blue box the by-products evidenced by UV-Vis spectroscopy are proposed. In contrast, the yellow boxes

highlighted the presence of the same by-products achieved with different photocatalytic degradation mechanisms.

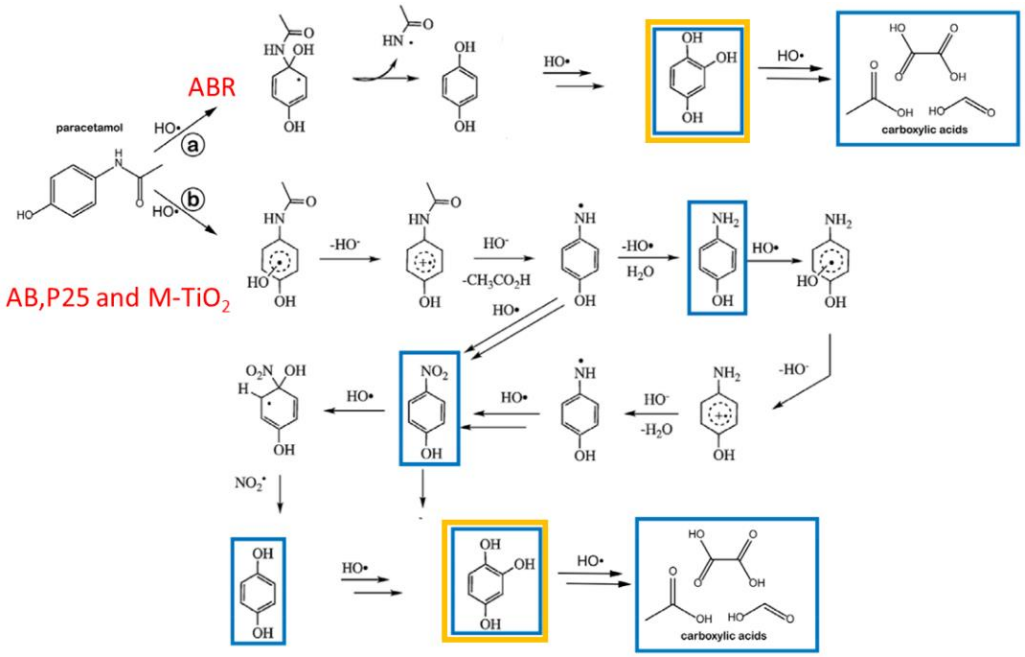

Figure 84. Paracetamol degradation pathways according to the literature, adapted from refs. [108], [182] Compounds in the boxes correspond to possible by-products identified by UV-Vis spectroscopy during the photocatalytic experiments. [59]

Once assessed the influence of different polymorphic structures on the photocatalytic degradation of paracetamol another photocatalyst was chosen to understand the effects of morphological properties. In this case the M-TiO_2 sample was chosen which is a material showing anatase as unique polymorphic structure but the morphological properties, i.e., mesoporosity, were tuned with photocatalytic properties optimization purposes. [86]

Figure 85 (right) shows the UV-Vis spectra collected during the photocatalytic degradation of paracetamol obtained with the M-TiO_2 sample.

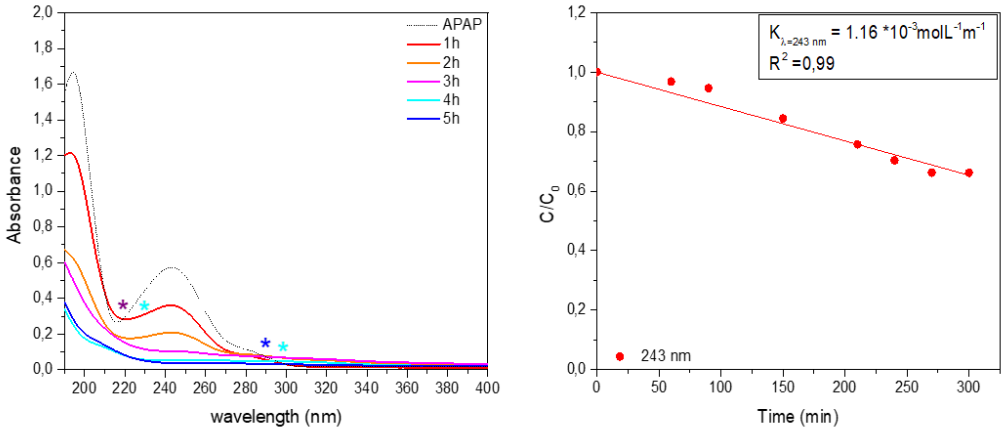

Figure 85. UV-Vis spectra of paracetamol degradation under 1 SUN with 1 g L^{-1} M-TiO_2 (left) and kinetic analysis of the photocatalytic degradation with 0.15 g L^{-1} Mes-TiO_2 as obtained by following the intensity of the band at 243 nm (right).

The degradation mechanism observed during the M-TiO_2 photocatalytic test was similar to P25 photocatalytic test, with 4-aminophenol (light blue asterisks) formation and consequent oxidation to nitrophenol (blue asterisk) and finally 1,2,4-trihydroxybenzene (purple asterisks). The degradation of the paracetamol molecules was achieved after 300 min irradiation with the band at 205 nm associated with carboxylic acids, evidenced even in this case as demonstrated by experimental tests.

The UV-Vis spectroscopy spectra allowed the comparison of the photocatalytic properties of the sample, and the hypothesis of degradation mechanisms was proposed. However, the kinetic data obtained during the photocatalytic tests performed with 0.15 g L^{-1} photocatalyst concentration offered the opportunity to compare the photocatalytic efficiency. Therefore, in Table 18, the kinetic constants were summarized for the four samples AB, ABR, P25, and M-TiO_2.

Table 18. Kinetic constant and fitting parameters obtained during the photocatalytic degradation of paracetamol with 0.15 g L^{-1} concentration of the photocatalysts.

Sample	$K_{\lambda=243nm}$ [10^{-3}mol L^{-1}min]	R^2
AB	1.60	0.99
ABR	0.82	0.99
P25	2.39	0.99
M-TiO_2	1.16	0.99

The samples AB and M-TiO_2 showed a kinetic constant of the photocatalytic degradation of paracetamol of the same order of magnitude as the P25 sample, which reached the highest kinetic constant value with the experimental settings under examination.

The reaction order is another information obtained from the photocatalytic tests performed at 0.15 g L^{-1}. Kinetic data were fitted with a line when plotted with C/C_0 against time. This trend is typical of zero-order kinetic reactions.

As Cubbage et al. proposed, the degradation of molecules during a photocatalytic reaction can be due to the pollutant's adsorption on the photocatalyst's surface or not.[183] The first mechanism can be described as a Langmuir–Hinshelwood (LH) mechanism, while Eley can describe the second mechanism–Rideal (ER) model based on a less rigorous binding event. The LH mechanism is commonly referred to, at low pollutant concentration, as a pseudo-first-order reaction. [183][184] For this reason, kinetic data could be used to explain some aspects of the photocatalytic degradation processes.

Overall, the photocatalytic degradation of paracetamol obtained by different samples can be attributed to the peculiar intrinsic properties of the materials. The presence of heterojunctions in the case of AB and P25 samples played a role. AB sample's photocatalytic properties were explained by the occurrence of efficient anatase/brookite heterojunctions, which have been shown to favor the separation of photogenerated e^-/h+ pairs. [25] The same kind of heterojunction was observed in the ABR sample, but a larger NPs size and a smaller surface area likely decreased its photocatalytic properties under solar light. On the other hand, the photocatalytic properties of P25 could be correlated with heterojunction between anatase/rutile, which can stabilize photogenerated charge carriers. [185]

The M_TiO_2 sample showed just the anatase polymorphic structure; hence, the photocatalytic properties should be researched elsewhere. This material exhibited good photocatalytic properties due to high SSA and organized intraparticle and interparticle mesoporosity, allowing paracetamol interdiffusion within pores. The M_TiO_2 photocatalyst showed pores diameter exceeding the molecular size of paracetamol (ca. 1.0 × 0.25 nm [186]), indicating that the whole available surface area should be accessible to paracetamol and its by-products, not affecting the reaction kinetics. [59]

6.3 Photocatalytic degradation of Simazine

The photocatalytic degradation of simazine was studied with the AB and the whole set of iron-doped AB photocatalysts. The experimental settings proposed for these photocatalytic experiments were based on a simazine concentration of 0.0175 mM and two different irradiation sources:

- Solar simulated lamp
- UV lamp

The solubility limit of simazine reported in the literature at room temperature and the atmospheric pressure is 0.0307 mM. [187] A lower concentration was chosen for photocatalytic experiments to overcome the low stability of the simazine solution in water.

Figure 86 shows the spectrum of the simazine solution used during the photocatalytic experiments. The spectrum of simazine shows two bands at 222 and 265 nm. These bands can be namely assigned to $\pi \rightarrow \pi^*$ (red asterisk) and $n \rightarrow \pi^*$ (black asterisk) electronic transitions. [188]

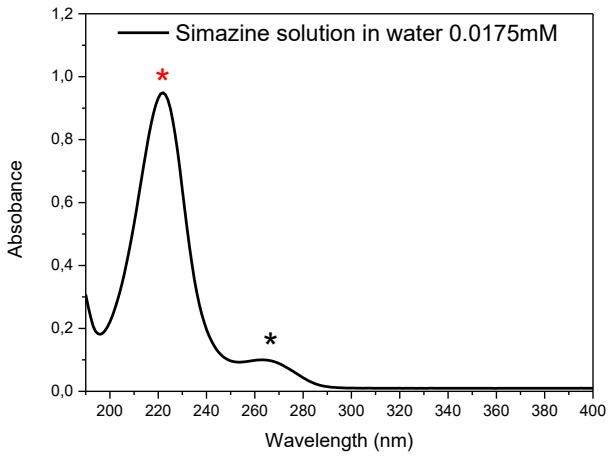

Figure 86. UV-Vis spectra of 0.0175mM simazine solution. The peculiar bands at 222 and 265 nm can be assigned to $\pi \rightarrow \pi^*$ (red asterisk) and $n \rightarrow \pi^*$ (black asterisk) electronic transitions [188]

Figure 87 reports the spectra obtained after 5 h under 1 SUN in the presence of the 4 studied powders. The photocatalytic experimental settings were based on a photocatalyst concentration of 1 g L^{-1} and simazine concentration of 0.0175mM in water.

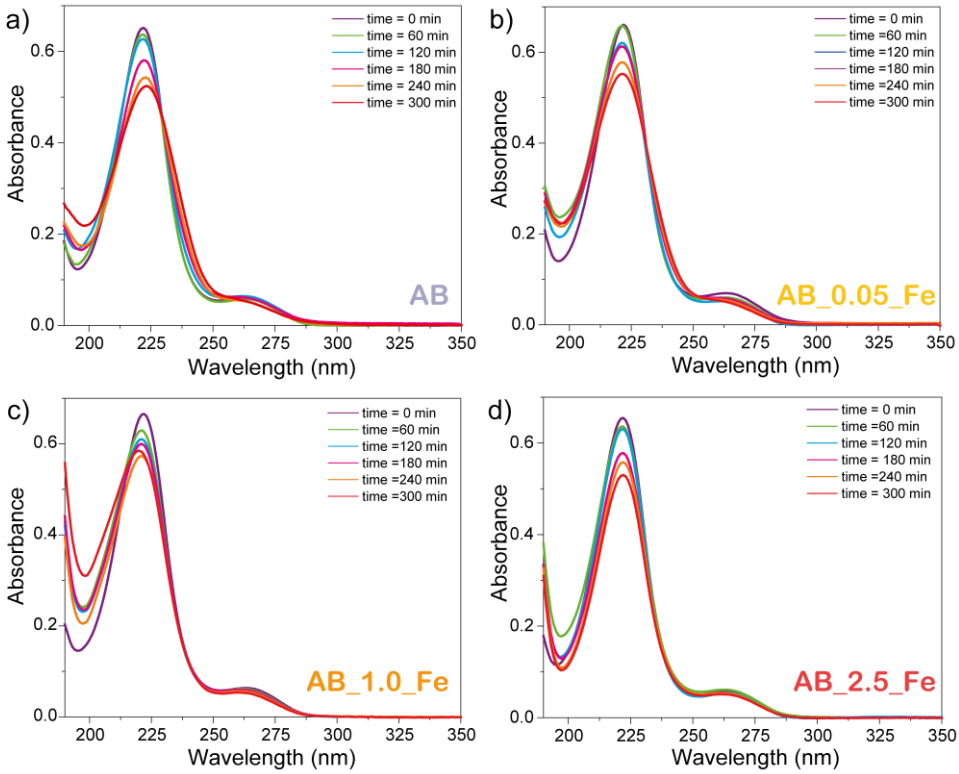

Figure 87. Absorption spectra obtained during photocatalytic tests with AB sample (a), AB_0.05 Fe (b), AB_1Fe (c), and AB_2.5Fe (d) under a simulated solar light with photocatalyst concentration of 1 g L^{-1} and simazine concentration of 0.0175 mM in water. [31]

The results showed a total simazine degradation of ca. 20 % with the undoped AB sample, testifying that this material can effectively exploit solar light, likely due to its DR-UV-Vis spectroscopy absorption spectrum showing the Urbach tail, as discussed in paragraph 4.2. Furthermore, the band at 222 nm showed an intensity decrease between 15 and 20% for the whole set of doped samples. As shown in other experiments, these results indicated the possibility of exploiting the solar spectrum with these samples, as well. [27].

During the photocatalytic tests under 1 SUN, no other bands were formed, and consequently, the overall simazine degradation was assessed, but the by-products formation and consequent degradation mechanism proposal were not possible.

Simazine is a stable molecule, according to the literature, and the reason for this high stability is attributed to the energy gap between its frontiers orbitals. [188] For this reason, mineralization was difficult to achieve by photocatalytic degradation with solar-simulated light. The possibility to boost the samples'

photocatalytic properties by exploiting the whole range of absorption of the photocatalysts induced the use of another UV-Lamp.

Figure 88 shows the UV-Vis spectra obtained during the photocatalytic experiments with the UV lamp, maintaining the previously detailed experimental settings.

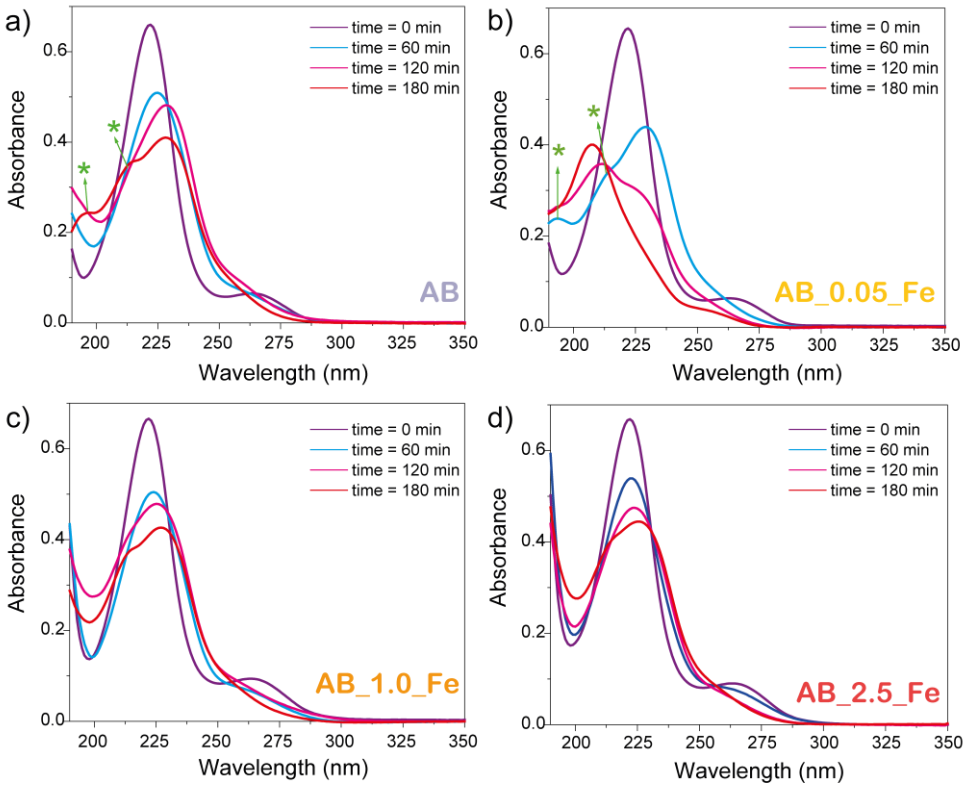

Figure 88. Absorption spectra obtained during photocatalytic tests with AB sample (a), AB_0.05 Fe (b), AB_1Fe (c), and AB_2.5Fe (d) under UV lamp with a photocatalyst concentration of 1g L^{-1} and simazine concentration of 0.0175 mM in water. [31]

The two most active samples were AB and AB_0.05_Fe. These samples led to the formation of new bands ascribed to by-products during the photocatalytic experiments under UV irradiation. The bands at 213 and 193 nm (green asterisks) were assigned in the literature to cyanuric acid. [189] Cyanuric acid is a non-toxic parent molecule of simazine, and it is the main by-product obtained with AB and AB_0.05_Fe samples.

According to the literature, commonly, simazine molecules undergo dealkylation and dechlorination processes before cyanuric acid formation, as summarized in Figure 89. [190] Evidence of these steps includes a blue shift of the band at 222 nm and the disappearance of the band at 265 nm band during the

dealkylation mechanism. In contrast, dechlorination induces a red shift of the 222 nm band in the water solution. [190]

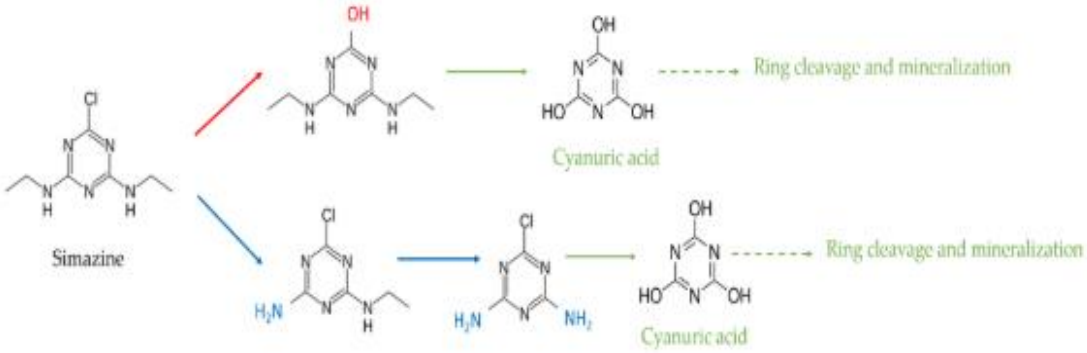

Figure 89. Oxidative degradation pathways of simazine obtained from ref [31].

Evidence of these band shifts was observed for the whole set of samples during the photocatalytic degradation of simazine under UV light. The alteration of simazine's molecules structure proved the degradation induced by these photocatalysts.

The best results were obtained with the AB and AB_0.05_Fe photocatalysts: with these samples, cyanuric acid formation occurred after 60 min reaction. Furthermore, also cyanuric acid molecules (peculiar absorption band intense band at 213 nm and a shoulder at 193 nm)[189] underwent photocatalytic degradation and probably a ring-opening process leading to further by-product formation.

The complete mineralization of simazine was not obtained with this set of samples, even under UV light. On the other hand, detoxification was achieved, i.e., by dechlorination processes, as long as we get lesser toxic molecules (namely, cyanuric acid) during the photocatalytic degradation of simazine. According to the literature, this result shall be considered an important achievement, considering the extremely high stability of the simazine molecule.[191][192]

For this set of photocatalytic tests under UV light, the M-TiO_2 sample was chosen as a benchmark for evaluating the photocatalytic properties of AB and Fe-doped AB samples. Figure 90 shows the UV-Visible spectra obtained during the photocatalytic degradation with the M-TiO_2 sample under UV light. All the experimental parameters adopted for experiments reported in Figure 88 were kept unvaried.

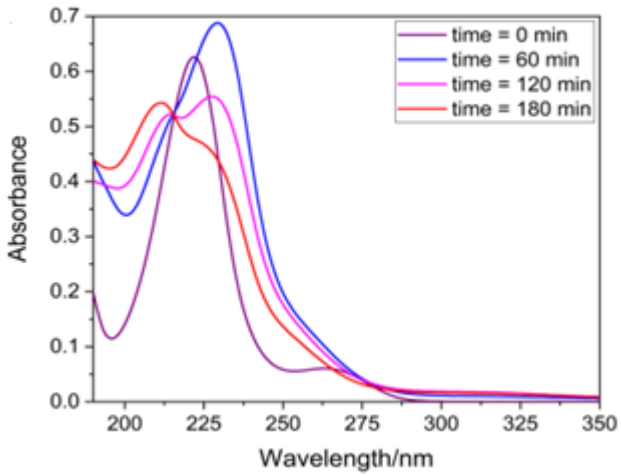

Figure 90. Absorption spectra obtained during the photocatalytic degradation of simazine with 1 g L^{-1} M-TiO_2 sample and UV-light. Simazine solution concentration was 0.0175 mM. [31]

With the M-TiO_2 sample, dechlorination occurred, as shown by a blue shift under 1 h irradiation. This attack on the simazine molecule probably led to the formation of the 4,6-diamino-2-hydroxy-1,3,5-triazine compound (main band at 229 nm [193]). This molecule was attacked and transformed into a more hydroxylated product (isosbestic point). However, the bands of cyanuric acid (at 213 and 193 nm) were not detected in the spectra. For this reason, likely the photocatalytic degradation with M-TiO_2 under UV light proceeded through another degradation mechanism, as compared to AB and doped AB samples.

6.4 Photocatalytic degradation of N-phenylurea

The photocatalytic degradation of the herbicide N-phenylurea (NPU) was performed with two irradiation sources:

- Solar simulated lamp
- UV lamp

In both cases, the photocatalytic properties of the undoped samples were assessed using the P25 powder as a benchmark. The photocatalysts selected for NPU photocatalytic degradation were:

- AB and ABR
- M-TiO_2
- RM-TiO_2

The photocatalyst concentration chosen was 1 g L^{-1}, while the N-Phenylurea solution concentration was 0.01 mM. The solubility of NPU at room temperature reported in the literature is 0.073 mM. Even in this case, for the photocatalytic tests were performed, with a concentration of pollutant, lower than the solubility limit of NPU in water. The choice was induced by the necessity to guarantee the stability of the solution during the photocatalytic tests.

Figure 88 reported the absorption spectrum of the solution used during the photocatalytic tests. The spectrum showed two main bands associated with substituted benzene rings at 199 and 235 nm. Another weak band at 270 nm can be appreciated in Figure 91.[194][27]

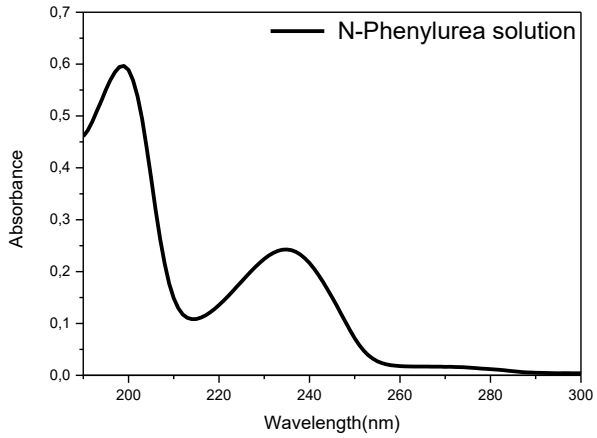

Figure 91. UV-Vis spectrum of 0.01mM NPU solution in water.

Figure 92 shows the UV-Vis spectra were obtained after 240 min photocatalytic degradation of NPU under 1 SUN.

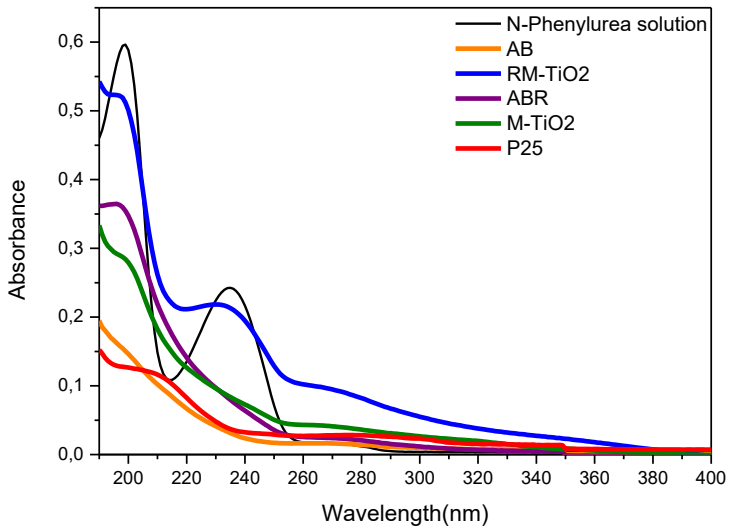

Figure 92. Solar simulated lamp photocatalytic degradation of NPU tests with AB (orange line), ABR (violet line), M-TiO_2 (blue line), RM-TiO_2 (green line) samples, and the benchmark P25 (red line) after 4h of illumination.

The NPU degradation % under 1 SUN followed the order AB ≅ P25 > M-TiO_2 > ABR > RM-TiO_2. The AB sample showed the best photocatalytic properties towards N-Phenylurea degradation under 1 SUN. The benchmark powder P25 reached similar photocatalytic degradation to AB photocatalyst.

The AB sample photocatalytic properties were attributed to the intrinsic properties of the materials described in paragraph 4.3, where the high SSA, the presence of anatase/brookite heterojunctions, and the presence of the Urbach tail were described. The photocatalytic efficiency of the AB sample was due to a combination of these aspects. The photocatalytic properties of the RM-TiO_2 sample were not boosted by the presence of brookite and anatase probably because of low content of brookite (8 %). Furthermore, a SSA comparable with P25 did not promote the photocatalytic degradation on N-phenylurea, probably for morphological reasons (aggregation of NPs) which inhibited the effective available surface of the material.

The central hypothesis regarding photocatalyst-NPU interaction was the presence of Van der Waals-type secondary bonding with the materials. These secondary interactions are the main explanation proposed, as the pH_{IEP}

measurement showed scattered results among different samples. The M-TiO_2 sample showed a very low pH_{IEP} (2.37), lower than the AB sample (ca. 5). Furthermore, the solution pH was 5.7 in the experimental condition, suggesting that AB NPs should be almost neutral, while the M-TiO_2 ones are negatively charged. These reasons were the base for hypothesizing that the interaction between particles and pollutant molecules should be researched elsewhere.

AB and M-TiO_2 samples had higher specific surface areas, which seemed to be the most crucial parameter in the photocatalytic degradation of NPU experiments. These results would not explain the comparable effectiveness of ABR and Mes-TiO_2 samples. The possible explanation is evidenced by Figure 93, where the position of the polymorphs is proposed concerning LOMO and HUMO orbitals of NPU.[27]

Brookite seems to have the best alignment of bands due to the superimposition with the LUMO orbitals of NPU. This situation might promote NPU molecules reduction of the NPU molecules. [27] For this reason, the hypothesis of a brookite-rich surface in the AB and ABR samples was inferred. This supposition was supported by experimental evidence observed in paragraph 4.3.2. [27]

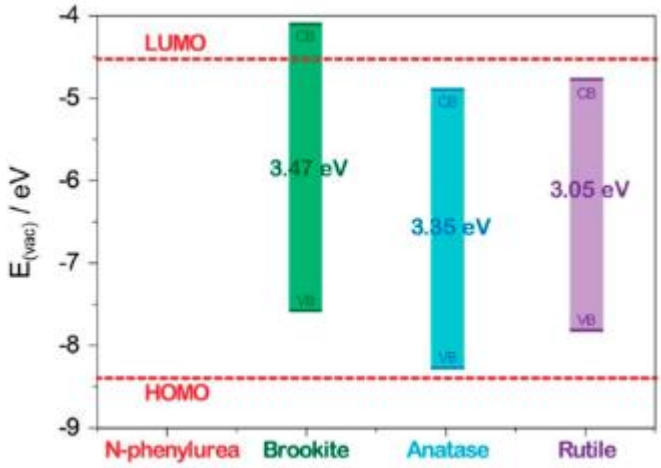

Figure 93. Position the calculated VB and CB of brookite, anatase, and rutile TiO_2 polymorphs[19]. The calculated HOMO and LUMO values of NPU [195] are reported as dotted lines.

Overall, the photocatalytic degradation results demonstrated that our samples were active in the photocatalytic degradation of NPU under solar simulated solar light.Figure 94 shows the UV-Vis spectra obtained after 240 min photocatalytic degradation of NPU under UV-light irradiation.

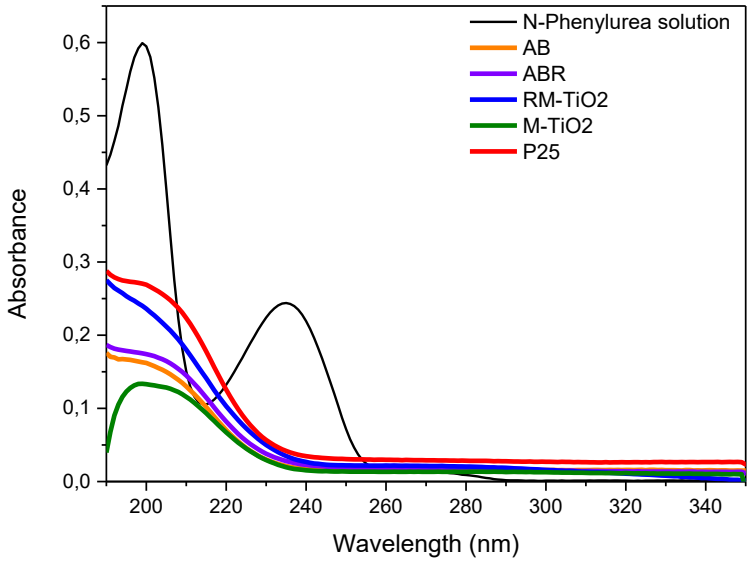

Figure 94. UV light photocatalytic degradation of NPU tests with AB (orange line), ABR (violet line), M-TiO_2 (blue line), RM-TiO_2 (green line) samples, and the benchmark P25 (red line) after 4h of irradiation.

According to the spectra shown in Figure 94, the samples obtained comparable photocatalytic degradation results. The marked decrease of the band at 235 nm was attributed to the degradation process of the -$NHCONH_2$ functional group. Simultaneously, the intensity of the band at 213 nm was observed. This band was associated in the literature with hydroxylated benzene rings. [108]

The hydroxylated benzene ring's presence provided insight into the degradation mechanism involving the occurrence of hydroxyl radicals attack to the ring already seen in paragraph 6.2 with ABR samples during the photocatalytic degradation of paracetamol.

Under UV light irradiation, the samples showed excellent photocatalytic activity. The better exploitation of incident radiation explained the improvement in the photocatalytic degradation of NPU. The increased light absorption, associated with all the samples according to their Eg, overcame the other morphological or intrinsic differences among samples.

6.5 Photocatalytic degradation of Acid Orange 7 (AO7)

The photocatalytic degradation of Acid orange 7 (AO7) was performed with the experimental settings summarized in Table 19. The photocatalysts chosen for this photocatalytic test were the iron-doped M-TiO_2 samples with undoped M-TiO_2 used as the benchmark. [196]

Table 19. Experimental settings of photocatalytic degradation of AO7 performed with M-TiO_2 samples.

Experimental parameters	**Starting conditions**	**Experimental parameters variations**	**Effective variations**
Light source	White LED 440 and 600 nm peaks	No variations	/
Photocatalyst concentration	1.5 g L^{-1}	Concentration variation of the most active sample M-TiO_2_2.5_Fe	0.75 g L^{-1} 3.0 g L^{-1} 6.0 g L^{-1}
Dye concentration	0.0285 mM (10 mg L^{-1})	Concentration variation in presence of the most active sample M-TiO_2_2.5_Fe	0.0570 mM (20 mg L^{-1}) 0.0142 mM (5 mg L^{-1})
Air flowing	150 cm^3min^{-1}	No variations	/

Several parameters were tested during this set of experiments, and two primary outcomes were obtained from the photocatalytic tests: discoloration and mineralization of the dye (AO7) molecules. The discoloration test gave information about the integrity of the dye molecules during the photocatalytic tests. Still, the main result was mineralization related to the total organic carbon (TOC) parameter.

Combining two parameters offers a deep understanding of the effectiveness of the photocatalytic degradation of AO7. In Figure 95, the data concerning the photocatalytic discoloration test with the whole set of samples are reported. The discoloration efficiency can be summarized in the following order: M-TiO_2_2.5_Fe > M-TiO_2_1_Fe > M-TiO_2_3.5_Fe > M-TiO_2. After 180 min under white LED

irradiation, the best photocatalyst in discoloration efficiency, M-TiO_2_2.5_F, led to the discoloration of 53 % AO7.

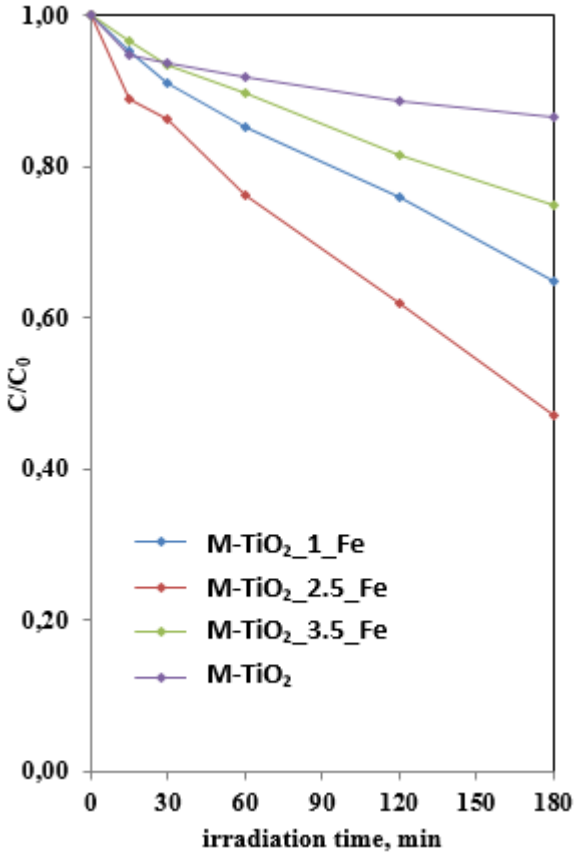

Figure 95. Results of the photocatalytic discoloration tests of M-TiO_2 (violet line), M-TiO_2_1_Fe (blue line), M-TiO_2_2.5_Fe (red line), M-TiO_2_3.5_Fe (green line) performed in starting conditions(Table 19. Experimental settings of photocatalytic degradation of AO7 performed with M-TiO2 samples. [196]

Results reported in Figure 95 led to the conclusion that iron doping influenced photocatalytic discoloration efficiency because higher discoloration percentage was obtained with iron-doped samples than with undoped TiO_2. However, the effects of iron doping are not straightforward because the nominal weight percentage of iron was not strictly correlated to photocatalytic discoloration increasing. [196]

The primary explanation for the discoloration efficiency of the iron-doped samples is the partial replacement of Ti^{4+} ions by Fe^{3+} ions in the lattice. This substitutional solution obtained in the material's first layer alters titania's electronic

properties. The main effect is the promotion of charge separation and stabilization, as reported in the literature. [197]

However, the electronic properties are not the only physico-chemical variations induced by iron doping. For example, iron ions inclusion inside the lattice can cause crystalline defects, which can promote midgap levels formation inside the Eg that can have the drawback of inducing the recombination of charge carriers depending on the position. [198] Furthermore, when doping is excessive, iron species segregation on the surface can take place, as described in paragraph 5.1.2 Such surface Fe_2O_3 or oxi/hydroxyde clusters altered the surface charge and promoted the anionic dye's adsorption. The anionic dye AO7 could interact with the protonated groups on the surface of the photocatalyst through the negative sulfonate group. As the pH_{IEP} value was higher for M-TiO_2_3.5_Fe, the relative abundance of positively charged sites on the surface at the natural pH of the AO7 solution was the highest among different samples. For this reason, a high amount of dye adsorbed on the surface of the M-TiO_2_3.5_Fe photocatalyst induces a decrease in the number of photons reaching the material's surface. In this case, no sensitizing effect of the dye was observed as the photocatalytic properties were also tested with other colourless molecule (phenol). [196]

Figure 96 shows the percentage of mineralization obtained, for the whole set of samples, by photocatalytic test performed in starting conditions (Table 19). The same photocatalytic experiments provided the discoloration results summarized in Figure 95.

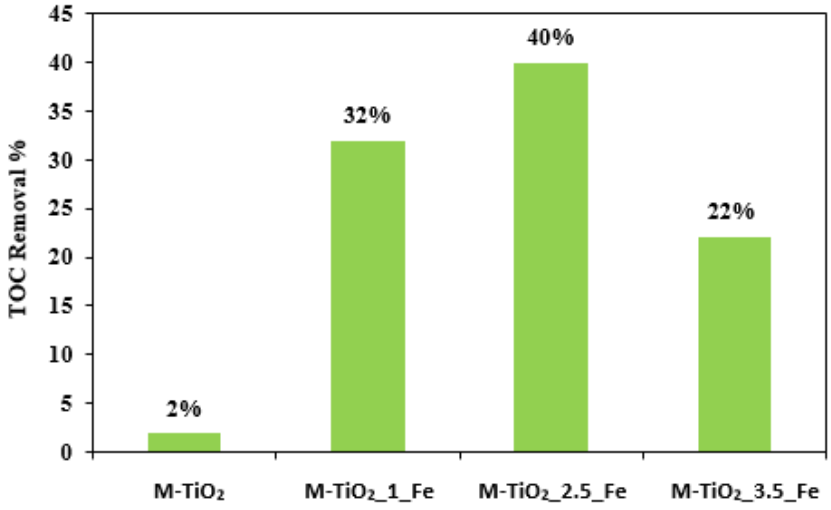

Figure 96. TOC Removal (%) from the AO7 aqueous solution after 180 min of visible light irradiation using M-TiO_2_1_Fe, M-TiO_2_2.5_Fe, M-TiO_2_3.5_Fe and undoped M-TiO_2 photocatalysts. [196].

The data regarding the mineralization showed the same trend obtained with photocatalytic discoloration of the whole set of samples. The best percentage of AO7 mineralization was obtained with the M-TiO2_2.5_Fe sample.

Figure 97 shows the photocatalytic tests' kinetic results in starting conditions (Table 19). The whole set of samples followed a pseudo-first-order kinetic during the photocatalytic tests according to the linearity of data.

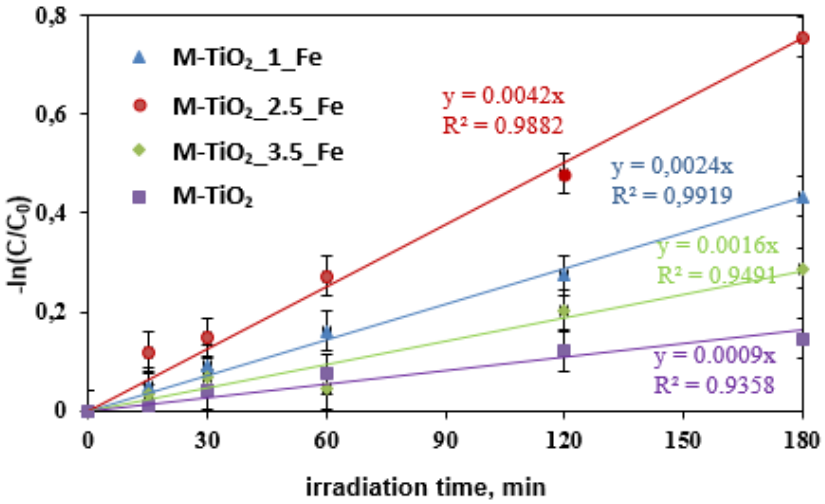

Figure 97. Kinetic results of the photocatalytic tests of M-TiO_2 (violet line), M-TiO_2_1_Fe (blue line), M-TiO_2_2.5_Fe (red line), M-TiO_2_3.5_Fe (green line) performed in starting conditions Table 19. [196]

The kinetic data in Figure 97 highlighted the same trend of photocatalytic efficiency shown in the previous figures with the order of photocatalytic properties M-TiO_2_2.5_Fe > M-TiO_2_1_Fe > M-TiO_2_3.5_Fe > M-TiO_2.

However, these results gave insight into the photocatalytic mechanisms involved in discoloration and mineralization processes. The photocatalytic discoloration and mineralization of AO7 had a pseudo-first-order kinetic; in the case of low concentrations of pollutants, this reaction kinetics can be described by the Langmuir-Hinshelwood model. [199] For this model application, the adsorption of the pollutant on the surface is requested, as already proposed in paragraph 6.2. [183][184].

Experimental evidence of AO7 adsorption on the surface of the photocatalysts was obtained after the dark conditions. After 2h of photocatalyst dispersion in solution was noticed, on the surface of the photocatalyst, an increased amount of adsorbed AO7 depending on the iron content. These amounts of adsorbed AO7 were correlated with better photocatalytic properties. The exception was the M-

TiO_2_3.5_Fe sample, probably because an excessive amount of dye adsorbed on the surface inhibited the possibility for photons to reach the surface of the material and promote the electron/hole separation.

After the first set of photocatalytic tests to understand the best photocatalyst among the selected samples, two essential parameters of photocatalytic processes, namely AO7 and photocatalyst concentration, were investigated.

Figure 98 shows the photocatalytic discoloration results of the experiments performed to understand the optimized photocatalyst concentration. The selected sample M-TiO_2_2.5_Fe concentration influence on photocatalytic properties was assessed with experimental parameters reported in Table 19. The experimental conditions were kept unaltered compared to starting condition (Table 19) except for photocatalyst concentration.

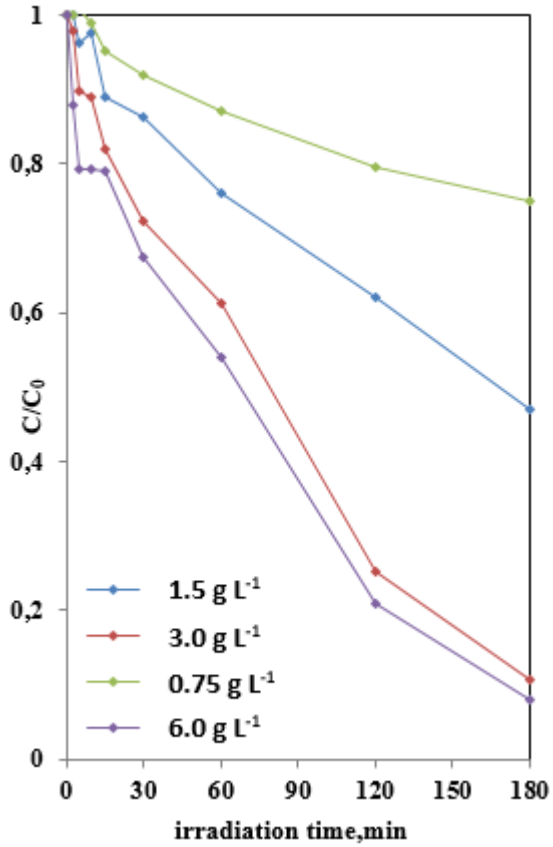

Figure 98. Discoloration results of the photocatalytic tests performed with the most efficient photocatalyst M-TiO_2_2.5_Fe with different sample concentrations. 6 g L^{-1} (violet line), 1.5 g L^{-1} (blue line), 3 g L^{-1} (red line) and 0.75 g L^{-1} (green line). [20]

The main result of the photocatalytic discoloration test performed with different concentrations of M-TiO_2_2.5_Fe was the similar efficiency with photocatalyst concentration of 6 and 3 gL^{-1}. The optimized concentration was, hence, 3 gL^{-1} because it guaranteed good results without photocatalyst loss.

Once the photocatalyst concentration was optimized, the optimal AO7 was investigated at different dye concentrations.

Figure 99 reported the discoloration results of the new experiments performed with 3 g L^{-1} of M-TiO_2_2.5_Fe sample and other parameters already presented as starting conditions in Table 19 but with different dye concentrations.

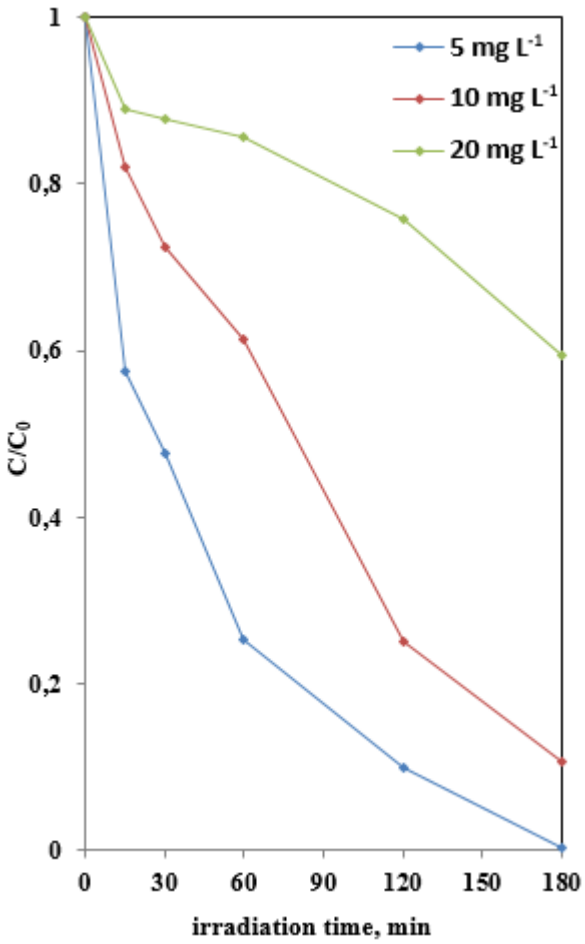

Figure 99. Discoloration results of the photocatalytic tests performed with the most efficient photocatalyst M-TiO_2_2.5_Fe with different AO7 concentrations.:5 mg L^{-1} (blue line), 10 mg L^{-1} (red line) and 20 mg L^{-1} (green line). [20]

This final group of experiments showed that by decreasing the pollutant amount, we faced a total discoloration of the solution in 180 minutes of white LED

irradiation. This evidence confirmed the hypothesis that the dye could inhibit the possibility for photons to reach the surface of the photocatalyst and hence reduce their photocatalytic properties [20]

Overall, these two final experiments offered a better understanding of the system described in this paragraph. Furthermore, the highest discoloration kinetics already reported in the literature was lower than the best result obtained with optimized experimental settings. [20] Han and coworkers optimized their experiments using a dosage equal to 2.5 g L^{-1} of Fe-doped TiO_2 with 25 mg L^{-1} AO7 concentration. [20][200]

By optimizing experimental parameters, they obtained a kinetic constant of discoloration of 1.6*10-3min^{-1} with visible light irradiation. The optimized experiments proposed in this paragraph provided a kinetic constant of 11.9*10^{-3} min^{-1}, one order of magnitude higher than the Han et al. experiment's best result. [20]

6.6 Photocatalytic degradation of Crystal Violet (CV)

The photocatalytic tests performed to study the discoloration and mineralization of the cationic dye crystal violet (CV) are summarized in **Table 20**. The photocatalysts chosen for these photocatalytic tests were the iron-doped RM-TiO_2 samples with undoped RM-TiO_2 used as a benchmark. [131]

Table 20. Experimental conditions adopted during the photocatalytic discoloration and mineralization tests of CV with RM-TiO_2 set of samples.

Experimental parameters	**Starting experimental conditions**	**Experimental parameters variations**	**Effective variations**
Light source	White LED 440 and 600 nm peaks	No variations	/
Photocatalyst concentration	3 g L^{-1}	No variations	/
Dye concentration	0.0285 mM (10 mg L^{-1})	No variations	/
Air inflation	150 cm^3min^{-1}	Variation in concentration of the most active sample RM-TiO_2 2.5 Fe	N_2 flow

Figure 100 shows data obtained during the photocatalytic discoloration tests performed in the starting experimental conditions (**Table 20**). The whole set of samples led to a 96% discoloration within 180 min except for the RM-TiO_2_3.5_Fe sample (75%) under visible light irradiation (white LED).

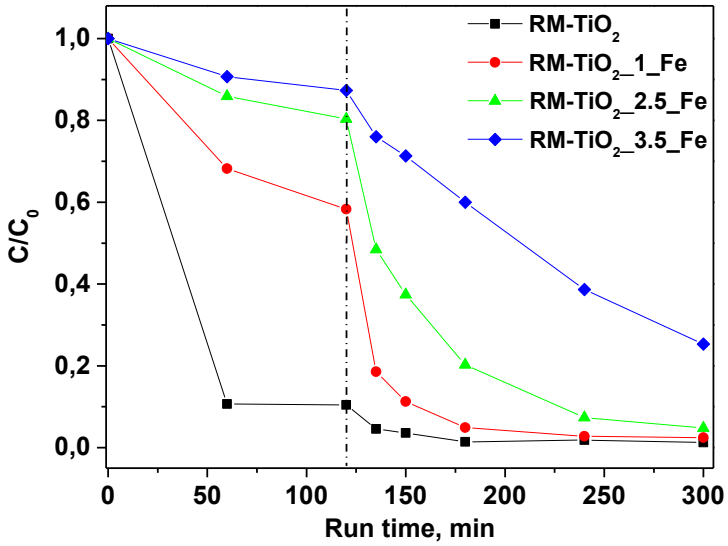

Figure 100. Results of the photocatalytic discoloration tests of RM-TiO_2 (black line), RM-TiO_2_1_Fe (red line), RM-TiO_2_2.5_Fe (green line), RM-TiO_2_3.5_Fe (blue line). The experimental condition were white LED irradiation, $3gL^{-1}$ photocatalyst concentration, and CV concentration of 10 mg L^{-1}. The broken line represents the concentration of dyes after 2h in dark condition.

The good results obtained in the discoloration experiments were explained in two ways: i) the sensitizing effect of the dye, in the case of RM-TiO_2 which boost its intrinsic photocatalytic properties and ii) the improvement of the photocatalytic properties with iron doping doped samples.

The unexpectedly low photocatalytic discoloration result obtained with the highest iron doping was already observed in the AO7 photocatalytic discoloration and mineralization tests reported in paragraph 6.5. The excessive amount of iron doping induced the formation of recombination centers for energy carriers.

The mineralization data reported in Table **21** showed a different trend than the discoloration tests.

Table 21. Mineralization results for the tests performed with the whole set of RM-TiO_2 samples in starting experimental conditions (**Table 20**).

Samples	%TOC removal in the starting experimental conditions
RM-TiO_2	0
RM-TiO_2_1_Fe	14
RM-TiO_2_2.5_Fe	52
RM-TiO_2_3.5_Fe	17

Results reported in Table **21**, when compared with Figure 100, highlighted the differences between photocatalytic discoloration and mineralization processes.

The photocatalytic discoloration process led to the formation of by-products of CV that did not show the chromophore group and, consequently, were not detected by UV-Vis spectroscopy. However, these molecules cannot be considered optimal by-products. On the other hand, the RM-TiO_2_2.5_Fe sample reached 52 % mineralization of the CV molecule. The mineralization results offered experimental evidence of the benefits of iron doping already explained in the previous paragraph and the literature.[89], [131], [196]

Once the best photocatalyst was established among the iron-doped RM-TiO_2 samples, the gas bubbling during the photocatalytic tests was changed to investigate the influence of oxygen presence in the system.

In the literature, the role of bubbled gas is well known because the presence of bubbled oxygen or standard air can increase the formation of ROS species in the system. For this reason, we tested the photocatalytic discoloration and mineralization properties with either nitrogen or air flow inside the reactor. [201]

Figure 101 reported the kinetic results of the photocatalytic discoloration process of the CV molecules under white led light with the best photocatalyst of the previous set of tests (RM-TiO_2_2.5_Fe) and starting experimental conditions (**Table 20**) with different gas flow purging inside the reactor.

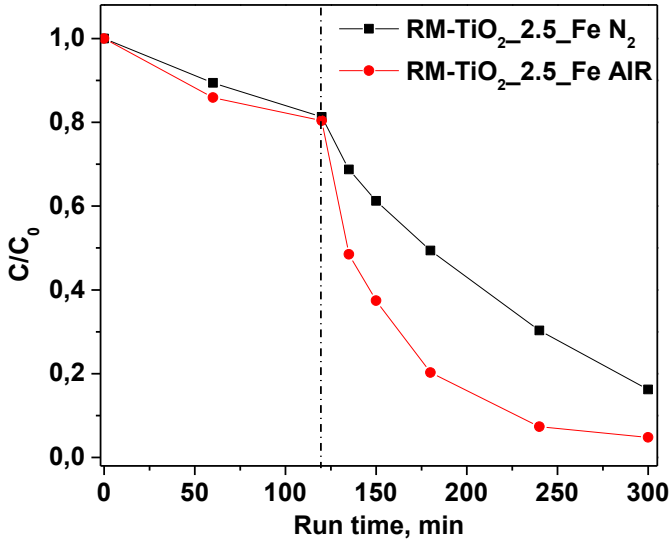

Figure 101. Results of the photocatalytic discoloration tests of RM-TiO_2_2.5_Fe sample with air purging (red line) and nitrogen purging (black line). The broken line represents the concentration of dyes after 2h in dark condition.

Photocatalytic discoloration and mineralization of CV were partially inhibited by the absence of oxygen flow, testifying to the influence of hydroxyl radicals and superoxide radical anions in these processes.

Once oxygen's influence on photocatalytic discoloration and mineralization processes was evidenced, further investigation on the effects of ROS species in the photocatalytic processes was performed by testing photocatalytic discoloration efficiency with scavenger molecules. [131]

The experimental settings selected were the starting conditions (**Table 20**) with introduction of scavenger molecules that can inhibit the influence of selected ROS species on the photocatalytic process.

Figure 102 shows the results of the photocatalytic discoloration tests performed with scavenger molecules. The selected scavengers molecules were: ethylenediaminetetraacetic acid (EDTA), p-Benzoquinone (BQ), and isopropyl alcohol (IPA) to quench $O_2^{\bullet-}$, h^+ (holes), and •OH photocatalytic activity, respectively.

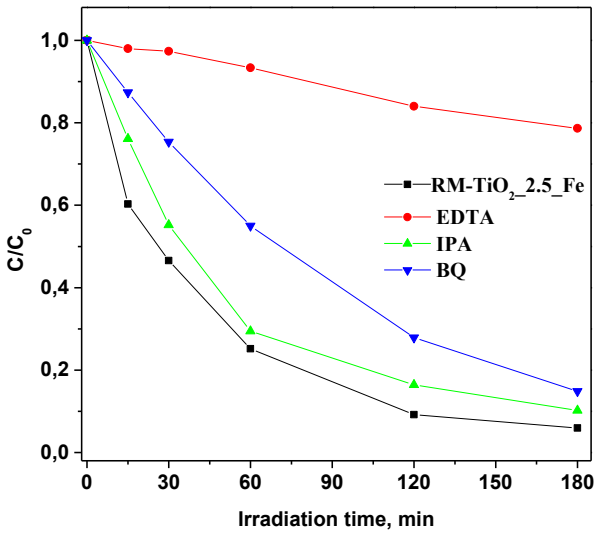

Figure 102. Results of the photocatalytic discoloration tests of M-TiO_2_2.5_Fe (black line) compared with the same experimental condition but with scavenger molecules: EDTA (red line), isopropanol (green line) and benzoquinone (blue line).

These results validated the previous hypothesis concerning the importance of $O_2^{\bullet-}$species in CV photocatalytic discoloration and mineralization processes with RM-TiO_2_2.5_Fe sample. The effects of hydroxyl radicals on the photocatalytic discoloration efficiency of CV seemed lower compared to superoxide radical anions that, once quenched, significantly inhibited the discoloration. [131]

6.7 Discussion

The photocatalytic properties of the samples were studied using as target molecules emerging pollutants. Undoped samples were used for photocatalytic degradation of paracetamol and N-phenylurea showing promising photocatalytic properties depending on their intrinsic physico-chemical properties summarized in Chapter 4.

According to experimental evidences AB sample was the most effective during paracetamol and N-phenylurea photocatalytic degradation under 1 SUN among the

materials proposed. Furthermore, iron-doped AB sample obtained promising results in the photocatalytic degradation of simazine under UV light confirming the positive effect, induced by the photocatalyst of anatase/brookite heterojunctions.

Other doped samples were studied and the effects of iron wt. % introduced in the material was investigated by testing the photocatalytic discoloration and mineralization of dyes efficiency.

Some insights into experimental parameters variations during the photocatalytic tests were proposed by optimizing parameters (i.e. photocatalyst or pollutant concentration).

7 Conclusions

Three different sol-gel synthesis methods allowed tuning the physico-chemical properties of TiO_2 NPs developed for the photocatalytic degradation of some emerging contaminants. An accurate physico-chemical characterization of the samples offered the opportunity to understand correlations between the synthesis method and the three TiO_2-based materials' properties. Furthermore, the introduction of iron in the procedures provided several Fe-doped TiO_2 photocatalysts with the aim to enhance the photocatalytic properties of the corresponding undoped TiO_2 materials.

A detailed characterization of the doped samples provided an insight into iron's influence on the physico-chemical properties of the samples. Even in this case, the photocatalytic applications were tested to assess the interconnections between doped nano-TiO_2 NPs properties and photocatalytic efficiency.

The adopted synthesis methods included two soft-template-assisted sol-gel synthesis methods. In one case, the system was based on direct micelles formation, aiding a mesoporous structure formation with inter- and intraparticles mesoporosity (M-TiO_2 sample). On the other hand, a reverse micelles system was adopted, offering the control on synthesis steps and NPs morphology (RM-TiO_2 sample). The third described synthesis method was based on a template-free sol-gel method under pH control to tune the amount of brookite, which led to the synthesis of two samples (AB and ABR samples).

Both AB and ABR showed a mixed polymorphic structure composition; anatase-brookite in the AB sample and anatase-brookite-rutile in the case of the ABR sample. In this case, the effects of calcination temperature on the physico-chemical properties differentiating the two samples were investigated, offering insight into calcination temperature effects on the properties of the TiO_2 NPs.

The three synthesis methods were adapted for the iron-doped samples synthesis, and three different sets of iron-doped TiO_2 NPs were obtained.

Different weight percentages of iron were introduced to guarantee the opportunity to investigate the correlation between the introduced Fe amount in the materials and the photocatalytic properties. The samples were characterized by

different techniques offering experimental evidence of Fe influence on physico-chemical properties of the nano-TiO_2 NPs.

The effects of iron doping on the bulk of the NPs were observed in two main experimental evidence: a red shift of the samples' absorption edge and an influence on the crystallite dimension. On the other hand, the iron presence affected the surface properties of the materials by promoting the formation of iron-rich species on the surface of the NPs, as evidenced by different characterization techniques.

The photocatalytic properties of the undoped materials were tested toward the degradation of N-containing emerging contaminants: Paracetamol and N-phenylurea. The best photocatalyst for paracetamol and N-phenylurea degradation (under 1 SUN) was the AB sample taking advantage of the heterojunctions between anatase and brookite phase. In agreement with the literature, these heterojunctions offer the most efficient exploitation of solar-simulated light by stabilizing electron/holes pairs.

Another adequate sample in paracetamol photocatalytic degradation was the M-TiO_2, showing a kinetic constant (under 1 SUN) comparable with that of the AB and P25 (commercial benchmark) samples. According to the literature, the possible explanation for the lower photocatalytic efficiency of the other samples was attributed to phase composition, surface area, morphology, and NPs' aggregation, which are properties affecting the photocatalytic performance.

The photocatalytic properties of the Fe-doped samples were tested by comparing the same materials with different doping amounts during the photocatalytic degradation of two azo-dyes used as target molecules. The M-TiO_2_Fe set of samples (with 1, 2.5, and 3.5 wt. % Fe) were tested in the photocatalytic degradation of AO7 (an anionic dye). The RM-TiO_2_Fe set of samples (with 1, 2.5, and 3.5 wt. % Fe) were tested in the photocatalytic degradation of CV (a cationic dye). Both sets of experiments were performed under solar/visible light. In both cases, an iron content corresponding to 2.5 wt. % induced better photocatalytic performance.

The photocatalytic parameters were optimized in both experiments, and a promising mineralization percentage of the dyes was obtained.

The AB_Fe samples (with 0.05, 1, 2.5 wt. % Fe) were tested in the photocatalytic degradation of simazine under solar-simulated and UV light. The samples showed a moderate photocatalytic efficiency under solar-simulated light, confirming the positive effect of anatase/brookite heterojunction presence. The chemical stability of the Simazine molecule induced the use of UV light to boost

the photocatalytic properties of the materials. In the photocatalytic tests performed under UV light, the most promising results were obtained with the undoped sample and AB_0.005_Fe sample.

8 References

[1] F. Parrino and L. Palmisano, *Titanium Dioxide Its Applications*. 2021.

[2] A. M. Samoylov and V. N. Popov, *Titanium Dioxide (TiO_2) and Its Applications*. .

[3] Y. Liu, Z. Li, M. Green, M. Just, Y. Y. Li, and X. Chen, "Titanium dioxide nanomaterials for photocatalysis," *J. Phys. D. Appl. Phys.*, vol. 50, no. 19, 2017, doi: 10.1088/1361-6463/aa6500.

[4] R. Nasi *et al.*, "Application of Reverse Micelle Sol – Gel Synthesis for Bulk Doping and Heteroatoms Surface Enrichment in," doi: 10.3390/ma12060937.

[5] A. Di Paola, E. García-López, G. Marcì, and L. Palmisano, "A survey of photocatalytic materials for environmental remediation," *J. Hazard. Mater.*, vol. 211–212, pp. 3–29, 2012, doi: 10.1016/j.jhazmat.2011.11.050.

[6] F. Freyria, F. Geobaldo, and B. Bonelli, "Nanomaterials for the Abatement of Pharmaceuticals and Personal Care Products from Wastewater," *Appl. Sci.*, vol. 8, no. 2, p. 170, 2018, doi: 10.3390/app8020170.

[7] H. Wang *et al.*, "A review on heterogeneous photocatalysis for environmental remediation: From semiconductors to modification strategies," *Chinese J. Catal.*, vol. 35, no. 0, pp. 178–214, 2022, doi: 10.1016/S1872.

[8] W. Zhao, Y. Li, and W. Shen, "Tuning the shape and crystal phase of TiO_2 nanoparticles for catalysis," *Chem. Commun.*, vol. 57, no. 56, pp. 6838–6850, 2021, doi: 10.1039/d1cc01523k.

[9] M. Manzoli, F. S. Freyria, N. Blangetti, and B. Bonelli, "Brookite, a sometimes under evaluated TiO_2 polymorph," *RSC Adv.*, vol. 12, no. 6, pp. 3322–3334, 2022, doi: 10.1039/d1ra09057g.

[10] T. Zhu and S. P. Gao, "The stability, electronic structure, and optical property of TiO_2 polymorphs," *J. Phys. Chem. C*, vol. 118, no. 21, pp. 11385–11396, 2014, doi: 10.1021/jp412462m.

[11] M. Manzoli, F. S. Freyria, N. Blangetti, and B. Bonelli, "Brookite, a sometimes under evaluated TiO_2 polymorph," *RSC Adv.*, vol. 12, no. 6, pp. 3322–3334, 2022, doi: 10.1039/d1ra09057g.

[12] X. Q. Gong and A. Selloni, "First-principles study of the structures and energetics of stoichiometric brookite TiO_2 surfaces," *Phys. Rev. B - Condens.*

Matter Mater. Phys., vol. 76, no. 23, pp. 1–11, 2007, doi: 10.1103/PhysRevB.76.235307.

[13] X. Che, L. Li, J. Zheng, G. Li, and Q. Shi, "Heat capacity and thermodynamic functions of brookite TiO_2," *J. Chem. Thermodyn.*, vol. 93, pp. 45–51, 2016, doi: 10.1016/j.jct.2015.09.018.

[14] D. A. H. Hanaor and C. C. Sorrell, "Review of the anatase to rutile phase transformation," *J. Mater. Sci.*, vol. 46, no. 4, pp. 855–874, 2011, doi: 10.1007/s10853-010-5113-0.

[15] H. Zhang and J. F. Banfield, "Understanding polymorphic phase transformation behavior during growth of nanocrystalline aggregates: Insights from TiO_2," *J. Phys. Chem. B*, vol. 104, no. 15, pp. 3481–3487, 2000, doi: 10.1021/jp000499j.

[16] I. Medina-Ramirez and A. Hernandez-Ramirez, *Photocatalytic Semiconductors*. Springer, 2015.

[17] R. López and R. Gómez, "Band-gap energy estimation from diffuse reflectance measurements on sol-gel and commercial TiO 2: A comparative study," *J. Sol-Gel Sci. Technol.*, vol. 61, no. 1, pp. 1–7, 2012, doi: 10.1007/s10971-011-2582-9.

[18] J. Zhang, P. Zhou, J. Liu, and J. Yu, "New understanding of the difference of photocatalytic activity among anatase, rutile and brookite TiO_2," *Phys. Chem. Chem. Phys.*, vol. 16, no. 38, pp. 20382–20386, 2014, doi: 10.1039/c4cp02201g.

[19] J. Buckeridge *et al.*, "Polymorph Engineering of TiO_2: Demonstrating How Absolute Reference Potentials Are Determined by Local Coordination," *Chem. Mater.*, vol. 27, no. 11, pp. 3844–3851, 2015, doi: 10.1021/acs.chemmater.5b00230.

[20] A. Mancuso *et al.*, "Fe-Doped TiO_2 Prepared by a Three-Block Copolymer Templating Approach," 2021.

[21] C. B. Anucha, I. Altin, E. Bacaksiz, and V. N. Stathopoulos, "Titanium dioxide (TiO_2)-based photocatalyst materials activity enhancement for contaminants of emerging concern (CECs) degradation: In the light of modification strategies," *Chem. Eng. J. Adv.*, vol. 10, no. September 2021, p. 100262, 2022, doi: 10.1016/j.ceja.2022.100262.

[22] A. H. Navidpour, S. Abbasi, D. Li, A. Mojiri, and J. L. Zhou, "Investigation of Advanced Oxidation Process in the Presence of TiO_2 Semiconductor as Photocatalyst: Property, Principle, Kinetic Analysis, and Photocatalytic Activity," *Catalysts*, vol. 13, no. 2, 2023, doi: 10.3390/catal13020232.

[23] X. Jiang *et al.*, "Anatase and rutile in evonik aeroxide P25: Heterojunctioned or individual nanoparticles?," *Catal. Today*, vol. 300, pp. 12–17, Feb. 2018,

doi: 10.1016/J.CATTOD.2017.06.010.

[24] D. C. Hurum, A. G. Agrios, K. A. Gray, T. Rajh, and M. C. Thurnauer, "Explaining the Enhanced Photocatalytic Activity of Degussa P25 Mixed-Phase TiO_2 Using EPR," pp. 4545–4549, 2003.

[25] A. A. Ismail, T. A. Kandiel, and D. W. Bahnemann, "Novel (and better?) titania-based photocatalysts: Brookite nanorods and mesoporous structures," *J. Photochem. Photobiol. A Chem.*, vol. 216, no. 2–3, pp. 183–193, 2010, doi: 10.1016/j.jphotochem.2010.05.016.

[26] T. Balaganapathi, B. KaniAmuthan, S. Vinoth, and P. Thilakan, "Synthesis, characterization and dye adsorption studies of porous brookite and mixed brookite with rutile TiO_2 using PEG assisted sol-gel synthesis process," *Mater. Res. Bull.*, vol. 91, pp. 114–121, 2017, doi: 10.1016/j.materresbull.2017.03.036.

[27] F. S. Freyria *et al.*, "Effects of the Brookite Phase on the Properties of Different Nanostructured TiO_2 Phases Photocatalytically Active Towards the Degradation of N-Phenylurea," *ChemistryOpen*, vol. 9, no. 9, pp. 903–912, 2020, doi: 10.1002/open.202000127.

[28] D. O. Scanlon *et al.*, "Band alignment of rutile and anatase TiO_2," *Nat. Mater.*, vol. 12, no. 9, pp. 798–801, 2013, doi: 10.1038/nmat3697.

[29] T. M. Khedr, S. M. El-Sheikh, E. Kowalska, and H. M. Abdeldayem, "The synergistic effect of anatase and brookite for photocatalytic generation of hydrogen and diclofenac degradation," *J. Environ. Chem. Eng.*, vol. 9, no. 6, 2021.

[30] B. K. Mutuma, G. N. Shao, W. D. Kim, and H. T. Kim, "Sol-gel synthesis of mesoporous anatase-brookite and anatase-brookite-rutile TiO_2 nanoparticles and their photocatalytic properties," *J. Colloid Interface Sci.*, vol. 442, no. May 2018, pp. 1–7, 2015, doi: 10.1016/j.jcis.2014.11.060.

[31] S. Gervasi, N. Blangetti, F. S. Freyria, S. Guastella, and B. Bonelli, "Physico-Chemical Characterization and Photocatalytic Activity towards Simazine Degradation," no. 2, 2023.

[32] M. A. Hossain *et al.*, "Synthesis of Fe- or Ag-doped TiO_2–MWCNT nanocomposite thin films and their visible-light-induced catalysis of dye degradation and antibacterial activity," *Res. Chem. Intermed.*, vol. 44, no. 4, pp. 2667–2683, 2018, doi: 10.1007/s11164-018-3253-z.

[33] J. Fang, F. Wang, K. Qian, H. Bao, Z. Jiang, and W. Huang, "Bifunctional N-Doped Mesoporous TiO_2 Photocatalysts," *J. Phys. Chem. C*, vol. 112, no. 46, pp. 18150–18156, 2008.

[34] H. Moradi, A. Eshaghi, S. R. Hosseini, and K. Ghani, "Fabrication of Fe-doped TiO_2 nanoparticles and investigation of photocatalytic decolorization

of reactive red 198 under visible light irradiation," *Ultrason. Sonochem.*, vol. 32, no. March, pp. 314–319, 2016, doi: 10.1016/j.ultsonch.2016.03.025.

[35] T. Nishikawa, T. Nakajima, and Y. Shinohara, "An exploratory study on effect of the isomorphic replacement of Ti4+ ions by various metal ions on the light absorption character of TiO_2," *J. Mol. Struct. THEOCHEM*, vol. 545, no. 1–3, pp. 67–74, 2001, doi: 10.1016/S0166-1280(01)00394-3.

[36] H. Khan and I. K. Swati, "Fe3+-doped Anatase TiO_2 with d-d Transition, Oxygen Vacancies and Ti3+ Centers: Synthesis, Characterization, UV-vis Photocatalytic and Mechanistic Studies," *Ind. Eng. Chem. Res.*, vol. 55, no. 23, pp. 6619–6633, 2016, doi: 10.1021/acs.iecr.6b01104.

[37] S. Sood, A. Umar, S. K. Mehta, and S. K. Kansal, "Highly effective Fe-doped TiO_2 nanoparticles photocatalysts for visible-light driven photocatalytic degradation of toxic organic compounds," *J. Colloid Interface Sci.*, vol. 450, pp. 213–223, 2015, doi: 10.1016/j.jcis.2015.03.018.

[38] T. Tong, J. Zhang, B. Tian, F. Chen, and D. He, "Preparation of Fe3+-doped TiO_2 catalysts by controlled hydrolysis of titanium alkoxide and study on their photocatalytic activity for methyl orange degradation," *J. Hazard. Mater.*, vol. 155, no. 3, pp. 572–579, 2008, doi: 10.1016/j.jhazmat.2007.11.106.

[39] J. Yu, Q. Xiang, and M. Zhou, "Preparation, characterization and visible-light-driven photocatalytic activity of Fe-doped titania nanorods and first-principles study for electronic structures," *Appl. Catal. B Environ.*, vol. 90, no. 3–4, pp. 595–602, 2009, doi: 10.1016/j.apcatb.2009.04.021.

[40] V. Etacheri, C. Di Valentin, J. Schneider, D. Bahnemann, and S. C. Pillai, "Visible-light activation of TiO_2 photocatalysts: Advances in theory and experiments," *J. Photochem. Photobiol. C Photochem. Rev.*, vol. 25, pp. 1–29, 2015, doi: 10.1016/j.jphotochemrev.2015.08.003.

[41] F. Freyria *et al.*, "Pure and Fe-Doped Mesoporous Titania Catalyse the Oxidation of Acid Orange 7 by H_2O_2 under Different Illumination Conditions: Fe Doping Improves Photocatalytic Activity under Simulated Solar Light," *Catalysts*, vol. 7, no. 7, p. 213, Jul. 2017, doi: 10.3390/catal7070213.

[42] D. Komaraiah, E. Radha, J. Sivakumar, M. V. Ramana Reddy, and R. Sayanna, "Structural, optical properties and photocatalytic activity of Fe^{3+} doped TiO_2 thin films deposited by sol-gel spin coating," *Surfaces and Interfaces*, vol. 17, no. April, p. 100368, 2019, doi: 10.1016/j.surfin.2019.100368.

[43] D. Komaraiah, E. Radha, J. Sivakumar, and R. Sayanna, "Influence of Fe^{3+} ions on the optical properties and photocatalytic ability of spin coated Fe^{3+} doped brookite TiO_2 thin films Influence of Fe 3 + ions on the optical

properties and photocatalytic ability of spin coated Fe 3 + doped brookite TiO 2 th."

[44] J. Zhu, F. Chen, J. Zhang, H. Chen, and M. Anpo, "Fe^{3+}-TiO_2 photocatalysts prepared by combining sol-gel method with hydrothermal treatment and their characterization," *J. Photochem. Photobiol. A Chem.*, vol. 180, no. 1–2, pp. 196–204, 2006, doi: 10.1016/j.jphotochem.2005.10.017.

[45] J. Singh, P. Yadav, A. K. Pal, and V. Mishra, *Water Pollutants: Origin and Status*. 2020.

[46] C. He *et al.*, "Future global urban water scarcity and potential solutions," *Nat. Commun.*, vol. 12, no. 1, pp. 1–11, 2021, doi: 10.1038/s41467-021-25026-3.

[47] J. Tóth, "ORIGIN, DISTRIBUTION, FORMATION, AND EFFECTS," *groundwater*, vol. I.

[48] R. Schwarzenbach *et al.*, "The Challenge of Micropollutants in Aquatic Systems," *Science (80-.).*, vol. 313, no. August, pp. 1072–1077, 2006.

[49] A. Jurado, E. Vàzquez-Suñé, J. Carrera, M. López de Alda, E. Pujades, and D. Barceló, "Emerging organic contaminants in groundwater in Spain: A review of sources, recent occurrence and fate in a European context," *Sci. Total Environ.*, vol. 440, pp. 82–94, 2012, doi: 10.1016/j.scitotenv.2012.08.029.

[50] V. Dulio *et al.*, "Emerging pollutants in the EU: 10 years of NORMAN in support of environmental policies and regulations," *Environ. Sci. Eur.*, vol. 30, no. 1, 2018, doi: 10.1186/s12302-018-0135-3.

[51] F. S. Freyria, F. Geobaldo, and B. Bonelli, "Nanomaterials for the abatement of pharmaceuticals and personal care products from wastewater," *Appl. Sci.*, vol. 8, no. 2, 2018, doi: 10.3390/app8020170.

[52] S. Dey, F. Bano, and A. Malik, *Pharmaceuticals and personal care product (PPCP) contamination-a global discharge inventory*. Elsevier Inc., 2019.

[53] T. Deblonde, C. Cossu-Leguille, and P. Hartemann, "Emerging pollutants in wastewater: A review of the literature," *Int. J. Hyg. Environ. Health*, vol. 214, no. 6, pp. 442–448, 2011, doi: 10.1016/j.ijheh.2011.08.002.

[54] I. C. Vasilachi, D. M. Asiminicesei, D. I. Fertu, and M. Gavrilescu, "Occurrence and fate of emerging pollutants in water environment and options for their removal," *Water (Switzerland)*, vol. 13, no. 2, pp. 1–34, 2021, doi: 10.3390/w13020181.

[55] K. Balakrishna, A. Rath, Y. Praveenkumarreddy, K. S. Guruge, and B. Subedi, "A review of the occurrence of pharmaceuticals and personal care products in Indian water bodies," *Ecotoxicol. Environ. Saf.*, vol. 137, no. November 2016, pp. 113–120, 2017, doi: 10.1016/j.ecoenv.2016.11.014.

[56] M. Abdul Mottaleb, M. J. Meziani, M. Abdul Matin, M. Musavvir Arafat, and M. A. Wahab, “Emerging micro-pollutants pharmaceuticals and personal care products (PPCPs) contamination concerns in aquatic organisms-LC/MS and GC/MS Analysis,” *ACS Symp. Ser.*, vol. 1198, pp. 43–74, 2015, doi: 10.1021/bk-2015-1198.ch003.

[57] F. S. Freyria, F. Geobaldo, and B. Bonelli, “Nanomaterials for the abatement of pharmaceuticals and personal care products from wastewater,” *Appl. Sci.*, vol. 8, no. 2, 2018, doi: 10.3390/app8020170.

[58] K. Shankar and H. M. Mehendale, “Acetaminophen,” *Encycl. Toxicol.*, pp. 26–29, Jan. 2014, doi: 10.1016/B978-0-12-386454-3.00215-3.

[59] N. Blangetti, F. S. Freyria, M. C. Calviello, N. Ditaranto, S. Guastella, and B. Bonelli, “Photocatalytic Degradation of Paracetamol under Simulated Sunlight by Four TiO_2 Commercial Powders: An Insight into the Performance of Two Sub-Micrometric Anatase and Rutile Powders and a Nanometric Brookite Powder,” *Catalysts*, vol. 13, no. 2, 2023, doi: 10.3390/catal13020434.

[60] P. Verlicchi, M. Al Aukidy, and E. Zambello, “Occurrence of pharmaceutical compounds in urban wastewater: Removal, mass load and environmental risk after a secondary treatment-A review,” *Sci. Total Environ.*, vol. 429, pp. 123–155, 2012, doi: 10.1016/j.scitotenv.2012.04.028.

[61] J. L. Wilkinson, A. B. A. Boxall, and D. W. Kolpin, “Pharmaceutical pollution of the world ’ s rivers,” *PNAS*, vol. 119, no. 8, pp. 1–10, 2022, doi: https://doi.org/10.1073/pnas.2113947119.

[62] A. Togola and H. Budzinski, “Multi-residue analysis of pharmaceutical compounds in aqueous samples,” *J. Chromatogr. A*, vol. 1177, no. 1, pp. 150–158, Jan. 2008, doi: 10.1016/J.CHROMA.2007.10.105.

[63] W. Li, X. Zhang, and J. Han, “Formation of Larger Molecular Weight Disinfection Byproducts from Acetaminophen in Chlorine Disinfection,” *Environ. Sci. Technol.*, vol. 56, no. 23, pp. 16929–16939, 2022, doi: 10.1021/acs.est.2c06394.

[64] W. Heri, F. Pfister, B. Carroll, T. Parshley, and J. B. Nabors, “Production, Developmnent, and Registration of Triazine Herbicides,” *Triazine Herbic.*, pp. 31–43, 2008, doi: 10.1016/B978-044451167-6.50006-4.

[65] V. Mohaupt, J. Volker, and I. Kirst, *Pesticides in European rivers, lakes and groundwaters – Data assessment. ETC/ICM Technical Report 1/2020*, no. February 2021. 2020.

[66] 1991, *Concerning the Placing of Plant Protection Products on the Market*. .

[67] F. Grasselli, S. Bussolati, R. Ramoni, S. Grolli, and G. Basini, “Simazine, a triazine herbicide, disrupts swine granulosa cell functions,” *Anim. Reprod.*,

vol. 15, no. 1, pp. 3–11, 2018, doi: 10.21451/1984-3143-2017-AR960.

[68] "Endocrine-disrupting Pesticide Atrazine to Be Banned in Hawaii, Five U.S. Territories, Prohibited on Conifers, Roadsides." https://biologicaldiversity.org/w/news/press-releases/endocrine-disrupting-pesticide-atrazine-be-banned-hawaii-five-us-territories-prohibited-conifers-roadsides-2020-09-23/ (accessed Mar. 04, 2023).

[69] Y. Rao and W. Chu, "Visible light-induced photodegradation of simazine in aqueous TiO_2 suspension," *Ind. Eng. Chem. Res.*, vol. 52, no. 38, pp. 13580–13586, 2013, doi: 10.1021/ie401191d.

[70] V. Mohaupt, J. Volker, and I. Kirst, *Pesticides in European rivers, lakes and groundwaters – Data assessment. ETC/ICM Technical Report 1/2020*, no. February 2021. 2020.

[71] F. Lai *et al.*, "A comparative study on the degradation of phenylurea herbicides by UV/persulfate process: Kinetics, mechanisms, energy demand and toxicity evaluation associated with DBPs," *Chem. Eng. J.*, vol. 428, no. May 2021, p. 132088, 2022, doi: 10.1016/j.cej.2021.132088.

[72] Q. Liu, "Pollution and Treatment of Dye Waste-Water," *IOP Conf. Ser. Earth Environ. Sci.*, vol. 514, no. 5, 2020, doi: 10.1088/1755-1315/514/5/052001.

[73] S. Mani and R. N. Bharagava, "Exposure to Crystal Violet, Its Toxic, Genotoxic and Carcinogenic Effects on Environment and Its Degradation and Detoxification for Environmental Safety," *Rev. Environ. Contam. Toxicol.*, vol. 237, pp. 71–104, 2016, doi: 10.1007/978-3-319-23573-8_4.

[74] F. S. Freyria, B. Bonelli, R. Sethi, M. Armandi, E. Belluso, and E. Garrone, "Reactions of Acid Orange 7 with Iron Nanoparticles in Aqueous Solutions," *J. Phys. Chem. C*, vol. 115, no. 49, pp. 24143–24152, 2011, doi: 10.1021/jp204762u.

[75] D. Bokov *et al.*, "Nanomaterial by Sol-Gel Method: Synthesis and Application," *Adv. Mater. Sci. Eng.*, vol. 2021, 2021, doi: 10.1155/2021/5102014.

[76] M. Atif *et al.*, "Ecotoxicology and Environmental Safety Synthesis , characterization and advanced sustainable applications of titanium dioxide nanoparticles : A review," *Ecotoxicol. Environ. Saf.*, vol. 212, p. 111978, 2021, doi: 10.1016/j.ecoenv.2021.111978.

[77] M. Cargnello, T. R. Gordon, and C. B. Murray, "Solution-Phase Synthesis of Titanium Dioxide Nanoparticles and Nanocrystals," 2014, doi: 10.1021/cr500170p.

[78] M. Cargnello, T. R. Gordon, and C. B. Murray, "Solution-phase synthesis of titanium dioxide nanoparticles and nanocrystals," *Chem. Rev.*, vol. 114, no.

19, pp. 9319–9345, 2014, doi: 10.1021/cr500170p.

[79] H. V. La Mer Dinegar, “Theory, Production and Mechanism of Formation of Monodispersed Hydrosols,” *J. Am. Chem. Soc.*, vol. 72, no. 8, 1950.

[80] Q. Shi, Z. Qin, S. Sharma, and G. Li, “Recent Progress in Heterogeneous Catalysis by Atomically and Structurally Precise Metal Nanoclusters,” *Chem. Rec.*, vol. 21, no. 4, pp. 879–892, 2021, doi: 10.1002/tcr.202100001.

[81] Serena esposito, *Sol – Gel Synthesis Strategies for Tailored Catalytic Materials SpringerBriefs in Materials*. Springer, 2022.

[82] Serena esposito, *Sol – Gel Synthesis Strategies for Tailored Catalytic Materials SpringerBriefs in Materials*. 2022.

[83] S. G. Science, T. Physicschemistry, O. Sol, and G. Processing, “Full text of " Brinker , C . And Scherer , G . 1990 Sol Gel Science : The Physics And Chemistry Of Sol Gel Processing ",” pp. 1–1338, 2020.

[84] P. P. Ghimire and M. Jaroniec, “Renaissance of Stöber method for synthesis of colloidal particles: New developments and opportunities,” *J. Colloid Interface Sci.*, vol. 584, pp. 838–865, 2021, doi: 10.1016/j.jcis.2020.10.014.

[85] S. Esposito, “‘Traditional’ sol-gel chemistry as a powerful tool for the preparation of supported metal and metal oxide catalysts,” *Materials (Basel).*, vol. 12, no. 4, pp. 1–25, 2019, doi: 10.3390/ma12040668.

[86] B. Bonelli, S. Esposito, and F. S. Freyria, “Mesoporous Titania: synthesis, properties and comparison with non-porous titania,” in *Titanium Dioxide*, Magdalena Janus, Ed. Intech, 2017.

[87] A. F. Sierra-Salazar *et al.*, “Unconventional Pathways for Designing Silica-Supported Pt and Pd Catalysts with Hierarchical Porosity,” *Stud. Surf. Sci. Catal.*, vol. 178, pp. 377–397, 2019, doi: 10.1016/B978-0-444-64127-4.00018-5.

[88] S. Shamaila, A. K. L. Sajjad, F. Chen, and J. Zhang, “Synthesis and characterization of mesoporous-TiO2 with enhanced photocatalytic activity for the degradation of chloro-phenol,” *Mater. Res. Bull.*, vol. 45, no. 10, pp. 1375–1382, 2010, doi: 10.1016/j.materresbull.2010.06.047.

[89] M. Piumetti, F. S. Freyria, M. Armandi, F. Geobaldo, E. Garrone, and B. Bonelli, “Fe- and V-doped mesoporous titania prepared by direct synthesis: Characterization and role in the oxidation of AO7 by H_2O_2 in the dark,” *Catal. Today*, vol. 227, pp. 71–79, 2014, doi: 10.1016/j.cattod.2013.11.013.

[90] F. S. Freyria *et al.*, “Effects of the Brookite Phase on the Properties of Different Nanostructured TiO_2 Phases Photocatalytically Active Towards the Degradation of N-Phenylurea,” *ChemistryOpen*, vol. 9, no. 9, pp. 903–912, 2020, doi: 10.1002/open.202000127.

[91] B. Bonelli *et al.*, "Reverse Micelle Strategy for the Synthesis of MnOx-TiO_2 Active Catalysts for NH_3-Selective Catalytic Reduction of NO_xat Both Low Temperature and Low Mn Content," *ACS Omega*, vol. 6, no. 38, pp. 24562–24574, 2021, doi: 10.1021/acsomega.1c03153.

[92] J. Wang, X. Li, S. Zhang, and R. Lu, "Facile synthesis of ultrasmall monodisperse 'raisin-bun'-type MoO_3/SiO_2 nanocomposites with enhanced catalytic properties," *Nanoscale*, vol. 5, no. 11, pp. 4823–4828, 2013, doi: 10.1039/c3nr01097j.

[93] S. Ghosh, "Comparative studies on brij reverse micelles prepared in benzene/surfactant/ethylammonium nitrate systems: Effect of head group size and polarity of the hydrocarbon chain," *J. Colloid Interface Sci.*, vol. 360, no. 2, pp. 672–680, 2011, doi: 10.1016/j.jcis.2011.05.006.

[94] M. Atif *et al.*, "Ecotoxicology and Environmental Safety Synthesis , characterization and advanced sustainable applications of titanium dioxide nanoparticles : A review," *Ecotoxicol. Environ. Saf.*, vol. 212, p. 111978, 2021, doi: 10.1016/j.ecoenv.2021.111978.

[95] A. Di Paola, M. Bellardita, and L. Palmisano, "Brookite, the least known TiO2 photocatalyst," *Catalysts*, vol. 3, no. 1. MDPI AG, pp. 36–73, Jan. 18, 2013, doi: 10.3390/catal3010036.

[96] M. Manzoli, F. S. Freyria, N. Blangetti, and B. Bonelli, "Brookite, a sometimes under evaluated TiO2polymorph," *RSC Advances*, vol. 12, no. 6. Royal Society of Chemistry, pp. 3322–3334, Jan. 26, 2022, doi: 10.1039/d1ra09057g.

[97] S. a Speakman, "Basics of X-Ray Powder Diffraction Required Training to Become an Independent User in the X-Ray SEF," *Mit*, vol. 1, no. 617.

[98] S. Speakman, "Basics of X-Ray Powder Diffraction," *MIT Materials Research Science and Engineering Center*. http://prism.mit.edu/xray Scott.

[99] A. Monshi, M. R. Foroughi, and M. R. Monshi, "Modified Scherrer Equation to Estimate More Accurately Nano-Crystallite Size Using XRD," *World J. Nano Sci. Eng.*, vol. 02, no. 03, pp. 154–160, 2012, doi: 10.4236/wjnse.2012.23020.

[100] A. Khorsand Zak, W. H. Abd. Majid, M. E. Abrishami, and R. Yousefi, "X-ray analysis of ZnO nanoparticles by Williamson-Hall and size-strain plot methods," *Solid State Sci.*, vol. 13, no. 1, pp. 251–256, 2011, doi: 10.1016/j.solidstatesciences.2010.11.024.

[101] T. Runčevski and C. M. Brown, "The Rietveld Refinement Method: Half of a Century Anniversary," *Cryst. Growth Des.*, vol. 21, no. 9, pp. 4821–4822, 2021, doi: 10.1021/acs.cgd.1c00854.

[102] H. Swenson and N. P. Stadie, "Langmuir's Theory of Adsorption: A

Centennial Review," *Langmuir*, vol. 35, pp. 5409–5426, 2019, doi: 10.1021/acs.langmuir.9b00154.

[103] M. Thommes *et al.*, "Physisorption of gases, with special reference to the evaluation of surface area and pore size distribution (IUPAC Technical Report)," *Pure Appl. Chem.*, vol. 87, no. 9–10, pp. 1051–1069, 2015, doi: 10.1515/pac-2014-1117.

[104] S. Brunauer, L. S. Deming, W. E. Deming, and E. Teller, "On a Theory of the van der Waals Adsorption of Gases," *J. Am. Chem. Soc.*, vol. 62, no. 7, pp. 1723–1732, 1940, doi: 10.1021/ja01864a025.

[105] K. A. Cychosz and M. Thommes, "Progress in the Physisorption Characterization of Nanoporous Gas Storage Materials," *Engineering*, vol. 4, no. 4, pp. 559–566, 2018, doi: 10.1016/j.eng.2018.06.001.

[106] M. Thommes and K. A. Cychosz, "Physical adsorption characterization of nanoporous materials: Progress and challenges," *Adsorption*, vol. 20, no. 2–3, pp. 233–250, 2014, doi: 10.1007/s10450-014-9606-z.

[107] P. J. Worsfold, "UV—visible Spectroscopy and its Applications," *Anal. Chim. Acta*, vol. 284, no. 1, p. 245, 1993, doi: 10.1016/0003-2670(93)80039-n.

[108] E. Moctezuma, E. Leyva, C. A. Aguilar, R. A. Luna, and C. Montalvo, "Photocatalytic degradation of paracetamol: Intermediates and total reaction mechanism," *J. Hazard. Mater.*, vol. 243, pp. 130–138, 2012, doi: 10.1016/j.jhazmat.2012.10.010.

[109] K. D. Dahm and D. J. Dahm, "Principles of Diffuse Reflectance Spectroscopy," *Handb. Near-Infrared Anal.*, pp. 27–43, 2021, doi: 10.1201/b22513-4.

[110] R. López and R. Gómez, "Band-gap energy estimation from diffuse reflectance measurements on sol-gel and commercial TiO 2: A comparative study," *J. Sol-Gel Sci. Technol.*, vol. 61, no. 1, pp. 1–7, Jan. 2012, doi: 10.1007/S10971-011-2582-9/TABLES/2.

[111] P. R. Griffiths, *Fourier transform infrared spectrometry*, vol. 222, no. 4621. 1983.

[112] J. Singh, M. Kumar, A. Sharma, G. Pandey, K. Chae, and S. Lee, "We are IntechOpen , the world ' s leading publisher of Open Access books Built by scientists , for scientists TOP 1 %," *Intech*, vol. 11, no. tourism, p. 13, 2016, [Online]. Available: https://www.intechopen.com/books/advanced-biometric-technologies/liveness-detection-in-biometrics.

[113] F. Martinovic *et al.*, "Solid-state ion exchange of Fe in small pore SSZ-13 zeolite: Characterization of the exchanged species and their relevance for the NOx SCR reaction," *Appl. Catal. A Gen.*, vol. 658, no. March, p. 119160,

2023, doi: 10.1016/j.apcata.2023.119160.

[114] M. W. Davidson and Mortimer Abramowitz, “Optical microscopy,” *CoatingsTech*, vol. 3, no. 2, pp. 36–43, 2006, doi: 10.4324/9780429399916-21.

[115] R. F. Egerton, *Physical principles of electron microscopy*, vol. 8, no. 12. 2005.

[116] K. E. MacArthur, “The use of annular dark-field scanning transmission electron microscopy for quantitative characterisation,” *Johnson Matthey Technol. Rev.*, vol. 60, no. 2, pp. 117–131, 2016, doi: 10.1595/205651316X691186.

[117] C. R. Che Hak *et al.*, “Field Emission Scanning Electron Microscope (FE-SEM) Facility in BTI,” *Nucl. Tech. Conv.*, p. 6, 2015, [Online]. Available: http://www.iaea.org/inis/collection/NCLCollectionStore/_Public/47/111/47111897.pdf.

[118] J. I. Goldstein *et al.*, “Scanning Electron Microscopy and X-ray Microanalysis,” 2003, doi: 10.1007/978-1-4615-0215-9.

[119] A. Alyamani and O. M. Lemine, “FE-SEM characterization of some nanomaterial,” *Intech*, vol. 11, no. tourism, p. 13, 2016, [Online]. Available: https://www.intechopen.com/books/advanced-biometric-technologies/liveness-detection-in-biometrics.

[120] D. B. Williams and C. B. Carter, “Transmission electron microscopy: A textbook for materials science,” *Transm. Electron Microsc. A Textb. Mater. Sci.*, pp. 1–760, 2009, doi: 10.1007/978-0-387-76501-3/COVER.

[121] D. B. Williams and C. B. Carter, *Transmission Electron Microscopy, A Textbook for Materials Science*. 2009.

[122] P. G. Self, H. K. D. H. Bhadeshia, and W. M. Stobbs, “Lattice spacings from lattice fringes,” *Ultramicroscopy*, vol. 6, no. 1, pp. 29–40, 1981, doi: 10.1016/S0304-3991(81)80175-1.

[123] P. Van der Heide, *X-Ray Photoelectron Spectroscopy; An Introduction to Principles and Practices*. 2012.

[124] D. N. G. Krishna and J. Philip, “Review on surface-characterization applications of X-ray photoelectron spectroscopy (XPS): Recent developments and challenges,” *Appl. Surf. Sci. Adv.*, vol. 12, no. June, p. 100332, 2022, doi: 10.1016/j.apsadv.2022.100332.

[125] R. R. Mather, *Surface modification of textiles by plasma treatments*. Woodhead Publishing Limited, 2009.

[126] A. C. Breeson, G. Sankar, G. K. L. Goh, and R. G. Palgrave, “Phase quantification by X-ray photoemission valence band analysis applied to

mixed phase TiO_2 powders," *Appl. Surf. Sci.*, vol. 423, pp. 205–209, 2017, doi: 10.1016/j.apsusc.2017.06.161.

[127] A. J. Shnoudeh *et al.*, *Synthesis, Characterization, and Applications of Metal Nanoparticles*. Elsevier Inc., 2019.

[128] V. Selvamani, *Stability Studies on Nanomaterials Used in Drugs*. Elsevier Inc., 2018.

[129] M. Kaszuba, J. Corbett, F. M. N. Watson, and A. Jones, "High-concentration zeta potential measurements using light-scattering techniques," *Philos. Trans. R. Soc. A Math. Phys. Eng. Sci.*, vol. 368, no. 1927, pp. 4439–4451, 2010, doi: 10.1098/rsta.2010.0175.

[130] M. von Smoluchowski, "Handbuch der Elektrizität und des Magnetismus," *Band II, Barth-Verlag, Leipzig*, pp. 366–427, 1921.

[131] A. Mancuso *et al.*, "Photocatalytic Degradation of Crystal Violet Dye under Visible Light by Fe-Doped TiO_2 Prepared by Reverse-Micelle Sol–Gel Method," *Nanomaterials*, vol. 13, no. 2, p. 270, 2023, doi: 10.3390/nano13020270.

[132] I. A. Saleh, N. Zouari, and M. A. Al-Ghouti, "Removal of pesticides from water and wastewater: Chemical, physical and biological treatment approaches," *Environ. Technol. Innov.*, vol. 19, p. 101026, Aug. 2020, doi: 10.1016/J.ETI.2020.101026.

[133] E. G. Rogers and P. Dorenbos, "Vacuum energy referred $Ti^{3+/4+}$ donor/acceptor states in insulating and semiconducting inorganic compounds," *J. Lumin.*, vol. 153, pp. 40–45, 2014, doi: 10.1016/j.jlumin.2014.03.002.

[134] R. López and R. Gómez, "Photocatalytic degradation of 4-nitrophenol on well characterized sol-gel molybdenum doped titania semiconductors," *Top. Catal.*, vol. 54, no. 8–9, pp. 504–511, 2011, doi: 10.1007/s11244-011-9614-0.

[135] O. Seiferth *et al.*, "Seifert1999_IR investigations of CO_2 adsorption on chromia surfaces," vol. 421, pp. 176–190, 1999.

[136] G. Jeantelot *et al.*, "Morphology control of anatase TiO_2 for well-defined surface chemistry," *Phys. Chem. Chem. Phys.*, vol. 20, no. 21, pp. 14362–14373, 2018, doi: 10.1039/c8cp01983e.

[137] Q. Gu, J. Long, Y. Zhou, R. Yuan, H. Lin, and X. Wang, "Single-site tin-grafted anatase TiO_2 for photocatalytic hydrogen production: Toward understanding the nature of interfacial molecular junctions formed in semiconducting composite photocatalysts," *J. Catal.*, vol. 289, pp. 88–99, 2012, doi: 10.1016/j.jcat.2012.01.018.

[138] M. Piumetti, F. S. Freyria, M. Armandi, F. Geobaldo, E. Garrone, and B.

Bonelli, “Fe- and V-doped mesoporous titania prepared by direct synthesis: Characterization and role in the oxidation of AO7 by H_2O_2 in the dark,” *Catal. Today*, vol. 227, pp. 71–79, 2014, doi: 10.1016/j.cattod.2013.11.013.

[139] F. Freyria *et al.*, “Pure and Fe-Doped Mesoporous Titania Catalyse the Oxidation of Acid Orange 7 by H_2O_2 under Different Illumination Conditions: Fe Doping Improves Photocatalytic Activity under Simulated Solar Light,” *Catalysts*, vol. 7, no. 7, p. 213, 2017, doi: 10.3390/catal7070213.

[140] H. Li, M. Vrinat, G. Berhault, D. Li, H. Nie, and P. Afanasiev, “Hydrothermal synthesis and acidity characterization of TiO2 polymorphs,” *Mater. Res. Bull.*, vol. 48, no. 9, pp. 3374–3382, 2013, doi: 10.1016/j.materresbull.2013.05.017.

[141] R. Nasi *et al.*, “Application of Reverse Micelle Sol–Gel Synthesis for Bulk Doping and Heteroatoms Surface Enrichment in Mo-Doped TiO_2 Nanoparticles,” *Materials (Basel).*, vol. 12, no. 6, p. 937, 2019, doi: 10.3390/ma12060937.

[142] P. Chandra, D. S. Doke, S. B. Umbarkar, and A. V. Biradar, “One-pot synthesis of ultrasmall MoO_3 nanoparticles supported on SiO_2, TiO_2, and ZrO_2 nanospheres: An efficient epoxidation catalyst,” *J. Mater. Chem. A*, vol. 2, no. 44, pp. 19060–19066, 2014, doi: 10.1039/c4ta03754e.

[143] T. T. T. Huyen, T. T. K. Chi, N. D. Dung, H. Kosslick, and N. Q. Liem, “Enhanced photocatalytic activity of {110}-faceted TiO_2 rutile nanorods in the photodegradation of hazardous pharmaceuticals,” *Nanomaterials*, vol. 8, no. 5, 2018, doi: 10.3390/nano8050276.

[144] M. G. S. Vieira, N. V. Gramosa, N. M. P. S. Ricardo, G. A. Morris, R. W. Adams, and M. Nilsson, “Natural product mixture analysis by matrix-assisted DOSY using Brij surfactants in mixed solvents,” *RSC Adv.*, vol. 4, no. 79, pp. 42029–42034, 2014, doi: 10.1039/c4ra04433a.

[145] B. K. Mutuma, G. N. Shao, W. D. Kim, and H. T. Kim, “Sol-gel synthesis of mesoporous anatase-brookite and anatase-brookite-rutile TiO_2nanoparticles and their photocatalytic properties,” *J. Colloid Interface Sci.*, vol. 442, pp. 1–7, 2015, doi: 10.1016/j.jcis.2014.11.060.

[146] Y. Hu, H. L. Tsai, and C. L. Huang, “Effect of brookite phase on the anatase-rutile transition in titania nanoparticles,” *J. Eur. Ceram. Soc.*, vol. 23, no. 5, pp. 691–696, 2003, doi: 10.1016/S0955-2219(02)00194-2.

[147] H. Yaghoubi *et al.*, “Toward a Visible Light-Driven Photocatalyst : The E ff ect of Midgap- States-Induced Energy Gap of Undoped TiO_2 Nanoparticles,” 2015.

[148] X. Chen, L. Liu, P. Y. Yu, and S. S. Mao, “Increasing solar absorption for

photocatalysis with black hydrogenated titanium dioxide nanocrystals," *Science (80-.).*, vol. 331, no. 6018, pp. 746–750, 2011, doi: 10.1126/science.1200448.

[149] C. C. Yang, Y. H. Yu, B. Van Der Linden, J. C. S. Wu, and G. Mul, "Artificial photosynthesis over crystalline TiO_2-based catalysts: Fact or fiction?," *J. Am. Chem. Soc.*, vol. 132, no. 24, pp. 8398–8406, 2010, doi: 10.1021/ja101318k.

[150] C. Morterra, E. Fisicaro, and F. Boccuzzi, "A spectroscopic study of anatase properties," *Zeitschrift fur Phys. Chemie*, vol. 124, no. 2, pp. 211–222, 1981, doi: 10.1524/zpch.1981.124.2.211.

[151] W. Su, J. Zhang, Z. Feng, T. Chen, P. Ying, and C. Li, "Surface phases of TiO_2 nanoparticles studied by UV raman spectroscopy and FT-IR spectroscopy," *J. Phys. Chem. C*, vol. 112, no. 20, pp. 7710–7716, 2008, doi: 10.1021/jp7118422.

[152] J. P. Holmberg, E. Ahlberg, J. Bergenholtz, M. Hassellöv, and Z. Abbas, "Surface charge and interfacial potential of titanium dioxide nanoparticles: Experimental and theoretical investigations," *J. Colloid Interface Sci.*, vol. 407, pp. 168–176, 2013, doi: 10.1016/j.jcis.2013.06.015.

[153] J. Li *et al.*, "In-situ formation of carboxylate species on TiO_2 nanosheets for enhanced visible-light photocatalytic performance," *J. Colloid Interface Sci.*, vol. 577, pp. 512–522, 2020, doi: 10.1016/j.jcis.2020.05.054.

[154] S. B. Eadi, S. Kim, S. W. Jeong, and H. W. Jeon, "Novel Preparation of Fe Doped TiO_2 Nanoparticles and Their Application for Gas Sensor and Photocatalytic Degradation," *Adv. Mater. Sci. Eng.*, vol. 2017, 2017, doi: 10.1155/2017/2191659.

[155] M. He, J. Ji, B. Liu, and H. Huang, "Reduced TiO_2 with tunable oxygen vacancies for catalytic oxidation of formaldehyde at room temperature," *Appl. Surf. Sci.*, vol. 473, no. December 2018, pp. 934–942, 2019, doi: 10.1016/j.apsusc.2018.12.212.

[156] S. Yu, H. J. Yun, D. M. Lee, and J. Yi, "Preparation and characterization of Fe-doped TiO_2 nanoparticles as a support for a high performance CO oxidation catalyst," *J. Mater. Chem.*, vol. 22, no. 25, pp. 12629–12635, 2012, doi: 10.1039/c2jm30360d.

[157] Y. F. Tu, S. Y. Huang, J. P. Sang, and X. W. Zou, "Preparation of Fe-doped TiO_2 nanotube arrays and their photocatalytic activities under visible light," *Mater. Res. Bull.*, vol. 45, no. 2, pp. 224–229, 2010, doi: 10.1016/j.materresbull.2009.08.020.

[158] C. W. Soo, J. C. Juan, C. W. Lai, S. B. A. Hamid, and R. M. Yusop, "Fe-doped mesoporous anatase-brookite titania in the solar-light-induced

photodegradation of Reactive Black 5 dye," *J. Taiwan Inst. Chem. Eng.*, vol. 68, pp. 153–161, 2016, doi: 10.1016/j.jtice.2016.08.025.

[159] M. Kang, S. J. Choung, and J. Y. Park, "Photocatalytic performance of nanometer-sized FexO y/TiO_2 particle synthesized by hydrothermal method," *Catal. Today*, vol. 87, no. 1–4, pp. 87–97, 2003, doi: 10.1016/j.cattod.2003.09.011.

[160] E. Borghi, M. Occhiuzzi, E. Foresti, I. G. Lesci, and N. Roveri, "Spectroscopic characterization of Fe-doped synthetic chrysotile by EPR, DRS and magnetic susceptibility measurements," *Phys. Chem. Chem. Phys.*, vol. 12, no. 1, pp. 227–238, 2010, doi: 10.1039/b915182f.

[161] E. Shafia, S. Esposito, M. Armandi, E. Bahadori, E. Garrone, and B. Bonelli, "Reactivity of bare and Fe-doped alumino-silicate nanotubes (imogolite) with H_2O_2 and the azo-dye Acid Orange 7," *Catal. Today*, vol. 277, pp. 89–96, 2016, doi: 10.1016/j.cattod.2015.10.011.

[162] M. F. and A. M. A. Mohammed M. Rahman, Sher Bahadar Khan, Aslam Jamal, "Iron Oxide Nanoparticles," *Nanomaterials*, vol. 3, no. tourism, pp. 43–67,2011,Available:https://www.intechopen.com/books/advanced-biometric-technologies/liveness-detection-in-biometrics.

[163] F. S. Freyria *et al.*, "Pure and Fe-doped mesoporous titania catalyse the oxidation of acid orange 7 by H_2O_2 under different illumination conditions: Fe doping improves photocatalytic activity under simulated solar light," *Catalysts*, vol. 7, no. 7, 2017, doi: 10.3390/catal7070213.

[164] A. V. Vorontsov, H. Valdés, P. G. Smirniotis, and Y. Paz, "Recent Advancements in the Understanding of the Surface Chemistry in TiO_2 Photocatalysis," *Surfaces*, vol. 3, no. 1, pp. 72–92, 2020, doi: 10.3390/surfaces3010008.

[165] S. Mustafa, S. Tasleem, and A. Naeem, "Surface charge properties of Fe_2O_3 in aqueous and alcoholic mixed solvents," *J. Colloid Interface Sci.*, vol. 275, no. 2, pp. 523–529, 2004, doi: 10.1016/j.jcis.2004.02.089.

[166] S. Esposito, N. Ditaranto, G. Dell'Agli, R. Nasi, P. Rivolo, and B. Bonelli, "Effective Inclusion of Sizable Amounts of Mo within TiO_2Nanoparticles Can Be Obtained by Reverse Micelle Sol-Gel Synthesis," *ACS Omega*, vol. 6, no. 8, pp. 5379–5388, 2021, doi: 10.1021/acsomega.0c05552.

[167] M. Iwasaki, K. Yamazaki, K. Banno, and H. Shinjoh, "Characterization of Fe/ZSM-5 DeNOx catalysts prepared by different methods: Relationships between active Fe sites and NH_3-SCR performance," *J. Catal.*, vol. 260, no. 2, pp. 205–216, 2008, doi: 10.1016/j.jcat.2008.10.009.

[168] L. Ma, J. Li, H. Arandiyan, W. Shi, C. Liu, and L. Fu, "Influence of calcination temperature on Fe/HBEA catalyst for the selective catalytic

reduction of NO x with NH 3," *Catal. Today*, vol. 184, no. 1, pp. 145–152, 2012, doi: 10.1016/j.cattod.2011.10.007.

[169] S. Khan *et al.*, "Revealing the true impact of interstitial and substitutional nitrogen doping in TiO_2 on photoelectrochemical applications," *J. Mater. Chem. A*, vol. 9, no. 20, pp. 12214–12224, 2021, doi: 10.1039/d0ta11494d.

[170] R. Nasi *et al.*, "Application of Reverse Micelle Sol–Gel Synthesis for Bulk Doping and Heteroatoms Surface Enrichment in Mo-Doped TiO_2 Nanoparticles," *Materials (Basel).*, vol. 12, no. 6, p. 937, 2019, doi: 10.3390/ma12060937.

[171] A. Schupp, R. D. Pütz, O. Beyss, L. H. Beste, T. Radel, and D. Zander, "Change of oxidation mechanisms by laser chemical machined rim zone modifications of 42crmo4 steel," *Materials (Basel).*, vol. 14, no. 14, pp. 1–19, 2021, doi: 10.3390/ma14143910.

[172] B. Bharti, S. Kumar, H. N. Lee, and R. Kumar, "Formation of oxygen vacancies and Ti^{3+} state in TiO_2 thin film and enhanced optical properties by air plasma treatment," *Sci. Rep.*, vol. 6, no. May, pp. 1–12, 2016, doi: 10.1038/srep32355.

[173] B. K. Mutuma, G. N. Shao, W. D. Kim, and H. T. Kim, "Sol-gel synthesis of mesoporous anatase-brookite and anatase-brookite-rutile TiO_2 nanoparticles and their photocatalytic properties," *J. Colloid Interface Sci.*, vol. 442, no. December, pp. 1–7, 2015, doi: 10.1016/j.jcis.2014.11.060.

[174] A. Mills, S. K. Lee, A. Lepre, I. P. Parkin, and S. A. O'Neill, "Spectral and photocatalytic characteristics of TiO2 CVD films on quartz," *Photochem. Photobiol. Sci.*, vol. 1, no. 11, pp. 865–868, 2002, doi: 10.1039/b205715h.

[175] L. Yang, L. E. Yu, and M. B. Ray, "Degradation of paracetamol in aqueous solutions by TiO_2 photocatalysis," *Water Res.*, vol. 42, no. 13, pp. 3480–3488, 2008, doi: 10.1016/j.watres.2008.04.023.

[176] H. Park, Y. Park, W. Kim, and W. Choi, "Surface modification of TiO_2 photocatalyst for environmental applications," *J. Photochem. Photobiol. C Photochem. Rev.*, vol. 15, no. 1, pp. 1–20, 2013, doi: 10.1016/j.jphotochemrev.2012.10.001.

[177] J.S. Knapp and K.C.A. Bromley-Challoner, "Recalcitrant organic compounds," in *Water Environment Research*, vol. 70, no. 7, 1998, pp. 1314–1326.

[178] N. San, A. Hatipŏlu, G. Koçtürk, and Z. Çinar, "Photocatalytic degradation of 4-nitrophenol in aqueous TiO_2 suspensions: Theoretical prediction of the intermediates," *J. Photochem. Photobiol. A Chem.*, vol. 146, no. 3, pp. 189–197, 2002, doi: 10.1016/S1010-6030(01)00620-7.

[179] M. S. D. and K. A. Gray, "A comparison of the degradation of 4-nitrophenol

via direct and sensitized phocatalysis in TiO_2 slurries," *water reasearch*, vol. 30, no. 5, pp. 1169–1183, 1996.

[180] E. Moctezuma, E. Leyva, G. Palestino, and H. de Lasa, "Photocatalytic degradation of methyl parathion: Reaction pathways and intermediate reaction products," *J. Photochem. Photobiol. A Chem.*, vol. 186, no. 1, pp. 71–84, 2007, doi: 10.1016/j.jphotochem.2006.07.014.

[181] X. Li, J. W. Cubbage, and W. S. Jenks, "Photocatalytic degradation of 4-chlorophenol. 2. The 4-chlorocatechol pathway," *J. Org. Chem.*, vol. 64, no. 23, pp. 8525–8536, 1999, doi: 10.1021/jo990912n.

[182] D. Vogna, R. Marotta, A. Napolitano, and M. D'Ischia, "Advanced oxidation chemistry of paracetamol. UV/H_2O_2-induced hydroxylation/degradation pathways and 15N-aided inventory of nitrogenous breakdown products," *J. Org. Chem.*, vol. 67, no. 17, pp. 6143–6151, 2002, doi: 10.1021/jo025604v.

[183] X. Li, J. W. Cubbage, and W. S. Jenks, "Variation in the chemistry of the TiO2-mediated degradation of hydroxy- and methoxybenzenes: Electron transfer and HOads· initiated chemistry," *J. Photochem. Photobiol. A Chem.*, vol. 143, no. 1, pp. 69–85, 2001, doi: 10.1016/S1010-6030(01)00472-5.

[184] A. V. Emeline, A. V. Rudakova, V. K. Ryabchuk, and N. Serpone, "Photostimulated reactions at the surface of wide band-gap metal oxides (ZrO: And TiO_2): Interdependence of rates of reactions on pressure-concentration and on light intensity," *J. Phys. Chem. B*, vol. 102, no. 52, pp. 10906–10916, 1998, doi: 10.1021/jp9830373.

[185] J. J. M. Vequizo, H. Matsunaga, T. Ishiku, S. Kamimura, T. Ohno, and A. Yamakata, "Trapping-Induced Enhancement of Photocatalytic Activity on Brookite TiO_2 Powders: Comparison with Anatase and Rutile TiO_2 Powders," *ACS Catal.*, vol. 7, no. 4, pp. 2644–2651, 2017, doi: 10.1021/acscatal.7b00131.

[186] L. O. Ahmed and R. A. Omer, "Journal of Physical Chemistry and Functional Materials Computational Study on Paracetamol Drug," *J. Phys. Chem. Funct. Mater.*, vol. 3, no. 1, pp. 9–13, 2020, [Online]. Available: https://dergipark.org.tr/jphcfum.

[187] A. S. Gunasekara, J. Troiano, K. S. Goh, and R. S. Tjeerdema, "Chemistry and fate of simazine," *Rev. Environ. Contam. Toxicol.*, vol. 189, pp. 1–23, 2007, doi: 10.1007/978-0-387-35368-5_1.

[188] J.-Y. Hu, T. Morita, Y. Magara, and T. Aizawa, "Evaluation of the Reactivity of Pesticides with Ozone in Water using the Energies of Frontier Molecular Orbitals," *Water Res.* , vol. 34, no. 8, pp. 2215–2222, 2000, [Online]. Available: www.elsevier.com/locate/watres.

[189] and A. P. D. Ricardo Cantu´ Otis Evans, Fred K. Kawahara, Jody A.

Shoemaker, “An HPLC Method with UV Detection, pH Control, and Reductive Ascorbic Acid for Cyanuric Acid Analysis in Water,” *Anal. Chem.*, vol. 72, no. 3, pp. 5820–5828, 2000, doi: 10.1111/j.1746-1561.1968.tb04978.x.

[190] E. Evgenidou and K. Fytianos, “Photodegradation of triazine herbicides in aqueous solutions and natural waters,” *J. Agric. Food Chem.*, vol. 50, no. 22, pp. 6423–6427, 2002, doi: 10.1021/jf0202887.

[191] Y. Mu *et al.*, “Dechlorination-Hydroxylation of Atrazine to Hydroxyatrazine with Thiosulfate: A Detoxification Strategy in Seconds,” *Environ. Sci. Technol.*, vol. 53, no. 6, pp. 3208–3216, 2019, doi: 10.1021/acs.est.8b06351.

[192] Y. Mu *et al.*, “Transformation of Atrazine to Hydroxyatrazine with Alkali-H_2O_2 Treatment: An Efficient Dechlorination Strategy under Alkaline Conditions,” *ACS ES T Water*, vol. 1, no. 8, pp. 1868–1877, 2021, doi: 10.1021/acsestwater.1c00127.

[193] A. J. Moreira, A. C. Borges, L. F. C. Gouvea, T. C. O. MacLeod, and G. P. G. Freschi, “The process of atrazine degradation, its mechanism, and the formation of metabolites using UV and UV/MW photolysis,” *J. Photochem. Photobiol. A Chem.*, vol. 347, pp. 160–167, 2017, doi: 10.1016/j.jphotochem.2017.07.022.

[194] M. Taniguchi and J. S. Lindsey, “Database of Absorption and Fluorescence Spectra of >300 Common Compounds for use in PhotochemCAD,” *Photochem. Photobiol.*, vol. 94, no. 2, pp. 290–327, Mar. 2018, doi: 10.1111/php.12860.

[195] VARGHESE, HEMA TRESA, R. R. J.B.BHAGYSREE, RAJEEV.T.ULAHANNAN, and C. Y. PANICKER, “FT-IR, FT-Raman and Computational study of Phenylurea,” *Orient. J. Chem.*, vol. 29, no. 1, 2013.

[196] A. Mancuso *et al.*, “Visible Light-Driven Photocatalytic Activity and Kinetics of Fe-Doped TiO_2 Prepared by a Three-Block Copolymer Templating Approach,” *Materials (Basel).*, vol. 14, no. 11, p. 3105, Jun. 2021, doi: 10.3390/ma14113105.

[197] S. D. Delekar, H. M. Yadav, S. N. Achary, S. S. Meena, and S. H. Pawar, “Structural refinement and photocatalytic activity of Fe-doped anatase TiO_2 nanoparticles,” *Appl. Surf. Sci.*, vol. 263, pp. 536–545, 2012, doi: 10.1016/j.apsusc.2012.09.102.

[198] M. L. V. P. Chippada *et al.*, “Structural modi fi cation of nano titania by doping with Barium and Copper – Impact on photocatalysis : Applications in degradation of dye and pathogens,” *Hybrid Adv.*, vol. 3, no. December 2022, p. 100033, 2023, doi: 10.1016/j.hybadv.2023.100033.

[199] J. M. Herrmann, “Heterogeneous photocatalysis: State of the art and present

applications," *Top. Catal.*, vol. 34, no. 1–4, pp. 49–65, 2005, doi: 10.1007/s11244-005-3788-2.

[200] F. Han, V. S. R. Kambala, R. Dharmarajan, Y. Liu, and R. Naidu, "Photocatalytic degradation of azo dye acid orange 7 using different light sources over Fe^{3+}-doped TiO_2 nanocatalysts," *Environ. Technol. Innov.*, vol. 12, pp. 27–42, 2018, doi: 10.1016/j.eti.2018.07.004.

[201] C. V. Rekhate and J. K. Srivastava, "Recent advances in ozone-based advanced oxidation processes for treatment of wastewater- A review," *Chem. Eng. J. Adv.*, vol. 3, no. June, p. 100031, 2020, doi: 10.1016/j.ceja.2020.100031.